Nonlinear dynamics and applications of MEMS and NEMS resonators.

Jin, Leisheng

Nonlinear Dynamics and Applications of MEMS and NEMS Resonators

Swansea University
Prifysgol Abertawe

Leisheng Jin

Department of Engineering

Swansea University

This dissertation is submitted for the degree of

Doctor of Philosophy

October 2015

Declaration/Statements

DECLARATION

This work has not previously been accepted in substance for any degree and is not being concurrently submitted in candidature for any degree.

Signed .... (candidate)
Date .....2015/10/14.....

STATEMENT 1

This thesis is the result of my own investigations, except where otherwise stated. Where correction services have been used, the extent and nature of the correction is clearly marked in a footnote(s).
Other sources are acknowledged by footnotes giving explicit references. A bibliography is appended.

Signed ..... (candidate)
Date .....2015/10/14.....

STATEMENT 2

I hereby give consent for my thesis, if accepted, to be available for photocopying and for inter-library loan, and for the title and summary to be made available to outside organisations.

Signed .... (candidate)
Date .....2015/10/14.....

To my family

Declaration

I hereby declare that except where specific reference is made to the work of others, the contents of this dissertation are original and have not been submitted in whole or in part for consideration for any other degree or qualification in this, or any other university. This dissertation is my own work and contains nothing which is the outcome of work done in collaboration with others, except as specified in the text and Acknowledgements. This dissertation contains fewer than 65,000 words including appendices, bibliography, footnotes, tables and equations and has fewer than 150 figures.

Leisheng Jin
October 2015

Acknowledgements

First thanks to my supervisor Dr. Lijie Li, who has been guiding me throughout my PhD study. Without his support and encouragement, I could not finish this project. The special way of his seeing, analyzing and solving the scientific problems has influenced me very much, and I believe this influence will be accompanying my future study and life.

Thanks to my PhD colleague Mr. Jie Mei. He is the one who spends the most time with me in the same office. Countless of discussions with him are very helpful for my research. Colleague Mr. Zheng Jun Chew is also acknowledged here. I would like to thank him for giving me lots of beneficial advices. Further, many thanks go to all the rest office mates for creating an enjoyable woking environment.

Thanks to all my friends I have met here. Special thanks go to Mr. Chuanrui Gan who is the first I have met in Swansea. I am grateful to meet all of you: Jing Tong, Ming Chen, Zunding Xiao, Yingjie Wang, Lei Li, Feihong Bian and so on, forgiving me that I could not write all of your names here. Many thanks to Miss. Juan Kang and Miss. Chenxia Li. The memory of the great time we have had together will last forever.

Thanks to the Chinese Scholarship Council (CSC) for its financial support.

Finally, special thanks go to my family. It is the endless love from my parents, my sister Xuewe Jin and my lovely niece Yichen Wang that makes me strong and not alone in UK.

Abstract

Rich nonlinear behaviours have been observed in microelectromechanical and nanoelectromechanical systems (MEMS and NEMS) resonators.This dissertation has performed a systematic study of nonlinear dynamics in various MEMS and NEMS resonators that appear to be single, two coupled, arrayed, parametric driven and coupled with multiple-fields, with the aim of exploring novel applications.

New study on dynamic performance of a single carbon nanotube resonator taking account of the surface induced initial stress has been performed. It is found that the initial stress causes the jumping points, the whirling and chaotic motions to appear at higher driving forces. Chaotic synchronization of two identical MEMS resonators has been theoretically achieved using Open-Plus-Closed-Loop (OPCL) method, and the coupled resonating system is designed as a mass detector that is believed to possess high resistance to noise. The idea of chaotic synchronization is then popularized into wireless sensor networks for the purpose of achieving secure communication. The arising of intrinsic localised mode has been studied in microelectromechanical resonators array that is designed intentionally for an energy harvester, which could potentially be used to achieve high/concentrated energy output. Duffing resonators with negative and positive spring constants can exhibit chaotic behaviour. Systematic calculations have been performed for these two systems driven by parametric pumps to unveil the controllability of chaos.

Based on the principle of nanomechanical transistor and quantum shuttle mechanism, a high sensitive mass sensor that consists of two mechanically coupled NEMS resonators has been postulated, and the mass sensor which can be realized in large-scale has also been investigated and verified. Furthermore, an novel transistor that couples three physical fields at the same time, i.e. mechanical, optical and electrical, has been designed, and the coupled opto-electro-mechanical simulation has been performed. It is shown from the dynamic analysis that the stable working range of the transistor is much wider than that of the optical wave inside the cavity.

Table of contents

List of figures

List of tables

Chapter 1

Introduction

1.1 What Are MEMS/NEMS Resonators

Microelectromechanical and nanoelectromechanical system (MEMS and NEMS) resonators are pivotal building blocks for modern electronic systems that can vibrate with a higher amplitude response at its modal resonance frequency [3]. Essentially speaking, the core of a MEMS/NEMS resonator can be seen as an oscillator that preferably operates at its resonant frequency, although it might appear to be with different shapes and subjected to various external environment. In order to have a clearer idea, the illustration has been presented visually in Fig. 1.1, where a doubly clamped cantilever has been employed to represent the vibrating component of a resonator, and the lumped model has been given correspondingly. From the Fig. 1.1 (a) and (b), it is seen that the resonators can be modelled as an oscillator

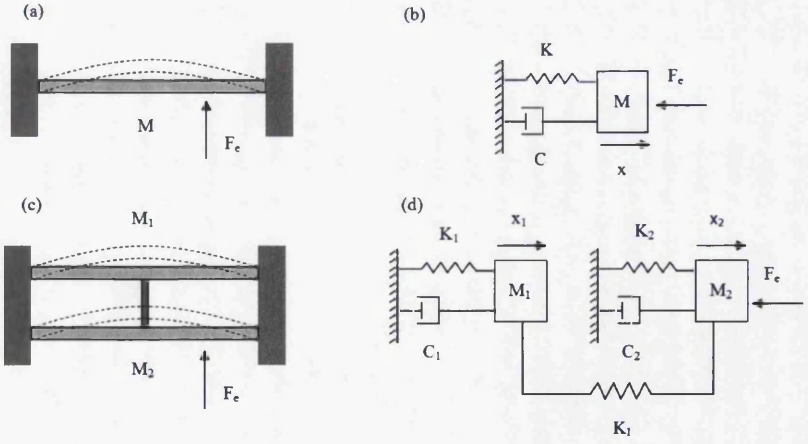

Fig. 1.1 Simplified resonators and their corresponding lumped models.

that has mass M and a stiffness K, subjected to an external driving F_e and a damping force

with ratio C (generally to the velocity of the device). Similarly, if the resonators are designed in the coupled way as indicated in Fig. 1.1 (c), it can be modelled by the coupled oscillators as well only by introducing a coupling coefficient K_I, and this idea can be generalized to the arrayed structure that has many resonators coupled together. Based on this analogy, the mathematical model of a single resonator shown in Fig. 1.1 (a) and the coupled one shown in Fig 1.1 (c) can be easily obtained by using Newtonian mechanics, as:

$$\begin{aligned} &M\ddot{x}+Kx+C\dot{x}=F_e \\ &\text{and} \\ &M_1\ddot{x}_1+K_1x_1+K_I(x_1-x_2)+C_1\dot{x}_1=0 \\ &M_2\ddot{x}_2+K_2x_2+K_I(x_2-x_1)+C_2\dot{x}_2=F_e \end{aligned} \tag{1.1}$$

respectively, where the damping force has been assumed to be linearly related to the velocity of the oscillator, and in the coupled model only M_2 is driven intentionally. The mathematical model in Eq. 1.1 can be extended for a more general case: arbitrary resonators coupled, provided the necessary considerations are being included .

Obviously, the modelling presented above is just a simple way for having a relative shallow impression of the MEMS/NEMS resonators. If more practical conditions were considered, such as the driving of the MEMS/NEMS resonators could be realized electrostatically or piezoelectrically, the damping ratio sometimes may not be a constant or not linearly varies with the velocity of the resonators and the restoring force of the resonators may not only linearly change with the displacement x, the model of Eq. 1.1 will become complicated. In fact, there already exists a famous model called Duffing resonator [4][5] that incorporates the force that is proportional to the cube of the displacement (K_3x^3) in order to consider the nonlinear effect introduced somehow, and it has been playing an very important role for investigating the dynamics of the MEMS/NEMS resonators, which is generally expressed in the following equation:

$$\ddot{x}+\delta\dot{x}+\beta x+\alpha x^3=F_e \tag{1.2}$$

where β and α are coefficients of linear and nonlinear stiffness. δ is the damping ratio. The β could be positive and negative. It should be noted that the Eq.1.2 has been normalized and re-arranged. For $\beta>0$, the Duffing resonator can be seen as a spring whose restoring force is expressed as: $F=-\beta x-\alpha x^3$. Further, depending on $\alpha>0$ or $\alpha<0$, the spring is called the hardened and softened, respectively. For $\beta<0$, the Duffing resonator describes the dynamics of a point mass in double potential well. The reading of the Duffing resonator can also stand from the perspective of energy that it is a Hamiltonian system, which has a

constant energy $E(t)$ if the $\delta = 0$:

$$E(t) = \frac{1}{2}\dot{x}^2 + \frac{1}{2}\beta x^2 + \frac{1}{4}\alpha x^4 \tag{1.3}$$

Given an initial energy E, the system will oscillate periodically keeping $E(t)$ as a constant, and corresponding to the two cases: $\beta > 0$ and $\beta < 0$, the $E(t)$ is forming a single-well potential and double-well potential, respectively, as shown in Fig. 1.2. However, if the damping force was considered, i.e. $\delta > 0$, the $E(t)$ of the system will not be a constant anymore, and instead the oscillator will gradually consume its energy and settle down at the one of its equilibrium positions finally. The dynamics of the Duffing resonator will become more complicated if various external driving included, such as the chaos may appear [6].

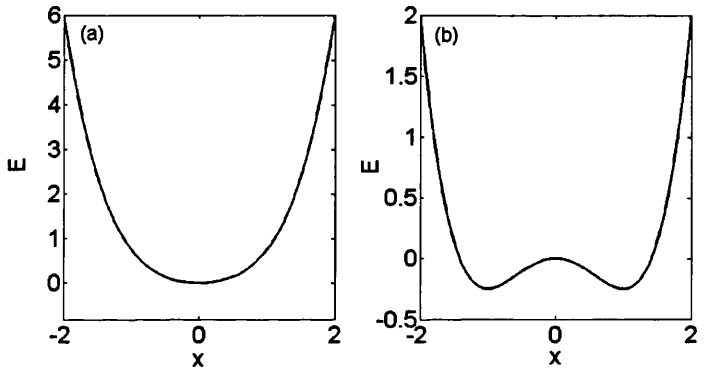

Fig. 1.2 Potential of the Duffing resonator when $\beta = 1$, $\alpha = 1$ and $\delta = 0$ in (a) and $\beta = -1$, $\alpha = 1$ and $\delta = 0$ in (b).

It is worth to mention that the modelling idea described above is more suitable for the resonators that are made in micro-scale while other modelling methods need to be adopted in some other cases. For example, when the resonator is made to be very thin and smaller (nano-scale) the Euler-Bernoulli beam theory needs to be employed [7][8], which is given by:

$$\rho A \frac{\partial^2 W(x,t)}{\partial t^2} = -EI \frac{\partial^4 W(x,t)}{\partial x^4} + T \frac{\partial^2 W(x,t)}{\partial x^2} \tag{1.4}$$

where $W(x,t)$ is the dynamical displacement of the beam at each point, x is the coordinate along the length of the beam, A is the cross section area of the beam, ρ is the mass density, T is the tension in the beam, E and I are Young's modulus and the moment of the inertia, respectively. It is seen from the Eq. 1.4 that the model gives the vibrating displacement at every point of the one-dimensional beam dynamically, instead of seeing the vibrating

components of the MEMS/NEMS resonators as a mass like in Eq. 1.1. This modelling has been widely employed and as well it will be used somewhere in the main body of this project.

The studying of MEMS/NEMS resonators are not simply a problem of vibration. It is truly a complex subject that could interact with multiple fields such as electrics [3], optics [9], quantum physics [10], magnetism [11] and piezoelectricity [12]. Along with the wide range of fabrication techniques and a variety of materials, makes the modelling of MEMS/NEMS resonators inherently a complex subject. The description above gives only an introductory remarks of MEMS and NEMS resonators from the point of view of mathematical modelling.

1.2 Motivations and Objectives

MEMS/NEMS resonators have been widely explored for a host of many applications such as sensors in various fields (mass, sound, liquid, force, distance, temperature, chemical etc.) [13][14][15][16][17][18][19][20], frequency generators for digital and mixed-signal circuits and actuators [21]. In particular, with the rapid advance of nanotechnology, the NEMS resonators that are characterized by high-Q factor and frequencies have been achieved, and they have been proved to be competent for ultra-sensing (force and charge detectors etc.) [22][23]. Moreover, by coupling the MEMS/NEMS resonators with other fields such as optics, they can be used as an platform for investigating the quantum phenomenon [24], taking the photon-phonon interactions [25] for example.

The rich nonlinear behaviours including the softening/hardening effect, pull-in [26], bifurcation [27], chaos and so on [28] have been readily observed in the MEMS/NEMS resonators, and these observations have inspired a wide interest among the researchers. They focus on investigating the origin of the nonlinearity, analysing and predicting the dynamical route for nonlinear behaviour [29][30], and most importantly, how to utilize the nonlinearity when it is wanted and control it when it is unwanted [31]. So far, methods for analysing the model of MEMS/NEMS resonators such as Melnikov's method [32] and secular perturbation have been developed [7]. Controlling the MEMS/NEMS resonator to operate favourably has been extensively studied by proposing many effective schemes [1]. A wide variety of applications ranging from switches, sensors to sophisticated mechanical signal processors based on the nonlinear behaviours have been realized too, and surprisingly some applications have been verified to perform more advantageous than working in the linear regime [33][34]. Various constructions of MEMS/NEMS resonators such as ring [14], grating [35], cylindrical [19], film [36], thanks to the advanced fabrication techniques, have been employed as a platform, and especially the NEMS resonators that have a high frequency-going beyond 1 GHz, relatively weak dissipation and high quality factors ($10^4 \sim 10^5$) have brought the

opportunities to dig the fundamentals of nonlinearities. In addition, the MEMS/NEMS resonators array which might be fabricated by tens to hundreds of coupled resonators allow the researchers to study the collective behaviours in the system that have many degrees of freedom, such as formation of extended patterns and intrinsically localized modes [37].

Although many achievements have been made, there are still many problems existing at the intersections of the MEMS/NEMS resonators with the nonlinear dynamics. Firstly, the modelling of the resonators, especially the ones in nano-scale, need to be further analysed as some effects playing an important role in the operation have been ignored or less understood. Secondly, more attention should be paid to explore the applications of nonlinear behaviours. Take chaos for example, the existing works [31][1][38] focus more on controlling it while there is enough room left to exploit it for novel applications. Thirdly, as the current development of MEMS/NEMS, they are designed in many cases intentionally coupled with other physical fields, which makes the whole coupled system more complicated and the involved nonlinear problems multidisciplinary. The applications based on these kinds of systems have been of interest and rarely touched.

It is author's objective to further understand the nonlinear dynamics, especially the chaos, in various MEMS/NEMS resonators and to explore unique applications. Therefore, the models studied in this project will span a wide scope ranging from the micro-scale, the single to the nano-scale, the coupled, the parametric and the arrayed, and more importantly, the models that are interacted with other fields such as optics and quantum physics. Theoretically, it is a priority to investigate and analyse the fundamentals of the nonlinearities and the working principles of the various models, trying to discuss the problems in a comprehensive way. For example, How the model of nanotube resonators that incorporates the initial surface stress is deduced? How does the parametric term affect the two types of Duffing models? What is the working principles of quantum shuttle mechanism? Could the working regime of chaos be used in devices? Along with the analysis of various models, the goal comes about how to utilize the distinct behaviours and explore the novel applications that have not ever been considered and are believed to be important for the development of this field.

1.3 The Basic of Nonlinear Dynamics

Since the nonlinear dynamics in the MEMS/NEMS resonators plays an important role, and also exists as the theoretical basis of this project, it is necessary to introduce some basic concepts here.

1.3.1 Chaos

The well-known butterfly effect essentially reflects the most important character of the chaos behaviour in nonlinear dynamical systems: sensitivity to the initial conditions. Namely, in a chaotic dynamical system, two slightly different initial states will finally be evolved into two trajectories that have a huge difference. Therefore, any small perturbations in a chaotic dynamical system will cause the present state to be completely unpredictable in the future.

It is helpful to illustrate the chaos by employing the famous Lorenz model [2], which is expressed as:

$$\begin{aligned} \dot{x} &= \sigma(y-z) \\ \dot{y} &= rx - y - xz \\ \dot{z} &= xy - bz \end{aligned} \tag{1.5}$$

where σ, r and b are parameters, and if they are taken as: $\sigma = 10$, $b = 8/3$ and $r = 28$, the Lorenz Eq. 1.5 will performing chaotic behaviour, as shown in Fig. 1.3, where the two-dimensional chaotic attractor has been plotted. In the Fig. 1.3, the red arrow indicates

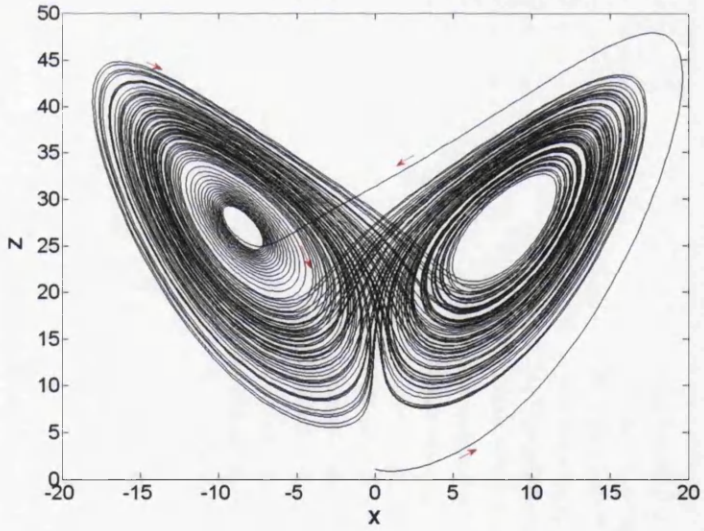

Fig. 1.3 The chaotic attractor of Lorenz equation.

an initial point that evolves according to the Lorenz equation. Under such a parameters setting, any trajectories that start from any initial points will not settle down in a periodic or quasi-periodic state, conversely, it will spiral around the right and left centre in a random way, i.e. the repetitions around each side unpredictably, while the whole dynamical trajectory is bounded in a certain area, which is called strange attractor. The strange attractors are

commonly seen in nonlinear dynamical systems. They essentially reflect the game between the deterministic and chaotic state. The strange attractors can be found in the MEMS/NEMS systems as well, and this will be studied in the main text.

1.3.2 Bifurcation

The chaotic behaviour always comes along with the taking place of bifurcation [39]. For example, the chaos in Lorenz equation, it actually had gone through two main bifurcations with the varying parameter r ($\sigma = 10$, $b = 8/3$) before the chaos arrived. The bifurcation in a nonlinear dynamical system is defined as the changes in the sense of quantity and quality of the system equilibrium points as one or more parameters varying. Considering the example shown in Fig. 1.4 (a) in which a solid ball has been put at a certain height where the potential energy of the ball is just enough for the ball to settle down at point 1 finally because of the energy dissipation, but if the initial height was put higher, as shown in Fig. 1.4 (b) the ball may cross the first peak and settle down at point 2 after many ups and downs. Here, the height can be seen as the bifurcation parameter in this example, depending on which the final equilibrium point is changed. A simple nonlinear discrete dynamical system [39] can also been employed here to explain the bifurcation, which is given by:

$$x_{n+1} = 1 - ux_n^2, \qquad u \in (0,2] \tag{1.6}$$

where the x_n is the state variable, and it is iterated discretely with n. u is the parameter that is varied intentionally for studying bifurcation, and here it is varied in the range $(0,2]$. By varying the u with a step 0.01, and iterating the system for $n = 1000$, the value of x_{800} to x_{100} have been recorded at each step of u, as shown in Fig. 1.5. It is seen from Fig. 1.5 that there is only one stable state value in the first part ($0 < u < 0.75$) of the varying range u, which means the system has dropped into a stable point as the iteration. While as the u is increased over ~ 0.75, the final state has became to be shuttling between two stable points. Actually, the system has occurred a bifurcation at $u \sim 0.75$, where the one stable solution of the system lost its stability and another two stable solutions appeared. This kind of bifurcation has occurred subsequently as the u varying until the final state is evolved into a chaotic state ($u \sim 2$).

In a nonlinear dynamical system, there are many types of bifurcation. For example, saddle-node bifurcation which represents the cases two equilibrium points move toward each other, collide, and mutually annihilate. Transcritical bifurcation is talking about the case one equilibrium point of the considered systems never get lost but changes its stability with the

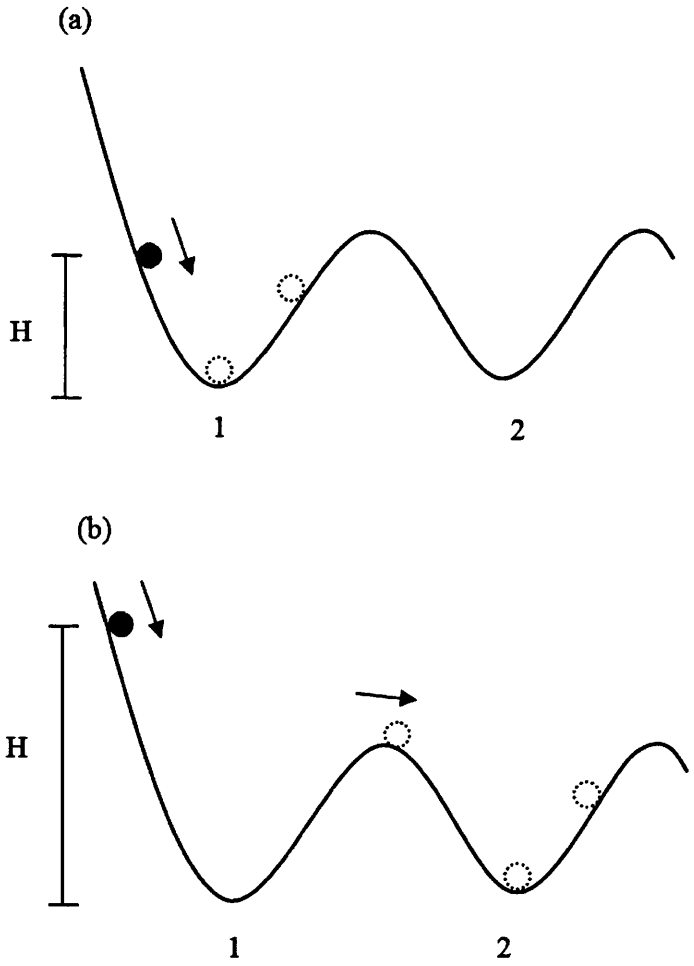

Fig. 1.4 A representative diagram of bifurcation.

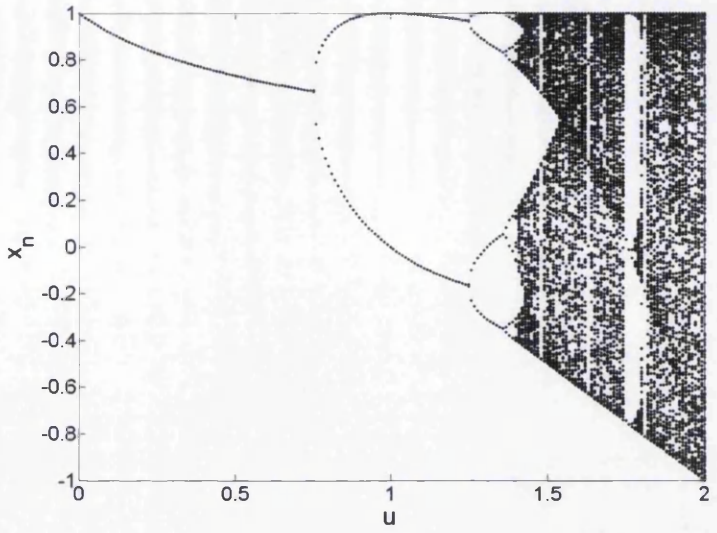

Fig. 1.5 Bifurcation diagram of Eq. 1.6.

varying of chosen parameters. Another commonly seen type is called pitchfork bifurcation, in which the equilibrium points appear and disappear in symmetrical pairs.

1.4 Thesis Overview and Achievements

In this thesis, there are eight chapters. After this short introduction chapter, it will go into the main body of the thesis (from chapter 2 to chapter 7), and the last is conclusion chapter.

In chapter 2, the dynamical model of a carbon nanotube resonator that incorporates the initial surface effect will be derived, and based on the model the impact of surface induced initial stress on the nonlinear dynamics will be investigated. In the last section, the potential application of the carbon nanotube resonator for a accelerator will be explored. This chapter can be served as an introduction for the NEMS resonator modelling. It is found that the initial strain-induced surface effect plays a crucial role in the dynamics of the carbon nanotube resonator. Specifically, the surface effect can increase the resonant frequency of the resonator and the threshold of occurrence of the whirling and chaotic motion. Besides, the proposed accelerator based on the nanotube resonator has a higher sensitivity comparing with other MEMS accelerator that are made in micro-scale.

In chapter 3, the chaotic synchronization between two MEMS resonators will be realized, and a novel mass sensor based on the mechanism of synchronization will be proposed and numerically validated. Moreover, the idea of the chaotic synchronization will be implemented for the use in the secure communication within a wireless sensor network (WSN). By

numerical simulation with the practical parameters, it is proved that designing the mass sensor by using two coupled resonators is noise-robust, and also can work in a wider range which spans both in linear and nonlinear regime. Encrypting the information by the chaotic signal can enhance the security of the sensor network, which has the potential application in future's wireless communication network design.

In chapter 4, the intrinsic localized mode (ILM) in an energy harvesting array that consists 64 pairs of microelectromechanical beams will be investigated, and whether the ILM is beneficial for energy harvesting will be discussed. It takes the practical considerations such as experimental accessible parameters and practical materials into account for simulation, and it is found that the charge generation of the cantilever array when it is in ILM mode generates higher output than the normal state, which sheds the light on how to increase the generation efficiency of the generators based on the cantilever array.

In chapter 5, the chaos controllability of the parametric term in Duffing resonators, either self-contained or intentionally added, will be systematically analysed, and the findings will be quantitatively explained by using the Melnikov's method. As these two types of resonators are representative in the MEMS/NEMS field, the investigation of them concentrating on the nonlinear regime is beneficial for future's designs. Here, by calculating the effect of the parametric modulation, it is found that for the two different type of resonators, the controllability from the parametric pump is different but they both have the effect to control the chaotic behaviour.

In chapter 6, a nano-mechanical transistor that is based on the quantum shuttle mechanism will be introduced, and by designing a weakly coupled beam resonators, a novel mass sensor that works in a self-excitation regime is realized. Furthermore, in the second part, the possibility of realizing the mass sensor in the large-scale will subsequently be discussed. In this chapter, the model of the resonator that couples with electrical field will be employed and analysed. The nano-mechanical transistor-based sensor are numerically proved to have a high sensitivity which could be used for sensing the quantum effect. Also, its realization has the feature that transaction readout circuit can be omitted. This mass sensor then has been extended into large scale which is supposed to be more practical.

In chapter 7, by taking the optical cavity as a resonator, a device that couples three fields (optical, electrical and mechanical) is for the first time proposed. The working range of the device both in the linear and nonlinear regime will be investigated in detail. It is found that the motion of the optical cavity is tiny which provides a reasonable distance for occurrence of quantum tunnelling, and this can be modulated by the taped laser pump. Furthermore, with increasing the pump power, the optical field inside of the cavity can behave in chaotic

behaviour while the motion of the mechanical part of the cavity is still in linear regime. This finding provides new clues in designing the transistors that work with multi-fields involved.

Chapter 2

Nonlinear Dynamics of Doubly Clamped Carbon Nanotube Resonator

2.1 Background

Carbon nanotube (CNT) resonators due to their remarkable properties such as high quality factor, low effective mass, high frequency and pristine electron states they hold have been widely explored for applications. Particularly, in ultra-sensing field, for example, Hsin-Ying Chiu et al [40] have realized the atomic-scale mass sensing by employing a doubly clamped carbon nanotube nanomechanical resonators. B. Lassagne et al [41] have demonstrated carbon nanotube-based ultra-sensitive magnetometers that enable one to assess the magnetic properties of a single and very small nano-object. An experiment for measuring the weak force was conducted by J. Moser at al [42], in which the force detection sensitivity can reach 12 zN $Hz^{-1/2}$ at temperature of 1.2 K. Other explorations in atoms/molecules detection [43][44], strain sensing [45] and biological molecules sensing in viscous fluids [17] have attracted much attention as well. Beyond these, CNT resonators have been employed for addressing the fundamental problems in the quantum regime. For instance, recently, P. Stadler et al. have demonstrated that ground state cooling of a CNT can be achieved by a spin-polarized current [46].

Alongside the explorations for various applications, the investigations of distinct properties of the CNT resonators have also been extensively conducted. Experimentally, quality factors of up to 5-million has been observed by using ultra-low-noise method [47]. Z. Y. Ning et al. [48] have found the resonant frequency of a CNT resonator can be tuned not only transversally by a gate voltage but also the axial strain applied through directly pulling of the

CNT. Capacitive spring softening effect in single-wall carbon nanotube has been reported by Chung Chiang Wu et al. [49].

However, there is a key thing existing behind the explorations that is to accurately model the motion of the CNT resonators. So far, molecular dynamics (MD) simulations and continuum mechanics approaches have been widely adopted for modelling the motion of the CNT resonators, both of which have been playing an important role in collaborating with the experiments, although they have their own weak points as for modelling different cases. [50].

In terms of continuum mechanics model, i.e. elastic beam model, it is less computationally expensive compared with MD, and can also provide a reliable way for getting physical insight into a problem, with limitations in solving the case with discontinuity at the atomic scale though. Many research groups have employed continuum mechanics models to investigate the dynamics both in linear and nonlinear regime. In reference [51], the authors have examined the single-wall carbon nanotube by continuum mechanics based approach, and the validity and accuracy of the method have been proved via investigating different cases. By employing Euler–Bernoulli continuum beam theory, in work [52], I.K.Kim and S.I.Lee have studied the nonlinear resonances of a single-wall carbon nanotube resonator, where they have demonstrated that the CNT will go through various nonlinear phenomenon with increasing electrostatic driving. Parallel to this, an analytical study has been conducted in [53], still by employing continuum mechanics model, the authors have derived the criterion for the onset of the nonlinear jump phenomena and the non-planar, whiling motion in CNT resonator, and the result they obtained agrees well with the experiment [54]. Inspired by this work, Chen et al. [55] carried a detailed bifurcation analysis for a electrostatically driven silicon nanowire resonators and concluded that the extensive chaotic motion is expected to arise as the excitation magnitude increases to such an extent. However, in these two works, they both have ignored the role of surface effect, which actually plays an important role in the motion of the NEMS resonators [56], especially for the resonators that have a relatively smaller transverse dimension.

It is necessary to consider the surface effect when one tries to model the nano-scale resonators accurately because the surface effect have impacts on the mechanical properties of the nanostructures such as effective bending rigidity and resonance. In fact, there are already some works studying the importance of the surface effect [57][58][59][60]. One of the work that needs to be highlighted is [61], in which the authors have systematically derived a new formulation of the Euler–Bernoulli beam model that incorporates surface-induced initial stresses. By comparing their result with the existing experimental measurements and the widely used Young–Laplace model, the validity of the proposed model has been proved. However, the work done so far on surface effect are rarely related to nonlinear regime of

the models they adopted, although some work may slightly touched the interplay between the surface effect and the nonlinearity of the models [56]. Therefore, how the surface effect is playing its role on the nonlinear behaviours of the nano devices is becoming an open question, especially when the device going into a strong nonlinear regime where the chaotic state may arise. In addition, from the viewpoint of applications, this research topic is also important, as the nanoresonators that are working in nonlinear regimes have been proven to have high sensitivity in mass detection [33] and can be used to improve the precision of measuring the resonant frequency [34]. In fact, some applications have already been realized. For example, Rueckes et al. [62] demonstrated that a suspended CNT can be used as a memory device based on its nonlinear pull-in behaviour, and very recently, in reference [63], the authors presented a nonlinear optical mass sensor based on a doubly clamped suspended CNT resonator in all-optical domain.

In this chapter, it will start by introducing the concept of surface effect (specifically the surface-induced initial stress), and then will derive the equation that considers both in-plane and out-plane motions of a single-wall CNT resonator. Based on the derived equation, nonlinear behaviours such as jump phenomena, whirling motion and chaotic vibration will be investigated. By comparing the cases with and without surface effect of the model, the result on how the surface effect affect the nonlinear behaviours will be discussed. Lastly, exploring the single-wall CNT resonator for application as an accelerator will be presented. It should be noted that the investigation of the surface effect also can be applied to other types of the devices such as multi-wall carbon nanotube resonators, as in the nano-scale the surface-induced initial stress is unavoidable.

2.1.1 Surface-Induced Initial Suface Stress

The importance of considering the surface-induced stress for modelling the small nano-structures has been argued in [61]. If there is an initial surface stress τ_0 presented in a nanostructure, it will induce strain both inside and surface of the structure depending on the boundary conditions, and the induced axial initial stress $\widetilde{\sigma}_{xx}$ and the surface stress can be obtained by:

$$\begin{aligned} \widetilde{\sigma}_{xx} &= E\widetilde{\varepsilon}_{xx} \\ \widetilde{\tau}_{xx} &= \tau_0 + E_s\widetilde{\varepsilon}^s_{xx} \end{aligned} \tag{2.1}$$

where the E and E_s are the Young's modulus of the bulk and surface of the nanostructure, respectively. $\widetilde{\varepsilon}_{xx}$ and $\widetilde{\varepsilon}^s_{xx}$ are the initial stain induced in the bulk and surface of the nanostructure, respectively. They are equal to each other at the surface according to the continuity

condition. The $\widetilde{\varepsilon}_{xx}$ and $\widetilde{\varepsilon}^s_{xx}$ are determined by the potential energy [64], while for a nanotube resonator with fixed/fixed boundary condition, it has $\widetilde{\varepsilon}_{xx} = \widetilde{\varepsilon}^s_{xx} = 0$. The $\widetilde{\sigma}_{xx}$ and $\widetilde{\tau}_{xx}$ affect the motion of the nanotube and will be incorporated into calculating the total bulk and surface stress, as shown in Fig. 2.1.

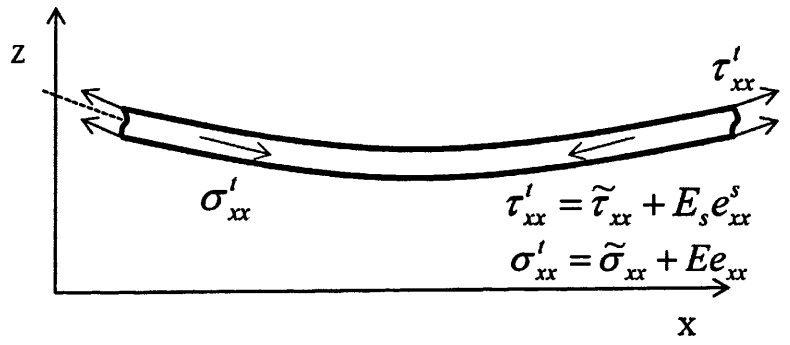

Fig. 2.1 Schematic diagram of the surface strain (red) and bulk strain (blue) of carbon nanotube when it is deformed.

2.2 Model Construction

As shown schematically in the Fig. 2.2, the resonator studied in this chapter consists of a single-wall CNT (SWCNT) which is suspended above a trench with double ends clamped and a bottom electrode. The initial distance between the SWCNT and the bottom electrode is h when the SWCNT is in static state. The diameter, length and wall thickness of the SWCNT are represented by d, L and b respectively. In this model, the bottom electrode serves as the gate, and when an external voltage V is applied the nanotube will be vibrating accordingly, due to the alternate electrostatic force induced between the bottom electrode and nanotube. It is worth to mention that the bottom electrode do play a role in the generation of electrostatic force that is between the single-wall nanotube. But in the following analysis, this effect is ignored as the single-wall CNT considered is very small compared with area of the bottom electrode. For mathematically modelling the resonator, it can be treated as a doubly clamped, one-dimensional oscillating mechanical beam, and the Euler-Lagrange theory can be employed to derive the dynamical equations that describes the motion of the resonator. Because of the large surface-to-volume ratio the surface effect in the model will be considered in following. Firstly, the initial surface stress can be represented by: $\widetilde{\tau}_{xx} = \tau_0 + E_s \widetilde{\varepsilon}^s_{xx}$ as given in Eq. 2.1, where again τ_0 is the surface stress when strain is zero. $\widetilde{\varepsilon}^s_{xx}$ and E_s are the initial surface strain in the relaxed state and surface elastic modulus, respectively. By employing the

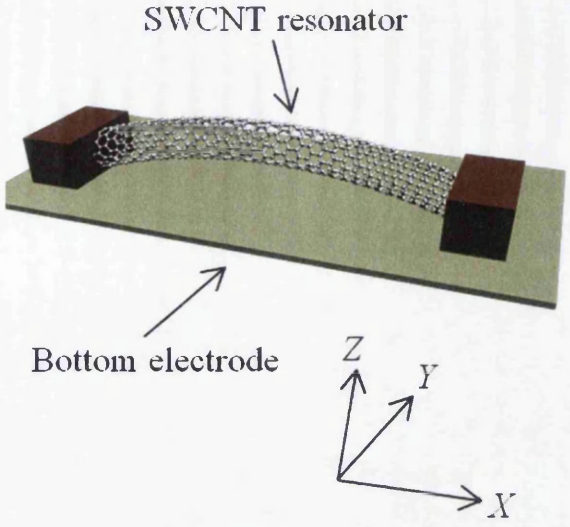

Fig. 2.2 Schematic diagram of a single-wall CNT doubly clamped resonator.

established theory [61], the surface stress can be expressed as: $\tau_{xx}^t = \widetilde{\tau}_{xx} + E_s e_{xx}^s$, where e_{xx}^s equals the value of Green-Lagrangian strain e_{xx} at the surface. The e_{xx} can be expressed as:

$$e_{xx} = -z\frac{\partial^2 Z}{\partial x^2} + \frac{1}{2}\left(z\frac{\partial^2 Z}{\partial x^2}\right)^2 + \frac{1}{2}\left(\frac{\partial Z}{\partial x}\right)^2 \tag{2.2}$$

The bulk stress σ_{xx}^t have the similar linear relation with e_{xx}, which is: $\sigma_{xx}^t = E e_{xx}$, where E is the bulk Young's modulus. The initial stress in bulk has been assumed to be 0 as the nanotube in our model is doubly clamped. Thus, the surface and bulk strain energy per unit volume E_s and E_b can be obtained as:

$$E_s = \int_0^{e_{xx}^s} \tau_{xx}^t de_{xx}^s = (\widetilde{\tau}_{xx} + \frac{1}{2}E_s e_{xx}^s)e_{xx}^s \tag{2.3}$$

$$E_b = \int_0^{e_{xx}} \sigma_{xx}^t de_{xx} = \frac{1}{2}E e_{xx}^2 \tag{2.4}$$

Then, the incremental potential energy of the nanotube can be derived by using theory of Biot [65], which is given by:

$$\Delta U_1 = \int (E_s - \widetilde{\tau}_{xx}\widetilde{\varepsilon}_{xx}^s)dC + \int (E_b - \widetilde{\sigma}_{xx}\widetilde{\varepsilon}_{xx})dA = \frac{1}{2}[EI_m + \widetilde{\tau}_{xx}I_s + E_s I_s]\frac{\partial^2 Z}{\partial x^2} + \frac{1}{2}\widetilde{\tau}_{xx}C\left(\frac{\partial Z}{\partial x}\right)^2 \tag{2.5}$$

Where C is the circumference. $I_m = \pi/4(d^4/16 - (d/2-b)^4)$ and $I_s = \pi/4(d^3/8 - (d/2-b)^3)$ are the inertia moment and the surface inertia moment, respectively. The bending

induced tension is leading to another incremental potential energy ΔU_2, which can be calculated by the following equation:

$$\Delta U_2 = \frac{1}{2}\left\{\frac{EA}{2L}\int_0^L\left[\left(\frac{\partial Z}{\partial x}\right)^2+\left(\frac{\partial Y}{\partial x}\right)^2\right]dx\right\}\left(\frac{\partial Z}{\partial x}\right)^2 \tag{2.6}$$

Unlike the previous work [61], in the above equation the bend mode in Y-direction has been taken into account. The kinetic energy per unit length of the nanotube can be easily obtained by:

$$T = \frac{1}{2}\rho A\left(\frac{\partial Z}{\partial x}\right)^2 \tag{2.7}$$

where ρ is density of the nanotube and A is the cross-section area. The action of Euler-Lagrange equation for the nanotube can be calculated by combining Eqs. 2.5, 2.6 and 2.7, then it arrives:

$$S = \int_0^L (T - \Delta U_1 - \Delta U_2)dx \tag{2.8}$$

The Lagrangian can be obtained by:

$$\begin{aligned} L_a =& \frac{1}{2}\rho A\left(\frac{\partial Z}{\partial x}\right)^2 - \frac{1}{2}[EI_m + \tilde{\tau}_{xx}I_s + E_sI_s]\left(\frac{\partial^2 Z}{\partial x^2}\right)^2 \\ & - \frac{1}{2}(\tilde{\tau}_{xx}C + \frac{EA}{2L}\int_0^L\left[\left(\frac{\partial Z}{\partial x}\right)^2+\left(\frac{\partial Y}{\partial x}\right)^2\right]dx)\left(\frac{\partial Z}{\partial x}\right)^2 \end{aligned} \tag{2.9}$$

Based on the Euler–Lagrange beam theory and by substituting Eq. 2.9 into the following Euler–Lagrange equation:

$$\frac{\partial L_a}{\partial Z} - \frac{\partial}{\partial t}\left(\frac{\partial L_a}{\partial \dot{Z}}\right) - \frac{\partial}{\partial x}\left(\frac{\partial L_a}{\partial Z_x}\right) + \frac{\partial^2}{\partial x^2}\left(\frac{\partial L_a}{\partial Z_{xx}}\right) = 0 \tag{2.10}$$

the dynamical equation for describing the motion in Z-direction can be derived, as below:

$$\begin{aligned} [EI_m + \tilde{\tau}_{xx}I_s + E_sI_s]\frac{\partial^4 Z}{\partial x^4} - (\tilde{\tau}_{xx}C + \frac{EA}{2L}\int_0^L\left[\left(\frac{\partial Z}{\partial x}\right)^2+\left(\frac{\partial Y}{\partial x}\right)^2\right]dx)\frac{\partial^2 Z}{\partial x^2} + \rho A\frac{\partial^2 Z}{\partial t^2} \\ = F_e + F_f^Z \end{aligned} \tag{2.11}$$

where the relations: $\partial L_a/\partial Z = 0$, $\partial L_a/\partial \dot{Z} = \rho A \partial Z/\partial t$ and $\partial L_a/\partial Z_x = -(\widetilde{\tau}_{xx}C + \int_0^L [(\partial Z/\partial x)^2 + (\partial Z/\partial x)^2]dx)\partial Z/\partial x$ have been used.

It should be noted that the applied electrostatic force F_e and viscous damping force F_f^Z have been added to the right side of Eq. 2.11, and their explicit form will be given later. Similarly, the dynamical motion of the nanotube in Y-direction can be derived in the same way, which has the similar form with Eq. 2.11, as below:

$$[EI_m + \widetilde{\tau}_{xx}I_s + E_sI_s]\frac{\partial^4 Y}{\partial x^4} - (\widetilde{\tau}_{xx}C + \frac{EA}{2L}\int_0^L \left[\left(\frac{\partial Z}{\partial x}\right)^2 + \left(\frac{\partial Y}{\partial x}\right)^2\right]dx)\frac{\partial^2 Y}{\partial x^2} + \rho A\frac{\partial^2 Y}{\partial t^2} = F_f^Y \tag{2.12}$$

where the added F_f^Y represents the viscous damping force in Y-direction. The explicit form of $F_f^{Y,Z}$ and F_e have been studied in [55], and they can be expressed as:

$$F_e = -\frac{\pi\varepsilon_0 V^2(t)}{(Z+h)[ln(4\frac{Z+h}{d})]^2} \approx -\frac{2\pi\varepsilon_0 V_{dc}V_{ac}cos(\omega_d t)}{h[ln\frac{4h}{d}]^2} \tag{2.13}$$

$$F_f^{Y,Z} = -\frac{\pi P d}{4v_T}\partial_t\{Y,Z\} \tag{2.14}$$

where in Eq. 2.13, the $V = V_{dc} + V_{ac}cos(\omega_d t)$ is the applied driving voltage, with V_{dc} and V_{ac} are dc and ac components of the potential, and the ω_d is the driving frequency. In Eq. 2.14, the $v_t = \sqrt{k_B T_k/m}$ is air molecule velocity at temperature T_k and pressure P, where k_B is the Boltzmann constant and m is the average molecular mass of air.

The general form of the dynamical model of the resonator have been derived as given by Eqs. 2.11 and 2.12. Next, the Galerkin's method [66] will be employed to solve it. Firstly, it is assumed that $Z(x,t) = z(t)\varphi(x)$, $Y(x,t) = y(t)\varphi(x)$, where the $z(t)$ and $y(t)$ are displacement of the resonator in Z- and Y-directions, respectively. The $\varphi(x)$ is a deflection eigenmode function that satisfies the boundary conditions $\varphi(0) = \varphi(L) = \varphi''(0) = \varphi''(L)$, and its explicit form is given by: $\varphi(x) = (2/3)^{1/2}[1 - cos(2\pi x/L)]$. According to the Galerkin's method, by multiplying the $\varphi(x)$ on both sides of the Eqs. 2.11 and 2.12 and integrating by parts from 0 to L. The ordinary differential equations (ODEs) that describe the dynamics of the resonator in Z- and Y-directions can be derived, as:

$$\begin{aligned} &\ddot{z} + \omega_0^2 z + \alpha z(z^2 + y^2) + \beta\dot{z} = -2F_0 cos(\omega t) \\ &\ddot{y} + \omega_0^2 y + \alpha y(z^2 + y^2) + \beta\dot{y} = 0 \end{aligned} \tag{2.15}$$

where $\omega_0 = (2\pi/L)^2\sqrt{(EI_m)^*/3\rho A(1+P^*L^2/4\pi^2(EI_m)^*)}$, and in which

$$\begin{aligned}
&(EI_m)^* = EI_m + \widetilde{\tau}_{xx}I_s + E_sI_s \\
&P^* = \widetilde{\tau}_{xx}C, \beta = \pi Pd/(4\nu_t\rho A), \alpha = E/18\rho(2\pi/L)^4 \\
&F_0 = (\sqrt{2/2}/\rho A)\pi\varepsilon_0 V_{dc}V_{ac}/(h(ln(4h/d))^2)
\end{aligned} \tag{2.16}$$

Some integrations that have been involved for carring out the Eq. 2.15 are:

$$\begin{aligned}
&\int_0^L (d^2\varphi/dx^2)^2 dx = \frac{16\pi^4}{3L^3} \\
&\int_0^L (d\varphi/dx)^2 dx = \frac{4\pi^2}{3L} \\
&\int_0^L \varphi^2 dx = L \\
&\int_0^L \varphi dx = \sqrt{\frac{2}{3}}L
\end{aligned} \tag{2.17}$$

2.3 Calculation and Results Analysis

2.3.1 Jumping and Whirling

In this section, the numerical simulation of on Eq. 2.15 will be carried out, and the comparison between the two cases: with and without surface effect, will be presented. The parameters taken for the simulation are [55] [67]: $L = 100$ nm, $b = 0.066$ nm, $d = 0.548$ nm, $\rho = 1350$ kg/m^3, $E = 5.5 \times 10^{12}$ pa, which is taken according to the motions. $h = 500$ nm, $k_B = 1.38 \times 10^{23}$, $\varepsilon_0 = 8.85 \times 10^{-12}$ and $m = 5.6 \times 10^{-26}$ kg. It should be mentioned that the parameters taken in this work are seen as constant even though they are varying with the size of the model studied. Here, it is focused on investigating the surface effect on nonlinear dynamics of the nanotube resonator, and these parameters will not change the essence of the problem. Therefore, only one group of the parameters have been considered.

Firstly, the vibration amplitude in Z- and Y- directions of the resonator versus frequency $\omega \in [0.9\omega_0 1.2\omega_0]$ under different driving voltage V_{ac} have been calculated in Fig. 2.3. Figs. 2.3 (a) and 2.3 (b) is the case without surface effect ($E_s = 0$, $\widetilde{\tau}_{xx} = 0$). It is shown in Fig. 2.3 (a) that the vibration is in linear regime at first, and when the V_{ac} is increase to 0.7 V the jumping behaviour is observed, which is a common nonlinear behaviour in resonators. It is also shown that in Fig. 2.3 (a) the jumping gap is getting wider as the driving voltage is increased over 0.7 V, which means that the nonlinear factor affects the vibration more and more. In the Fig. 2.3 (b) the vibration amplitude in Y-direction has been studied, and it

is seen that only after the driving voltage increased to 1.5 V, the Y amplitude is becoming comparable with the Z-direction. What happens if initial surface effect is considered? Here, the $E_s = 5.19$ N/m [68], $\widetilde{\tau}_{xx} = 0.05$ N/m have been taken for calculation. As shown in the Figs. 2.3 (c) and (d), where the amplitude in Z and Y-direction are both performing differently compared to Figs. 2.3 (a) and (b). In Fig. 2.3 (c) the jumping behaviour occurs at a higher driving voltage: $V_{ac} = 1.5$ V and the curves representing the relations between V_{ac} and ω have become more condensed and sharper, and in Fig. 2.3 (d) the amplitude in Y-direction is becoming comparable at a higher driving voltage too: $V_{ac} = 3.3$ V. But it should be noted that the ω_0 of the case with the initial surface effect considered has been increased to 4.59×10^{10} Hz. The swing driving frequency have been varied in the same range of $0.9\omega_0$ to $1.2\omega_0$ with the case without initial surface effect. For illustrating the process as to how and when the

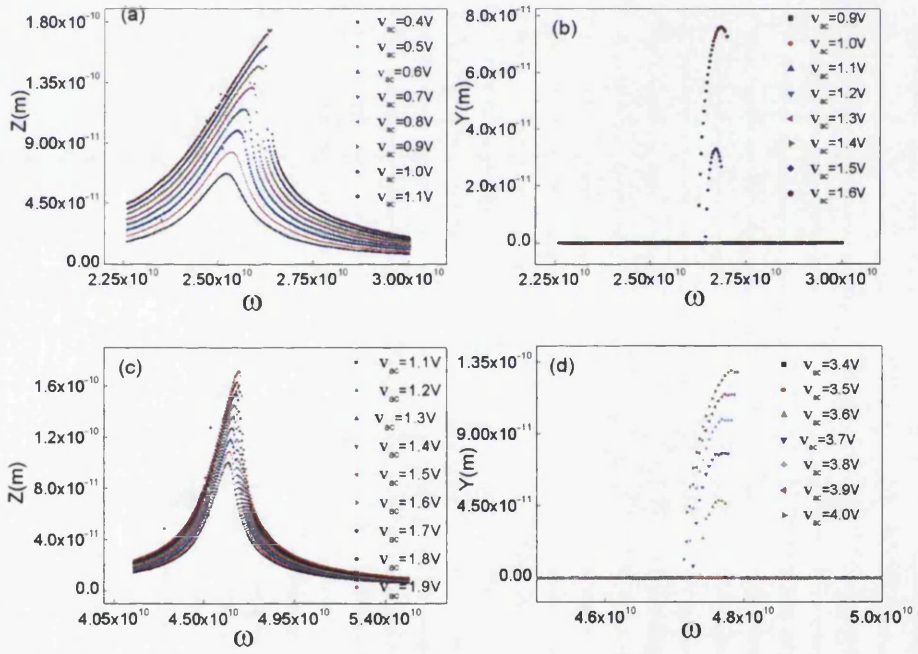

Fig. 2.3 Calculated vibration amplitudes in Z-and Y-directions of the system without surface effect under different driving voltage V_{ac} ((a) and (b)). Results of the system with surface effect ((c) and (d)).

whirling motion is arising, the amplification of the vibration in Y-direction has been carefully studied, as shown in Fig. 2.4. The driving frequency are both set equally to ω_0 but with different value according to the two cases: without surface effect in Figs. 2.4 (a) and (b) and with surface effect in Figs. 2.4 (c) and (d). Under the driving voltage varying in the range of (0.6 V - 5.6 V) and (0.5 V - 8.1 V) in the Fig. 2.4 (a) and Fig. 2.4 (c), respectively,

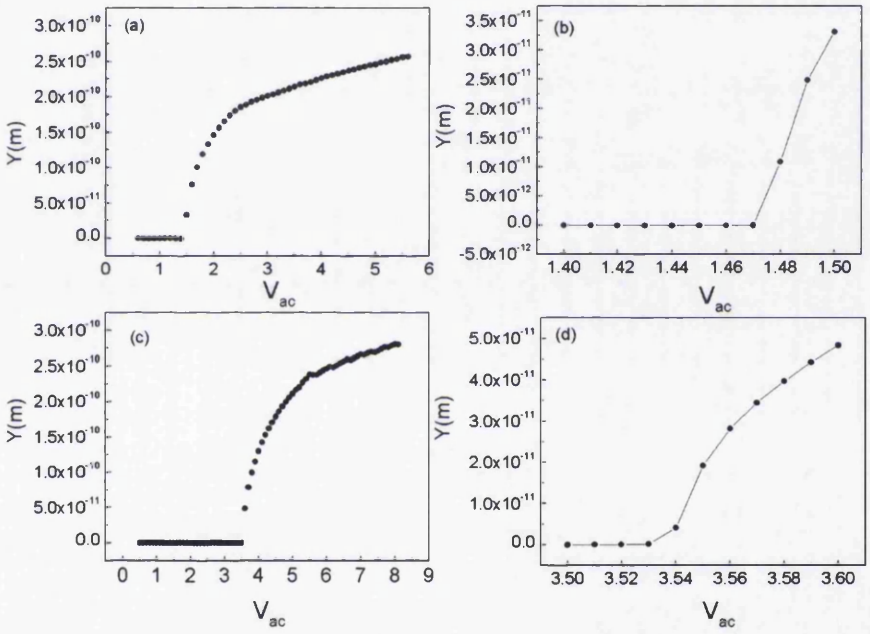

Fig. 2.4 Calculated detailed relation between vibration in Y and applied V_{ac}; without surface effect ((a) and (b)); with surface effect ((c) and (d)). The driving frequency in the two cases are taken to be ω_0.

it is seen that the whirling motion when the amplitude has the comparable value occurs at different driving voltage. The Y amplitude are all nearly 0 in Fig. 2.4 (a) and Fig. 2.4 (c) at the beginning, and then they all go through a sharply jumping. After that the slope of the increasing trend are getting smaller. The amplified process of the arising of the whirling motion have also presented in Fig. 2.4 (b) and Fig. 2.4 (d), respectively, where it is seen the whirling motion arises differently. The case without initial surface effect shown in Fig. 2.4 (b) is abrupt while the one in Fig. 2.4 (d) seems to be moderate.

2.3.2 Bifurcation and Lyapunov Analysis

The bifurcation diagram could give a clearer picture about how the motion of CNT resonator is evolving under different driving voltage. The bifurcation diagram of the Eq. 2.15 without and with initial surface effect have been plotted in Fig. 2.5 and Fig. 2.6, respectively. It is shown in Fig. 2.5 that the amplitudes in Z-direction are performing a multiple phase picture under the driving voltage V_{ac} increased from 20 V to 25 V. When the V_{ac} is set in the range of [20 V - 21.47 V], the resonator is observed to be vibrating at one periodical state, and then the vibration evolves into a multiple periodical state after the driving voltage increased to the range of (21.47 V - 22.25 V). As the driving voltage increasing higher, the vibration state get back to one periodical state, but it splits into main branches at $V_{ac} = 23.25$ V soon. As the amplitude varying along the two branches, it is evolving into the chaotic state at $V_{ac} = 24.25$ V.

While, the bifurcation diagram with considering the initial surface effect is exhibiting totally different with the same driving voltage range. It is shown that in Fig. 2.6 that the most part of the vibration is in a multiple periodical state, and only in some short driving interval, the one periodical states appear.

Comparing the bifurcation diagrams of Figs. 2.5 and 2.6, it is seen that there are big differences between the two cases. In the Fig. 2.5 when there is not surface effect considered the dynamics of the resonator has gone though multiple phases. It is because the resonant frequency changes by a large extent when the surface effect is considered or not. When there is surface effect considered, the frequency of the resonator is increased to 4.59×10^{10} so the diagram in Fig. 2.6 performs monotonously as the threshold of bifurcation to other phases is increased. If the driving voltage is increased to a larger value, the bifurcation of the case in Fig. 2.6 will perform to be diverse too.

The phase portraits (z_1 vs. z_2) in Fig. 2.7 have been plotted, where the dynamics of the resonator is performing diversely ranging from one periodical state to chaotic state (Figs. 2.7 (a) to (e) is without initial surface effect and Figs. 2.7 (f)-(h) is with initial surface effect). The Lyapunov exponents (λ) has always been used to characterize the dynamics of

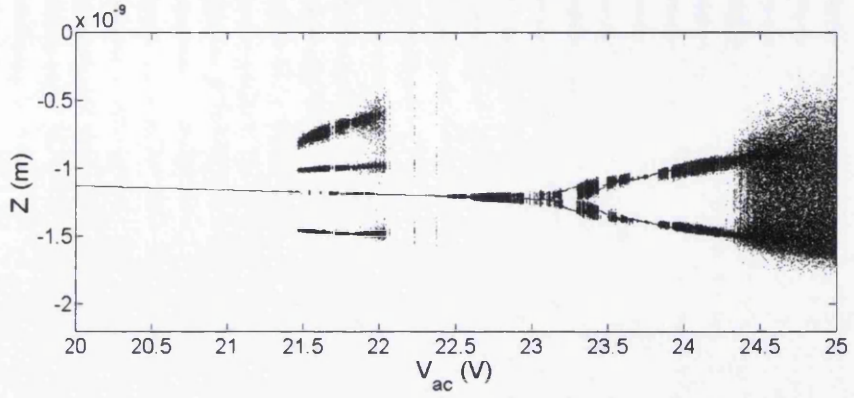

Fig. 2.5 Bifurcation diagram of displacement in Z direction of the system without surface effect under the same driving voltage V_{ac}

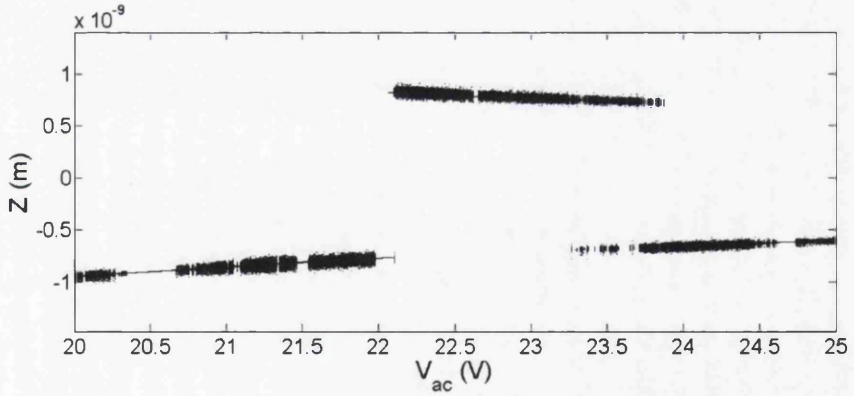

Fig. 2.6 Bifurcation diagram of displacement in Z direction of the system with surface effect under the same driving voltage V_{ac}

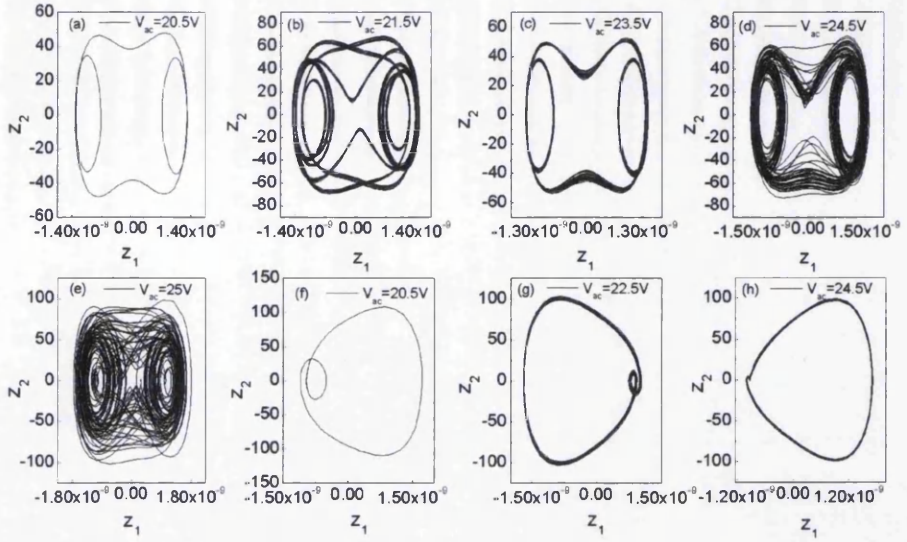

Fig. 2.7 Phase portrait (z_1 vs. z_2)of the system without surface effect in (a)-(e) and with surface effect in (f)-(h) under the different driving voltages.

a nonlinear system. It is defined by:

$$|\delta Z(t)| \approx e^{\lambda t}|\delta Z_0| \tag{2.18}$$

where the δZ_0 represents an initial infinitesimal difference of two trajectories flowing in the nonlinear systems, and the $\delta Z(t)$ is the time-dependent divergence that starts with δZ_0. If there is at least one positive Lyapunov exponent existing, the nonlinear system is determined as chaotic, and it is reasonable to take the largest one in all Lyapunov exponents of a nonlinear system to judge the system to be chaotic or not. In this section, the Lyapunov exponents of the systems Eq. 2.15 versus driving voltage increasing from 25 V to 30 V have been calculated as shown in Fig. 2.8. The plot in Fig. 2.8 (a) shows the case without considering initial surface effect, it is seen that the largest exponent λ_1 is positive in the most part of the driving voltage range, which means the system is chaotic mostly, while in Fig. 2.8 (b), where the initial surface effect taken into consideration, all the Lyapunov exponents are negative in the driving voltage of the range from 25 V to 30 V, and this is agree with Fig. 2.6 where the resonator is exhibiting in periodical states. In Figs. 2.8 (c) and (d), the transition point for changing into chaotic state from the periodical with and without considering surface effect have been studied. It is shown that the max Lyapunov exponent (MLE) becomes positive in Fig. 2.8 (c) at $V_{ac} = 24.5$ V while the transition point in Fig. 2.8 (d), where the initial surface effect considered, occurs at $V_{ac} \approx 150$ V. This to some extent explains the phenomenon that experimental results did not display whirling motions at odds with theoretical prediction

[54], in which the surface effect was not considered. In reference [53], it mentioned that with increasing driving voltage the whirling dynamics is unavoidable. In addition, it should be mentioned that all the Lyapunov exponents have been calculated with variables normalization: $z' = z/h$, $y' = y/h$, $z_1 = z'$, $z_2 = dz'/dt$, $y_1 = y'$, $y_2 = dy/dt$ and $T = \omega_0 t$

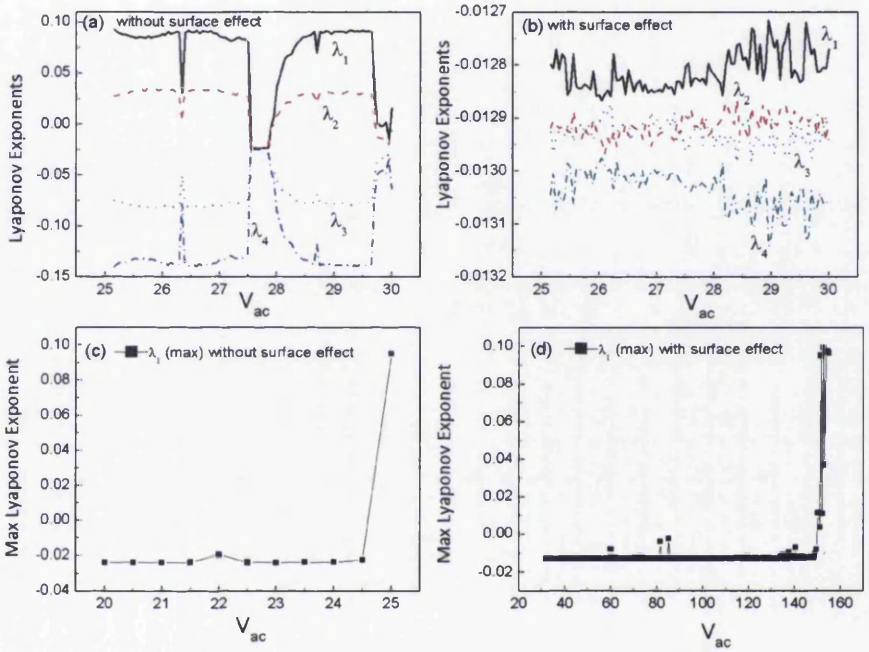

Fig. 2.8 Calculated Lyaponov exponents of the system described by Eq. 2.14 without surface effect in (a) and with surface effect in (b) driven by V_{ac} in the range of 25 V–30 V. Transition of calculated max Lyaponov exponents of the same system without surface effect to positive in (c) and with surface effect in (d).

2.3.3 Elliptical Pattern

Although the elliptic pattern of the whirling motion for device under certain driving conditions has been reported in both the previous articles [53] [37] and this work, detailed analysis of the displacement pattern of the middle point of the doubly clamped CNT resonator has not been reported so far. Herein, calculation based on mathematical model described in the previous section has been conducted to unveil the moving trajectory of the central point of the doubly clamped CNT in Y-Z plane, especially when the device is experiencing the whirling and chaotic motions. For the device under very low driving voltages, as there is not displacement in Y-direction so only one strain line in Z-direction. However as the driving

voltage increases to the level at which whirling motion occurs, the displacement pattern will display complex shapes, just like Lissajous curves formed by a pair of parametric equations.

According to calculated results, as the driving frequency varies from $1.061\omega_0$ to $1.075\omega_0$, V_{dc} and V_{ac} are fixed at 0.5 V and 1.6 V respectively, from the Lissajous pattern depicted in Fig. 2.9 (a), the oscillating frequencies in Z and Y are the same. It is shown from the results that the whirling trajectories can be categorized into two stable zones, one is centred on the 70° phase difference between Z-axis and Y-axis oscillations, and the other is centred on the +70° degree phase difference. There is no other intermediate trajectory existing. Increasing the driving voltage to 25 V V_{dc}, while varying V_{ac} from 20.5 V to 21.5 V, Lissajous patterns shown in Fig.2.9 (b) and (c) indicate that the Z-axis oscillation has different frequencies and phases, which is ascribed to multiple periodic states of the oscillations. Further increasing the driving voltage, it is calculated that the oscillator experiences chaotic motions. As a result, the displacement pattern in Y-Z plane displays a filled ellipse shown in Fig. 2.9 (d), meaning the middle point of the CNT could be any position within the outline of the ellipse.

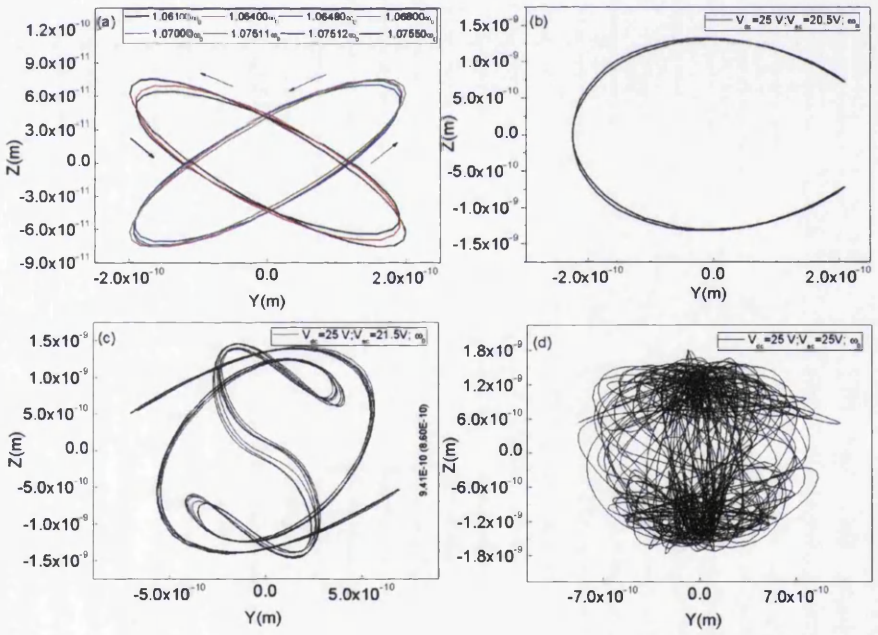

Fig. 2.9 Displacement patterns in $Y-Z$ plane formed by the middle point of the doubly clamped SWCNT resonator under different driving conditions. (a), whirling motions stabilized in two zones; (b), one Lissajous pattern formed by periodic motions in Y and Z with frequency and phase differences; (c), another Lissajous pattern for the Z and Y motions with frequency and phase differences. (d), displacement pattern in $Y-Z$ plane when the device is at chaotic state.

2.4 Application

A novel application in accelerometer based on the whirling motion of the nanotube has been proposed. While the CNT resonator is vibrating, an external acceleration applied in the Y-Z plane will change the amplitude of the vibration, which can be detected by either optical or electronic methods. Analysis is conducted to find out the vibrating amplitude change subject to external acceleration/force. In the analysis, the driving voltage $V_{dc} = 0.5$ V and $V_{ac} = 1.6$ V, at which the whirling motion appears. The driving frequency is set at $1.074\omega_0$. Here the system without surface effect is only considered, i.e. when $E_s = 0$, $\widetilde{\tau}_{xx} = 0$. The changes of the Z and Y amplitudes have been calculated as the resonator is under a Z-axis acceleration, Y-axis acceleration and Z-Y plane acceleration, respectively. The acceleration equivalences f_z and f_y are added to Eqs. 2.15, and after conducting the similar derivation procedure as described in previous section, the motion equation is:

$$\begin{aligned} \ddot{z} + \omega_0^2 z + \alpha z(z^2 + y^2) + \beta \dot{z} &= -2F_0 cos(\omega t) + f_z \\ \ddot{y} + \omega_0^2 y + \alpha y(z^2 + y^2) + \beta \dot{y} &= f_y \end{aligned} \tag{2.19}$$

where the $[f_z, f_y] = \sqrt{2/3}/\rho A \cdot [F_z, F_y]$. The peak amplitudes in Z and Y were calculated as the F_z and F_y increase in the range of [9.91 μN, 57.83μN]. The results are shown in Fig. 2.10. In Fig. 2.10 (a), when $F_y = 0$, it is seen that the peak amplitude in Z firstly decreases from 0.24 nm to 0.2 nm and then increases linearly as the acceleration force F_z increases. In Fig. 2.10 (b), when F_z=0, it is seen that the peak amplitude in Y increases over the whole force range. Furthermore, the case of $F_z \neq 0$ and $F_y \neq 0$ has been calculated. i.e. when the acceleration force is neither parallel nor perpendicular to the Y-and z-axis, and the results are shown in Fig. 2.10 (c) and 2.10 (d). As expected, the Y component of the force is proportional to the amplitude in Y-axis, and inversely proportional to the amplitude in Z-axis. Similar observation for Z component of the force is shown in the results, except when the F_y is very small, where a notch has been found at F_z=18.2 μN.

There are two types of MEMS accelerometers: piezoresistive and capacitive based accelerometers. The piezoresistive type consists of a cantilever beam with a proof mass attached to its tip and a piezoresistive patch on the beam end. When the cantilever is subjected an acceleration, the piezoresistive patch and the bulk device can turn the acceleration into an electrical signal. While, the capacitive based accelerometers sense the acceleration by changing the capacity that is formed by a movable proof mass and a fixed conductive electrode. To compare with these two types of MEMS accelerometers, the CNT resonator based accelerometer proposed in this chapter has been designed in nano-scale that makes the effective mass of the sensing beam down to $10^{-23}kg$ so that it can sense very weak force

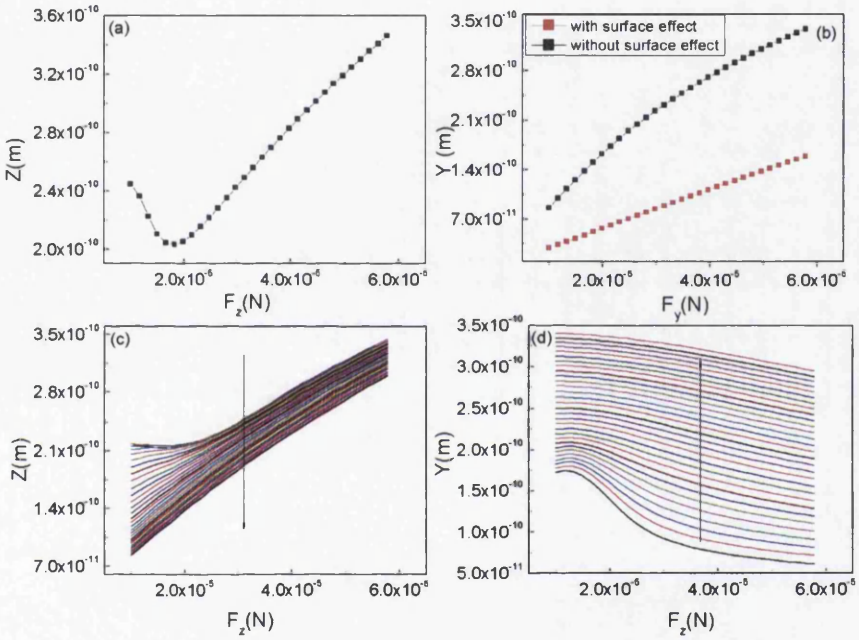

Fig. 2.10 The peak amplitude change in Z-and Y-directions as the acceleration force varies in the range of [9.91 μN, 57.83 μN]. (a), $F_y = 0$, F_z is varying. (b), $F_z = 0$, F_y is varying. (c) and (d), Both F_y and F_z are varying. The arrow in the (c) and (d) indicates the increasing direction of F_y, and the step size is approximately 1.65 μN.

($10^{-6}N$) that is induced by acceleration while in MEMS accelerometers the force can be detected is orders higher [69]. The CNT resonator based accelerometer has the merit that it can sense two directions at the same time while the traditional types are generally designed only with one single-degree of freedom. However, the CNT resonator based accelerometer has the drawbacks in packing and amplitude limit in operation. In addition, it also has a low shock limit and high operation frequency, and these drawbacks limit its practical operation.

2.5 Conclusion Remarks

It has been found from the numerical calculations that taking account of very small surface effect $E_s = 5.19$ Pa (compared with stiffness of the nanotube 5.5×10^{12} Pa), the dynamic performances of the SWCNT resonator has changed dramatically. The resonant frequency has increased to nearly twice of the value without surface effect, and the threshold voltage for the whirling motion has increased from 1.4 V to 3.5 V. Detailed analysis of the whirling motions has been conducted, and it is found that the moving trajectories of the central point of the SWCNT resonator follows Lissajous patterns. The nonlinear motions have also changed significantly due to the surface effect from the bifurcation and Lyapunov exponent analysis. The voltage needed to drive the resonator into chaotic motions has been increased from 25 V to around 150 V. The reported findings can be used to explain the previous discrepancies between experiments and theories, which will act as a more accurate guidance in designing such resonator devices. A new application in accelerometers using this resonator has been reported and the theoretical analysis is conducted to build the relation between acceleration forces and peak vibrating amplitudes.

Chapter 3

Chaotic Synchronization of Two MEMS resonators and Wireless Sensor Network

3.1 Background I

Compared with the NEMS resonators, MEMS resonators seem to be an old research topic. But they are never out of date, as the MEMS resonators can be easily fabricated, accurately modelled and widely used, and technologically, the integration of MEMS resonators with CMOS is more mature, which makes the related applications such as RF filters and sensors easy to be commercialized [3]. So far, the investigations both in linear and nonlinear working regime of the MEMS resonators have been extensively conducted, while in this chapter the discussions focus on the nonlinear part.

For an electrostatically driven MEMS resonator, the nonlinear behaviours are always related with the electrostatic force. When the electrostatic force is increased to such an extent that overcome the elastic restoring force in the beam, the pull-in instability might take place, in which the vibration of the resonator tends to approach two stable points: one is the equilibrium point where the beam is without stretching and the another one is where the beam is attached to the fixed electrode that is used for providing the driving force. The study of pull-in phenomenon in MEMS resonators has been of special interest for researchers. Laura Ruzziconi et al., in their recent work [70], have investigated the pull-in dynamics in a MEMS capacitive accelerometer (essentially a MEMS resonator). They have observed the pull-in behaviour at different excitations amplitude than anticipated, and argued that the reasons lie in the presence of disturbance. Fadi M. Alsaleem el al. have conducted a more detailed work of dynamic pull-in in MEMS resonators [71]. In their experiment, poly-silicon micro-cantilever beam, gold cantilever and clamped–clamped micro-beams, and

a capacitive accelerometer were tested, and the data of dynamic pull-in as a function of the ac frequency and amplitude had been presented. Theoretically, they have combined the shooting technique and basin-of-attraction analysis to quantitatively determine the pull-in band of MEMS resonators, and the results are believed to be useful for avoiding pull-in in practical use. By proposing a different model that has strong potential to deal with the nonlinearities in the geometric of the deformable micro-beam and in the electrostatic force, Barun Pratiher [72] has concluded that the higher order correction of electrostatic pressure increase the threshold of the occurrence of pull-in.

Apart from pull-in, the study of chaos in the MEMS resonators has also attracted much attention. Chaos is ubiquitous and intriguing in MEMS resonators and the route for chaos arising is relatively complicated. For example, the beam in resonators starts from vibrating linearly, before the chaos arrived, the dynamics of the resonator may go through various phases such as the one-periodic, multi-periodic and quasi-periodic [73]. The experimental observation of chaos in a MEMS device has been realized by Yongmei Cindy Wang et al. [28] in 1998. In their work, they investigated a bistable MEMS oscillator both theoretically and experimentally, and a strange chaotic attractor representing the chaotic behaviour in the resonator was demonstrated. Since then, lots of researchers have been trying to understand and predict the chaos in MEMS resonators. Melnikov analysis, as one approach to calculate the distance between stable and unstable manifolds of the system, has been developed, such as in [74], the authors calculated the Melnikov function of a MEMS resonator system that was driven by electrostatic force on both sides of the beam, and they derived an analytical criterion in terms of the system parameters to predict when the chaos is arising. Similar work can be found in [31], where the authors have combined Melnikov analysis and bifurcation analysis to reveal the effect of the parametric excitation amplitude on chaos arising. Except for the Melnikov analysis, Ehsan Maani Miandoab et al. have proposed another method that can give an accurate analytical solution for frequency response of resonators, and based on the solution they have developed an analytical criterion for predicting the chaos [75]. More recently, in work [73], it has presented a general formula to judge whether a MEMS resonator would perform chaos behaviour. The authors have derived the energy function of the resonator system and classified it into four cases according to the signs of some system parameters. It is proved that chaos appear only in the case when the dynamics of systems can behave bistable state and contains three equilibrium points: one unstable saddle point and two stable centre points. Other studies that focus on chaos phenomenon analysis, for example, dynamics investigation in a close-loop controlled MEMS resonators [30] and noise-induced chaos in the electrostatically actuated MEMS resonators [76] have also been conducted, all of which can be served to deep understand the chaos in MEMS resonators.

The insights of chaos in MEMS resonator have been gained to some extent, what faces to the researchers now is how to control the chaos as it is commonly believed that the chaos is undesirable, and they have been consistently arguing that the chaos will lead to the dysfunction of the devices. Many control methods have been proposed trying to control the resonators oscillating in the desired motion such as periodic state. One of the most direct methods is bifurcation analysis that can provide a visualized image of how the devices behave with respect to the system parameters, and thus by setting parameters properly the chaos can be avoided. But, if doing so, the parameters chosen might be not suitable for realizing other functions. In the sense of the limitation of this method, some other controlling methods have been explored. Kwangho Park et al. [77] have devised a feasible control strategy in their work that not only can control the resonator into periodic motion but also enhance the output energy. The control method does not vanish when the desired state is achieved while instead changing itself into periodic too, in which the output energy get enhanced. A.M. Tusset el al. [1] have designed three different control methods: State Dependent Riccati Equation (SDRE) Control, Optimal Linear Feedback Control, and Fuzzy Sliding Mode Control, to suppress the chaos occurred in a comb-drive MEMs actuator. Both the methods were effectively implemented without eliminating the nonlinearity of the considered systems, and also the robustness of the methods were proved when the systems parameters have random uncertainties. Other control methods target to different MEMS resonator such as output-feedback control [38] and time-varying stiffness strategy [31] have also been explored.

However, on the other hand, rather than avoiding and controlling the nonlinear behaviours, the explorations that take advantage of nonlinear behaviors have been very few. Although there are some works such as in [26], the authors have designed a novel RF MEMS switch based on the dynamic pull-in phenomenon which is actuated using a combined DC and AC loading, and recently in [78], the authors have proposed a mass detection mechanism based on bifurcation and bi-stability of the hysteric nonlinear response of MEMS resonator. However, the working mode of the resonators in theirs are still in the fundamental one, i.e. without touching with more nonlinear behaviours such as chaos. Therefore, an open question appears to be whether the chaos behaviour that arises commonly in MEMS resonators can be explored for applications.

In this chapter, the application for a mass sensor based on two coupled chaotic synchronized MEMS resonators is discussed. The designed sensor has two features: 1) the mass sensing relies on amplitude detection that is more direct to detect than frequency changing; 2) it is noise robust as the two employed MEMS resonators are in the same environment, and therefore the noise effect can be offset and weakened. In the following text, the model of chaotic MEMS resonator will be given firstly, followed by a brief introduction of OPCL

methodthat is used for realizing synchronization of two chaotic MEMS resonators. Numerical simulation will be conducted of the two synchronized chaotic MEMS resonators with or withoutmass sensed. A similarity measure will be used to reflect the mass sensing. In the end, thecase with considering the noise will be investigated.

3.1.1 Model of MEMS Resonators

It is taken the model studied in [1] as a paradigm for achieving synchronization between two resonators in this chapter. As shown in Fig. 3.1, it is a MEMS resonator that consists of

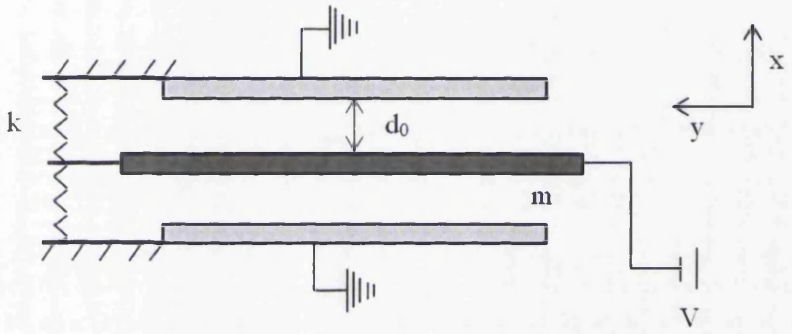

Fig. 3.1 A MEMS resonator model referenced from [1]

two fixed plates functioning as the electrodes and a movable plate between them. The initial distancebetween the middle plate with the fixed one is d_0. The movable plate is subjected to a dc (V_p) and ac ($V_i sin(\omega t)$) combined driving voltage, and it is being part of the capacitors formed with the fixed electrodes. The equation that describes the motion of the movable plate can be derived by using the Newton's second law, as:

$$m\ddot{x} = -F_k - F_c + F_e \tag{3.1}$$

where F, F_c and F_e are the restoring force, damping force and the electrostatic force between plates, respectively. The restoring force F_k can be expressed as:

$$F_k = k_1 x + k_3 x^3 \tag{3.2}$$

where k is the linear stiffness and k_3 is the nonlinear stiffness. The damping force F_c is assumed to be linearly related with the velocity of the movable plate, which is given by: $F_c = c\dot{x}$ where the c is damping ratio. The electrostatic force F_e can be calculated from the total electric energy stored, represented by W_e, in the two capacitors formed in the device.

The W_e is given by [1]:

$$W_e = \frac{\varepsilon_0}{2} V^2 A \left(\frac{1}{d_0 - x} \right) + \frac{\varepsilon_0}{2} V^2 A \left(\frac{1}{d_0 + x} \right) \tag{3.3}$$

where $V = (V_p + V_i sin(\omega t))$, ε_0 is the permittivity of vacuum and the A is the plate area. The F_e can then be calculated by:

$$F_e = \frac{\partial W_e}{\partial x} = 2\varepsilon_0 d_0 A V^2 \frac{x}{(d_0^2 - x^2)^2} \tag{3.4}$$

By combining all the specific expressions of the forces related to the motion Eq. 3.1, it is straightforward to write the motion equation of the device, as:

$$m\ddot{x} + k_1 x + k_3 x^3 + c\dot{x} = 2\varepsilon_0 d_0 A V^2 \frac{x}{(d_0^2 - x^2)^2} \tag{3.5}$$

Due to the nonlinearities brought by the F_e and $k_3 x^3$, the Eq. 3.5 can exhibit chaotic behaviour given certain parameters settings.

3.1.2 Open-Loop–Closed-Loop Method

Open-loop–closed-loop (OPCL) coupling method was first proposed by Ioan Grosu et al. [2]. It is a coupling scheme that can be used to synchronize two chaotic systems either identical or parameter-mismatched. According to the OPCL method, one of the two systems is called driver, which can be expressed in a general form: $\dot{y} = F(y) + \Delta F(y), y \in R^n$, where F represents a general nonlinear function and $\Delta F(y)$ contains the parameter-mismatched terms. Another system is called response system, which has the form: $\dot{x} = F(x), x \in R^n$, having the same function F. In order to synchronize these two parameter-mismatched systems, the authors of [2] have designed a coupling scheme added to the response system, and then a driven system can be obtained, which is:

$$\dot{x} = F(x) + D(x, \alpha y) \tag{3.6}$$

where α is a constant which can be used to modulate the goal dynamics. For example: $\alpha = 1$ is for complete synchronization (CS), and $\alpha = -1$ is for anti-synchronization (AS). The $D(x, \alpha y)$, which actually plays the role to "connect" the driver and response system, is given by:

$$D(x, \alpha y) = \alpha y - F(\alpha y) + [H - JF(\alpha y)](x - \alpha y) \tag{3.7}$$

In the coupling term D, the H is an arbitrary constant Hurwitz matrix whose eigenvalues all have negative real parts and $J = \partial/\partial(\alpha y)$ is Jacobian. Based on this method, the authors have successfully achieved AS and CS in three parameter-mismatched nonlinear systems, i.e. Lorenz system, Rössler system and Sprott system. In addition, they have also proved this method can be realized by electronic circuits, as shown in Fig. 3.2. The OPCL method will

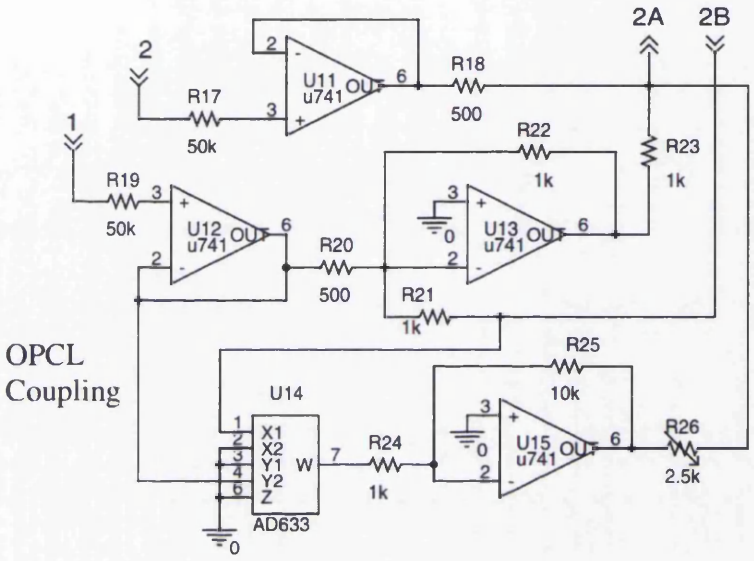

Fig. 3.2 Realizing OPCL method by circuit for Sprott system [2]

be employed in the next for realizing two chaotic MEMS resonator systems.

3.2 Synchronizing Two MEMS Resonators

Based on the MEMS resonator introduced in the first section, a novel mass sensor has been designed in this section, as shown schematically in Fig. 3.3, in which two identical MEMS resonators have been employed, and the two resonators, w and u, are functioning as the reference system and sensing system, respectively. In the practical operation, the u and w will be first of all set into CS which can be achieved by OPCL method. If there is any tiny mass changes on the sensing system u, the two systems will be de-synchronized, through which the sensing function is realized, and then a quantitative similarity measure will be used to reflect the level of the de-synchronization. Mathematically, the motion equation of each resonator can be given according to the first section, which is:

$$m\ddot{x} + k_1 x + k_3 x^3 + c\dot{x} = 2\varepsilon_0 d_0 A V^2 \frac{x}{(d_0^2 - x^2)^2} \tag{3.8}$$

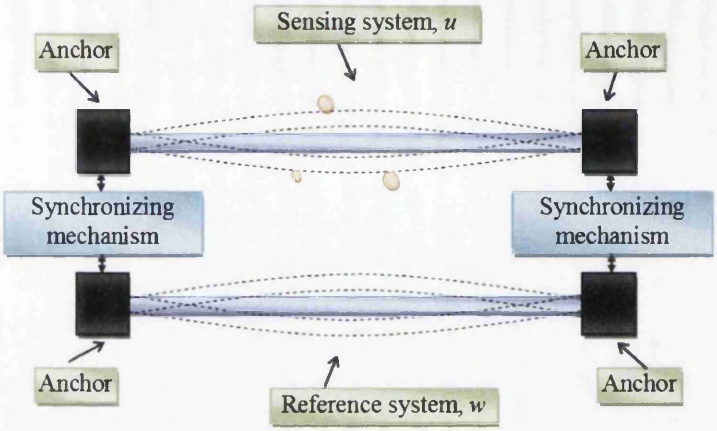

Fig. 3.3 Cartoon schematic of the two synchronized resonators for sensing application.

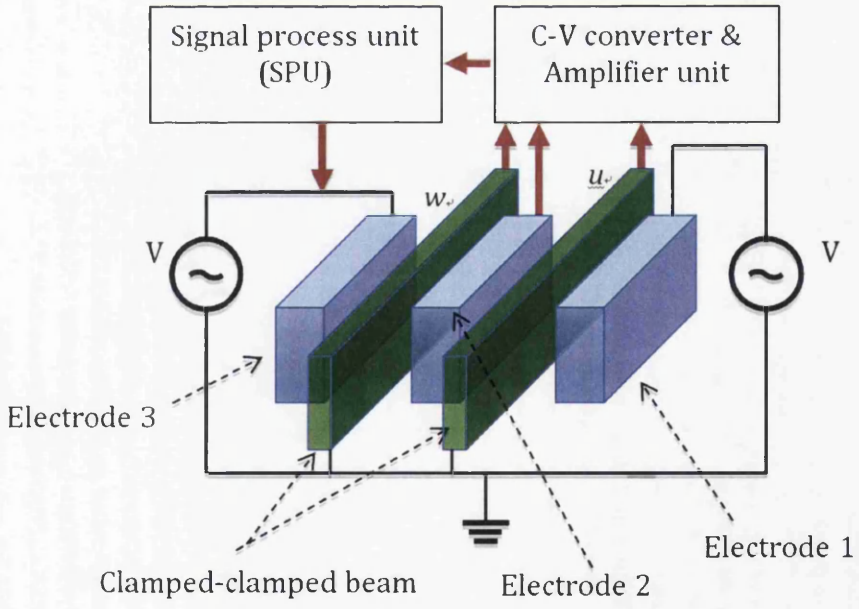

Fig. 3.4 Design of a sensor system using two electrostatically driven doubly clamped resonators.

where m is the effective mass of the resonator, k_1 is the constant that control the stiffness, k_3 is the coefficient of Duffing term that controls the amount of nonlinearity in the restoring force and c is the damping ratio. On the right side of the Eq. 3.8, it is the term that represents the diving force, in which the d_0 is the initial distance between the fixed and movable plates, A is the overlap area between two parallel plates, V is the driving voltage which has two parts as: $V=V_p+V_i sin(\omega t)$, where the V_p and the V_i are dc and ac voltage, respectively, and ω is the diving frequency. x is the displacement of the MEMS resonator.

In order to conduct the numerical simulation easily, the motion Eq. 3.8 has been normalized by introducing: $T = \omega_0 t$ and $u = x/x_0$, and then the new is given by:

$$\begin{aligned} \dot{u_1} &= u_2 \\ \dot{u_2} &= -\alpha_1 u_1 - \alpha_3 u_1^3 - b u_2 + \beta V^2 \frac{u_1}{(d^2 - u_1^2)^2} \end{aligned} \tag{3.9}$$

where the relations $u_1 = u$, $\dot{u_1} = u_2$ and the coefficients defined by the following equations:

$$\begin{aligned} b &= \frac{c}{m\omega_0}, \alpha_1 = \frac{k_1}{m\omega_0^2}, \alpha_3 = \frac{k_3 x_0^2}{m\omega_0^2} \\ \beta &= \frac{2\varepsilon_0 d_0 A}{m\omega_0^2 x^4}, \nu = \frac{\omega}{\omega_0^2}, d = \frac{d_0}{x_0} \end{aligned} \tag{3.10}$$

have been used. The reference system w can be modelled identically with the sensing system u as:

$$\begin{aligned} \dot{w_1} &= w_2 \\ \dot{w_2} &= -\alpha_1 w_1 - \alpha_3 w_1^3 - b w_2 + \beta V^2 \frac{w_1}{(d^2 - w_1^2)^2} \end{aligned} \tag{3.11}$$

The u and w system are taken as the driver and reference system, respectively, according to the OPCL method. Specifically, the w is driven into a goal dynamics: $g(t) = \alpha u(t)$, where α is the modulate constant, and it is taken to be 1 in the following simulation as CS is expected to achieve here. The driven system can be written as:

$$\dot{w} = F(w) + D(w, \alpha u) \tag{3.12}$$

where $D(w, \alpha u)$ is the coupling term, and it is formulated according to Eq. 3.7, which actually can be adopted in straight way only by changing the variables: $x \rightarrow w$ and $y \rightarrow u$.

To make clear of the OPCL coupling term, the Jacobin J of Eq. 3.9 is firstly calculated:

$$J = \begin{bmatrix} \partial/\partial u_1 & \partial/\partial u_2 \\ \partial/\partial u_1 & \partial/\partial u_2 \end{bmatrix} = \begin{bmatrix} 0 & 1 \\ -\alpha_1 - 3\alpha_3 u_1^2 + \frac{V^2\beta}{(d^2-u_1^2)^2} - \frac{4u_1V^2\beta}{(-d^2+u_1^2)^3} & -0.5 \end{bmatrix} \tag{3.13}$$

The matrix J can be used to select the elements of H. As mentioned before, the H is a Hurwitz matrix and it needs to be satisfied the so-called Routh-Hurwitz (RH) condition that all its eigenvalues must have negative real parts. The authors in [2] have proposed a method to chose the elements of H. They claimed that the element H_{ij} can be chosen as the same constant if J_{ij} is a constant, and the H_{ij} can be set to be variable, for example p, if J_{ij} is not a constant. According to this method, $H = [0, 1; p, -0.5]^T$ can be firstly derived. However, this H is not sufficient, and some elements have to be changed to "fix" the H for becoming a Hurwitz matrix. Here, the H finally is selected as $H = [-15, 1; -5, -0.5]^T$, with 0 and p has been replaced by -15 and -5, respectively, Now after the J and H have been determined, the driven system Eq. 3.12 can be written explicitly, as:

$$\begin{aligned} \dot{w}_1 &= w_2 + 15au_1 - 15w_1 \\ \dot{w}_2 &= -\alpha_1 w_1 - \alpha_3 w_1^3 - bw_2 + \beta V^2 \frac{w_1}{(d^2 - w_1^2)^2} \\ &\quad - a\alpha_3 u_1^3 + a^3\alpha_3 u_1^3 + au_1V^2\beta/(d^2-u_1^2)^2 - au_1V^2\beta/(d^2-a^2u_1^2)^2 + (-au_1 + w_1) \\ &\quad \times (-5 + \alpha_1 + 3\alpha_3 u_1 - V^2\beta/(d^2-u_1^2)^2 + 4u_1^2V^2\beta/(-d^2+u_1^2)^3) \end{aligned} \tag{3.14}$$

When the system parameters are properly set, the u and w system can exhibit chaotic behaviour which can be verified by calculating the Lyapunov exponents. Here, the parameters have been taken as follows: $\alpha_1 = 1$, $\alpha_3 = 0.4$, $\beta = 69141.6$, $b = 0.5$, $d = 25$, $v = 6.28$, $V_p = 2$ V and $V_i = 10$ V [1].

The numerical calculation of the Eqs. 3.9 and 3.14 have been calculated firstly, as shown in Fig. 3.5. It is seen that in Fig. 3.5 (a) the time series of u_2 and w_2 have been realized to CS, which also can be proved by plotting u_2 versus w_2 and the error dynamics $e = u_2 - w_2$ versus t, shown in Fig. 3.5 (b) and Fig. 3.5 (c), respectively. Moreover, the chaotic attractors of the two chaotic systems have been plotted in Fig. 3.6, where the two strange attractors present identically.

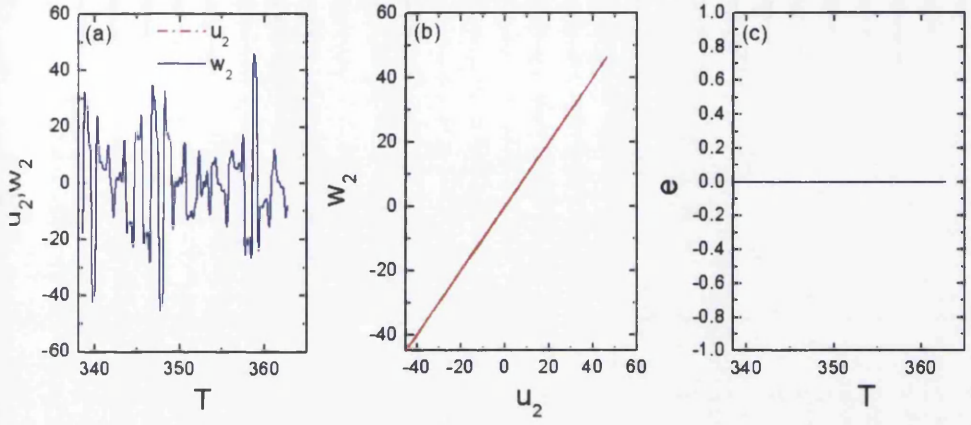

Fig. 3.5Results of synchronized two MEMS resonators. (a) The time series for synchronized u_2 and v_2. (b) The plot of u_2 vs. w_2. (c) The error dynamics.

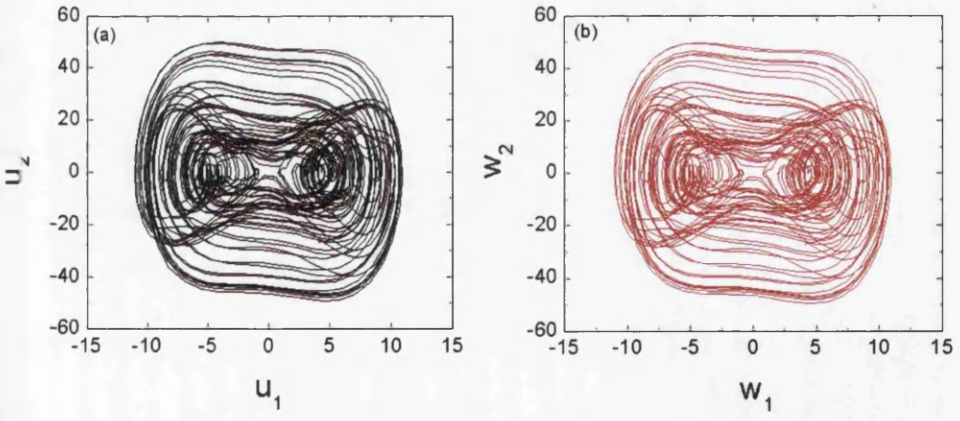

Fig. 3.6 Chaotic attractors of the two MEMS resonators.

3.3 Synchronized System with Application in Mass Sensor

With the purpose for realizing a practical system, the Eq. 3.14 needs to be re-arranged as:

$$\begin{aligned}
\dot{w}_1 &= w_2 + 15au_1 - 15w_1 \\
\dot{w}_2 &= -\alpha_1 w_1 - \alpha_3 w_1^3 - bw_2 + \beta V^2 \frac{w_1}{(d^2 - w_1^2)^2} \\
&\quad (-u_1 + w_1)(-5 + \alpha_1 + 3\alpha_3 u_1 - V^2\beta/(d^2 - u_1^2)^2 + 4u_1^2 V^2 \beta/(-d^2 + u_1^2)^3)
\end{aligned} \tag{3.15}$$

In the Eq. 3.15, it is obviously to see that $u_1 - w_1$ can be obtained from detecting displacements of the two MEMS resonators. The term $(-5 + \alpha_1 + 3\alpha_3 u_1 - V^2\beta/(d^2 - u_1^2)^2 + 4u_1^2 V^2\beta/(-d^2 + u_1^2)^3)$ is the dynamical coefficient related to u_1. According to disassemble of Eq. 3.15, it is reasonable to arrive at two doubly clamped resonating beams sharing one central electrode like what is depicted in Fig. 3.4. First of all, the two resonators are driven into the chaotic state by applying a same excessive voltage V. The central electrode 2 is used to extract the capacitances (C_1 and C_2) between this electrode and resonators, which represent the displacements (u_1, w_1) of these two resonators, respectively. Further, the extracted capacitances can be converted and amplified subsequently by a C-V converter and amplifier unit, and the converted signal, as an input, is processed by the signal processing unit (SPU), in which the algorithms of Eq. 3.15 is carried out. Finally, the output of the SPU is fed back to w system, completing the closed loop of the OPCL.

After the synchronization of the two chaotic resonator u and w and a feasible design suggestion have been discussed. The next step is to validate the sensing mechanism by manually changing the mass of u system. In the following calculation the "sensed" mass changes on u is represented by changing the m, where m is the original effective mass of the u. Accompanying with the mass change, the coefficients α_1, α_3, b and β in the Eq. 3.9 will be varied accordingly, here a tuning parameter ε has been inserted in the Eq. 3.9 to reflect the change of mass. Taking into account this tuning parameter, the Eq. 3.9 becomes:

$$\begin{aligned}
\dot{u_1} &= u_2 \\
\dot{u_2} &= -\frac{1}{\varepsilon}\alpha_1 u_1 - \frac{1}{\varepsilon}\alpha_3 u_1^3 - \frac{1}{\varepsilon} b u_2 + \frac{1}{\varepsilon}\beta V^2 \frac{u_1}{(d^2 - u_1^2)^2}
\end{aligned} \tag{3.16}$$

The MEMS resonator w and OPCL operators remained constant as in references, re-calculating the coupled system to find out if two MEMS resonators $\dot{u} = F(u)$ and $\dot{w} = F(w)$ are still synchronized.

In order to check whether the sensing system u is still in chaotic state after the m is increased, the max lyapunov exponent (MLE) of system u has been calculated in Fig. 3.7,

and it is seen that the MLE is positive with varying m from $1m$ to $1.07m$. Therefore, this particular mass sensor's working range can be set in the range of $[0 \quad 0.07m]$.

The visualized degree of the de-synchronization due to the mass changes on u is shown in Fig. 3.8. As the mass change increased from 0.01 m to 0.07 m, it is seen obviously that the original synchronized time trajectory patterns starts to de-synchronization, and the heavier mass attached the more de-synchronization occurs, but will not lead to totally de-synchronized. For practical applications, it is required to have a quantitative measure to reflect the mass attached to the sensor, as it is very difficult to quantify the trajectory graphs from Fig. 3.8. The similarity measured (unitless) of these two synchronized MEMS resonators can be introduced, which is defined by:

$$\delta = \frac{\langle [u_2 - \alpha w_2(t-\tau)]^2 \rangle}{[\langle u_2(t)^2 \rangle \langle w_2(t)^2 \rangle]^{\frac{1}{2}}} \tag{3.17}$$

where τ is the time delay, and $\delta = 0$ when the two systems u and w are reached CS, i.e when there is no mass attached on the sensing system u. By calculating Eq. 3.17 based on parameters in the above sections, δ increases up to $3.25\times\ 10^{-5}$ as the attached mass increases from 0 to 0.07 m (Fig. 3.9).

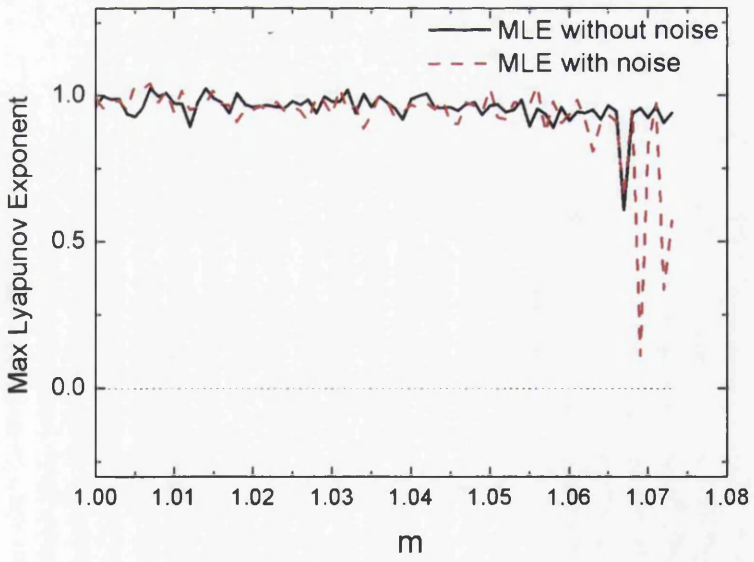

Fig. 3.7 Max Lyapunov exponents for the sensing system u, with the mass being changed from m to $1.07m$. The bounded noise has been analysed, and the MLE for the system with noise is also plotted.

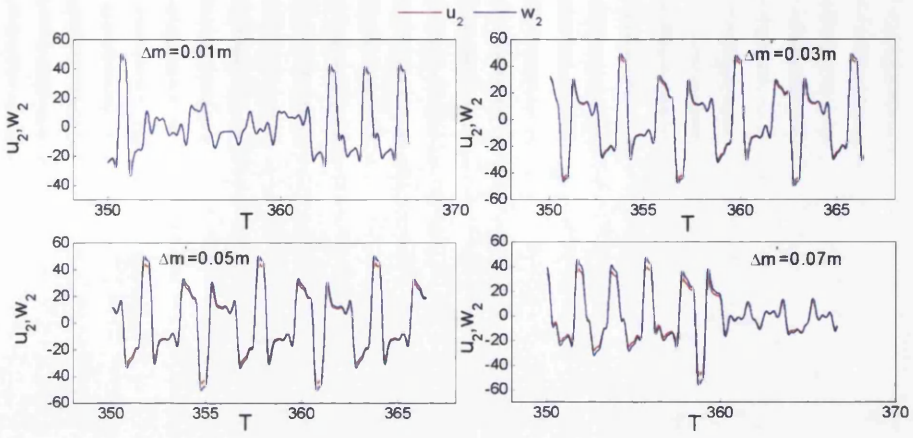

Fig. 3.8 Trajectories of the synchronized systems when the mass of the sensing system changes from m to $1.07m$. Time series of u_2 and w_2 for mass changes of $0.01m$, $0.03m$, $0.05m$ and $0.07m$ are plotted.

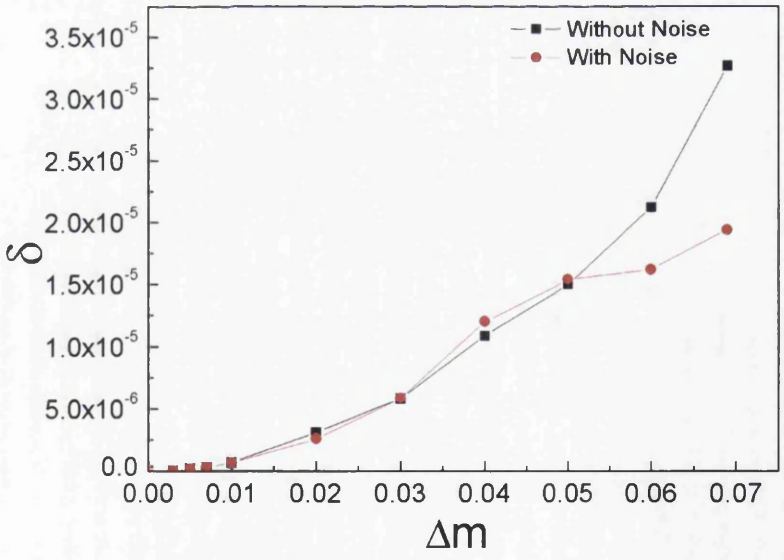

Fig. 3.9 Similarity measure δ used for quantitatively characterizing the sensitivity of the system has been plotted for the situations of both with noise and without noise. Added mass varies from $0.01m$ to $0.07m$.

3.4 Noise Consideration

In the practical operation of the sensors, the noise is unavoidable, and sometimes it brings serious consequence that may lead the device completely useless. In this section, the bounded noise is considered. Bounded noise is a slowly varying random process, which has constant amplitude and random frequencies and phases, and it has been widely studied in the real systems [76][79] [80]. The equation for describing this type of noise is:

$$f(t) = \sigma cos(\Omega_2 t + \Phi), \quad \Phi = \delta B(t) + \Gamma \tag{3.18}$$

where the σ and Ω_2 represent the amplitude and frequency of the random excitation, respectively. In the sub-second equation in Eq. 3.18, the $B(t)$ and Γ are a standard Wiener process and a random variable that distributed uniformly in [0,2π]. The σ, Ω_2 and δ are required to be positive. When the bounded noise is considered, the equation of the sensing system u becomes:

$$\begin{aligned} \dot{u_1} &= u_2 \\ \dot{u_2} &= -\frac{1}{\varepsilon}\alpha_1 u_1 - \frac{1}{\varepsilon}\alpha_3 u_1^3 - \frac{1}{\varepsilon}b u_2 + \frac{1}{\varepsilon}\beta V^2 \frac{u_1}{(d^2 - u_1^2)^2} + f(T) \end{aligned} \tag{3.19}$$

where $f(T)$ is the random process in Eq. 3.18 with $T = \omega_0 t$. Eq. 3.18 can be rewritten as

$$f(T) = v cos(\psi(T)), \quad \dot{\psi}(T) = \omega_2 + \kappa\xi(T), \quad \xi(T) = \dot{B}(T) \tag{3.20}$$

where κ is the noise intensity and $v = \sigma/m\omega_0^2$. The Wiener process B is taken as the Gaussian white noise with power spectrum. The formal derivative $\xi(T)$ of $B(T)$ is defined by:

$$\xi(T) = \sqrt{\frac{4\omega_2}{N}} \sum_{k=1}^{N} cos\left[\frac{\omega_2}{N}(2k-1)T + \varphi_k\right] \tag{3.21}$$

where N is a very large integer number and φ_k is independent and uniformly distributed in (0,2π). Meanwhile, the reference system w is also exposed by the noise $f(T)$, and the similar equation as Eq. 3.19 can also be used to describe w. By using the same parameters with above section and taking $N = 100000$, the MLE of the system with the bounded noise considered has been calculated, which is shown in Fig. 3.7. It is seen that the MLE has an obvious non-regular change compared with the one without noise but it still keep as positive, which means the MEMS resonator is still in chaotic state even when the noise is considered. The reliability of the OPCL method has been re-verified in Fig. 3.10 when the bounded noise is involved. It is seen the CS can still be realized. The bifurcation diagram has been

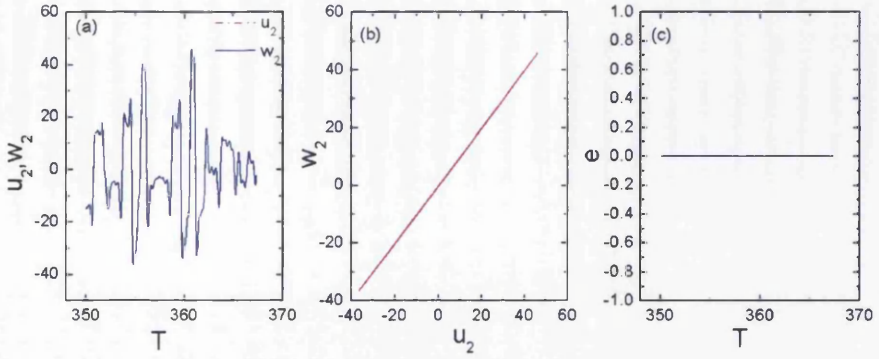

Fig. 3.10 Results of synchronized two MEMS resonator systems in the presence of the bounded noise. (a) The time series for synchronized u_2 and w_2. (b) The plot of u_2 vs.w_2. (c) The error signal.

calculated in Fig. 3.11, where the effect of the bounded noise can be seen clearly. The similar

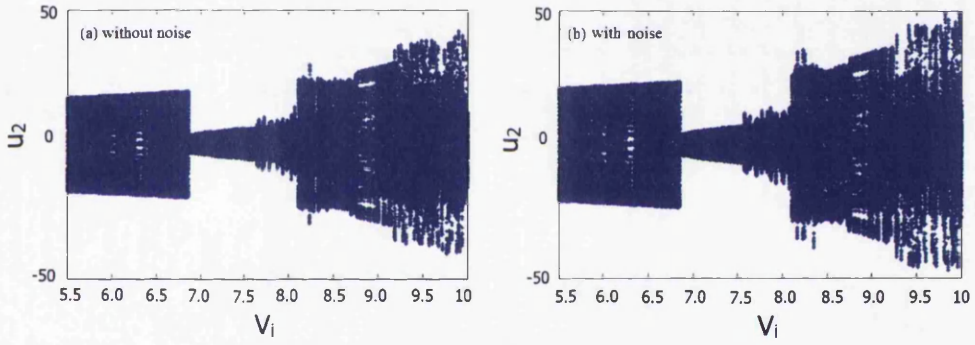

Fig. 3.11 Bifurcation diagrams of u and w systems subjected to the bounded noise ($k = 0.1, v = 0.1$) in (b), and without the noise in (a), respectively. The unit of V_i is volt.

analysis of the performance of the mass sensor subjected bounded noise has been conducted in Fig. 3.12, which proves the method's effectivity even under the consideration of noise. Lastly, the similar measure δ has been re-calculated under the bounded noise as shown in Fig. 3.9, which further proves the OPCL synchronization method is still valid to detect mass changing.

Compared with other mass sensors which normally employ only one single resonator, the mass sensor proposed in this chapter has the advantage in the wide working range that can work in nonlinear regime (chaotic state). Furthermore, as the two coupled MEMS resonators are synchronized together and put in the same working environment so that it can get rid of the noise effect, which plays an unwanted role in sensors. However, it has drawbacks in terms of fabrication because of its complicated structures. Overall, this mass sensor provides

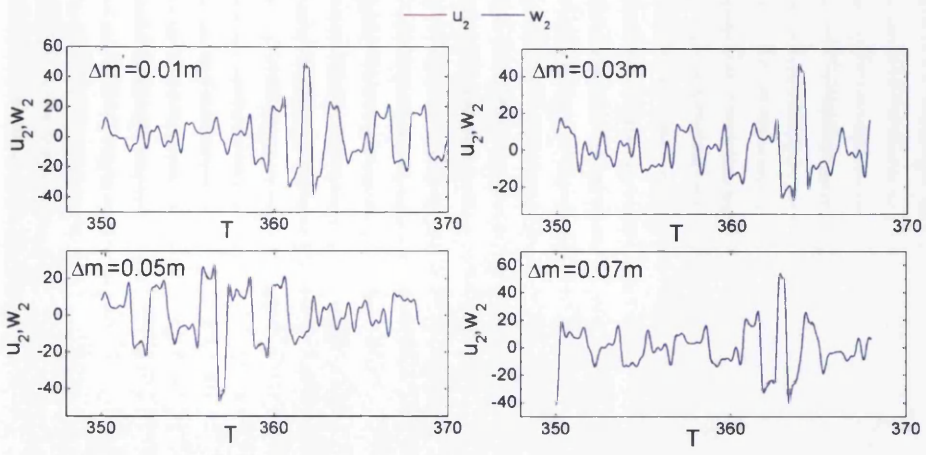

Fig. 3.12 Trajectories of the synchronized systems when the mass of the sensing system changes from m to $1.07m$ with bounded noise. Time series of u_2 and w_2 for mass changes of $0.01m$, $0.03m$, $0.05m$, and $0.07m$ are plotted.

a new idea for mass sensing when the noise effect is concerned and wide working range needed.

3.5 Background II

In the first part of this chapter, it has been discussing about the chaotic synchronization between only two coupled MEMS resonator systems, and a mass sensor that employs the OPCL method has been realized. In this part, it is trying to explore the use of CS in wireless sensor network (WSN) network that includes more sensor systems. Even though these sensor system may be not the MEMS resonators, it still can be seen as a further work that tries to apply the theory of nonlinear dynamics into sensing field.

WSN has attracted much attention from both academic and industrial sectors as it has been ubiquitously used in surveillance [81], industrial process control [82], structural health monitoring [83], and even in healthcare [84]. A WSN is usually constructed by many sensors that detect physical and environmental conditions based on various transduction technologies, and a base station that receives and processes data from all of those sensors. Though the WSN technology is a well-established area, there are many challenges such as energy sources for sensors, production of miniature sensors, and communication between sensors and the base station. Particularly in terms of data transferring in a WSN, quite often a more secure communication is required. Previously modulating data by a chaotic signal was regarded as a more secure approach [85]. A lot of efforts have been devoted in this development in the past. For example, two chaotic coding and de-coding methods based on artificial neural networks

were reported in [86]. Chaotic synchronization was used in discrete-time systems connected by bandlimited channels [87]. The bit error rate performance for differential chaos shift keying chaotic communication was evaluated by using the non-central F distribution of the decision variable in the reference [88]. In order to establish a communication between two chaotic signals from both the base and one sensor node, chaotic synchronization is essential and has to be carefully researched. Here, the OPCL coupling method will be re-employed for realizing the chaotic synchronization between the time-delay Lorenz systems that are used for encrypting the sensor networks, and it is worth to mention that the model of the sensor is not fixed.

3.6 Model Construction

A secure communication scheme that takes advantage of the chaotic synchronization among wireless sensors network has been postulated in this section. As shown in Fig. 3.13, there

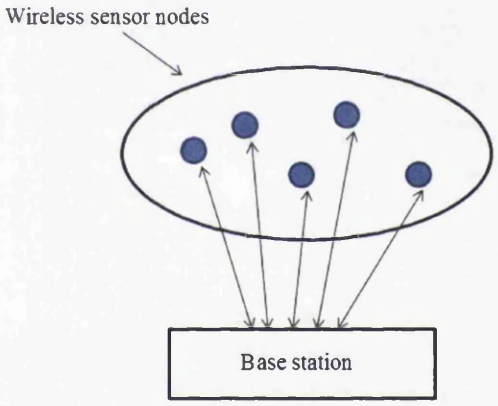

Fig. 3.13 Schematic sketch of a wireless sensor network, blue dots represent sensor nodes, and bidirectional arrows stand for the communication between sensor nodes and the base station.

are a base station acting as the commander and some sensor nodes are distributed around to represent the practical network. Supposing the information transmitted from a single node is encrypted by a chaotic signal, the communication security will then be enhanced. But the problem is the receiver, commander in the base station, should have the ability to decode it, and the only way to decode the chaotic-coded signal is to use CS, which acts the role of a "key" for decoding the transmitted information.

In this model, a time-delayed dynamical system is used to generate the chaotic signal for encryption. The commander and sensors are equipped the same but with parameter-

mismatched time-delayed dynamical systems, and then a coupling method that based on the modified OPCL will be designed to realize the synchronization between them. Due to the high sensitivity of the chaotic systems, it is challenging to synchronize two chaotic systems with different initial values and mismatched parameters, especially for the time-delayed systems that has the intrinsic nature for generating high-dimensional chaotic signal. Specifically, the time-delayed dynamical system employed in this model is given by:

$$\begin{aligned} \dot{x}_1 &= -\sigma x_1 + \sigma x_2 \\ \dot{x}_2 &= r x_1 - x_2 - x_1(t-\tau)\cdot x_3(t-\tau) \\ \dot{x}_3 &= -b x_3 + x_1(t-\tau)\cdot x_2(t-\tau) \end{aligned} \tag{3.22}$$

where x_i, $i = 1,2,3$ are the state variables, and $x_i(t-\tau)$, $i = 1,2,3$ are the time-delayed terms with τ is the delay time. σ, r, and b are the system parameters. Under a proper parameters setting, the Eq. 3.22 will perform chaotic behaviour. It is worth to note that the synchronization between the commander and all the sensor nodes can not be realized simultaneously, while a selective matrix will be introduced, as shown in Fig. 3.14, functioning to select the one expected to be synchronized. The selective matrix will be given explicitly in the following section. The time-delayed dynamical system that is used to generate chaotic

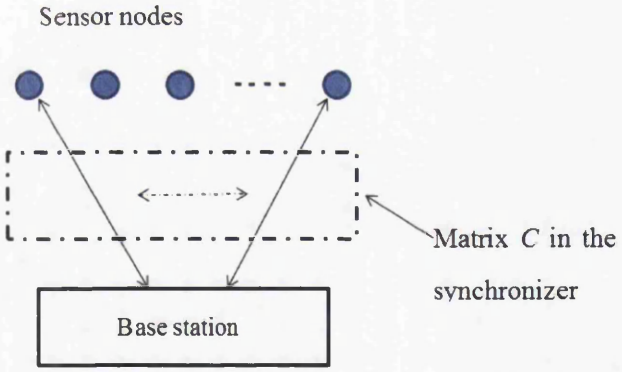

Fig. 3.14 Synchronization between the base and individual sensor node can be achieved by using an identification matrix C , which essentially scans the synchronizer from the first sensor node to number N node.

signal for the sensor nodes are taken the same form as the Eq. 3.22 but with the parameters mismatched as the each single practical sensor systems can not be identically realized. It can

be written as:

$$\begin{aligned}\dot{y}_{i1} &= (\sigma+\Delta\sigma_i)\cdot(y_{i2}-y_{i1})\\ \dot{y}_{i2} &= (r+\Delta r_i)y_{i1}-y_{i2}-y_{i1}(t-\tau)\cdot y_{i3}(t-\tau)\\ \dot{y}_{i3} &= -(b+\Delta b_i)y_{i3}+y_{i1}(t-\tau)\cdot y_{i2}(t-\tau)\end{aligned} \tag{3.23}$$

where y_{i1}, y_{i2} and y_{i3} are the states variables of sensor node i ($i=1,2,\ldots$), and the $\Delta\sigma$, Δr and Δb are mismatched parameters. In order to achieve CS between the commander and sensor node i, once again the OPCL based coupling method is used, but it needs to be modified as in this model the CS is expected between one to many rather than one to one scheme, and the nonlinear dynamical systems employed here are time-delayed. A new coupling method $D(x,ay_i)$ has been proposed, which is expressed in the following form:

$$D(x,ay_i)=C\cdot(ay_i-F(ay_i))+A[(H-JF(ay_i))]\begin{bmatrix}x_1-ay_{i1}\\ x_{1\tau}-ay_{i1\tau}\\ x_2-ay_{i2}\\ x_{2\tau}-ay_{i2\tau}\\ x_3-ay_{i3}\\ x_{i\tau}-ay_{i3\tau}\end{bmatrix} \tag{3.24}$$

, and this coupling term will be intentionally added to the right side of the commander system Eq. 3.22, which functions to connect the commander system and the sensor i. In the Eq. 3.24, a is a constant which can be used to modulate the synchronization realization such as $a=1$ is set for CS. The H is an arbitrary constant Hurwitz matrix ($M\times M$) whose eigenvalues all have negative real parts and J is the Jacobian matrix, which is defined by [89]:

$$J=\begin{bmatrix}\frac{\partial}{\partial(ay_{i1})} & 0 & \frac{\partial}{\partial(ay_{i2})} & 0 & \frac{\partial}{\partial(ay_{i3})} & 0\\ 0 & \frac{\partial}{\partial(ay_{i1\tau})} & 0 & \frac{\partial}{\partial(ay_{i1\tau})} & 0 & \frac{\partial}{\partial(ay_{i1\tau})}\\ \frac{\partial}{\partial(ay_{i1})} & 0 & \frac{\partial}{\partial(ay_{i2})} & 0 & \frac{\partial}{\partial(ay_{i3})} & 0\\ 0 & \frac{\partial}{\partial(ay_{i1\tau})} & 0 & \frac{\partial}{\partial(ay_{i1\tau})} & 0 & \frac{\partial}{\partial(ay_{i1\tau})}\\ \frac{\partial}{\partial(ay_{i1})} & 0 & \frac{\partial}{\partial(ay_{i2})} & 0 & \frac{\partial}{\partial(ay_{i3})} & 0\\ 0 & \frac{\partial}{\partial(ay_{i1\tau})} & 0 & \frac{\partial}{\partial(ay_{i1\tau})} & 0 & \frac{\partial}{\partial(ay_{i1\tau})}\end{bmatrix} \tag{3.25}$$

It should be noted that for the time-delayed system when calculating the Jacobian matrix, the variables that contain time-delayed term can be treated equally as an independent variable. So for the sensor i it is treated to have six variables: y_{i1}, y_{i2}, y_{i3}, $y_{i1\tau}$, $y_{i2\tau}$, $y_{i3\tau}$. The matrix A

in the coupling term is taken as:

$$A = \begin{bmatrix} 1 & 1 & 0 & 0 & 0 & 0 \\ 0 & 0 & 1 & 1 & 0 & 0 \\ 0 & 0 & 0 & 0 & 1 & 1 \end{bmatrix} \tag{3.26}$$

The matrix C is a selective matrix which has n_0 row and N column, with n_0 is the dimension of the dynamical system and N is the number of the sensor nodes, and it behaves like a single pole, multi-row switch that will change its element depending on which sensor is expected to be synchronized with the commander. For example, if the sensor node i is expected, the element of the C will be set as $C_{n,n_0 \cdot i - n_0 + n} = 1$ and all other elements are set to be 0, where $n = 1, 2, \ldots$

3.7 Case Study

If sensor $i = 2$ is targeted to realize CS with the base station (commander), then the matrix C should be set as:

$$C = \begin{bmatrix} 0 & 0 & 0 & 1 & 0 & 0 & \ldots \\ 0 & 0 & 0 & 0 & 1 & 0 & \ldots \\ 0 & 0 & 0 & 0 & 0 & 1 & \ldots \end{bmatrix} \tag{3.27}$$

, and $a = 1$ for CS. The H must satisfy the Routh-Hurwitz (RH) condition that ensures eigenvalues of H all with negative real parts, which has been discussed in the first part of this chapter. In this case, the H is taken as:

$$A = \begin{bmatrix} -2.7 & 0 & 0 & 0 & 0 & 0 \\ 0 & -3.1 & 0 & 0 & 0 & 0 \\ 0 & 0 & -10 & 0 & 0 & 0 \\ 0 & 0 & 0 & 0 & 0 & -1 \\ 0 & 0 & 0 & 0 & -7.5 & 0 \\ 0 & 0 & 0 & 2.8 & 0 & -0.01 \end{bmatrix} \tag{3.28}$$

, and it can be used for other sensors as well. The coupling $D(x, ay_i)$ can be calculated in a straightforward way based on the sensor dynamical system of Eq. 3.23. And after the $D(x, ay_i)$ is calculated the commander system will be driven by the OPCL synchronizer into

the following form:

$$\begin{aligned}
\dot{x}_1 =& -\sigma x_1 + \sigma x_2 + a\Delta\sigma(y_{22} - y_{21})(-2.7 + \sigma)(x_1 - ay_{21}) - \sigma(x_2 - ay_{22}) - 3.1(x_{1\tau} - ay_{21\tau}) \\
\dot{x}_2 =& rx_1 - x_2 - x_1x_3 + a\Delta r y_1 + ay_{23\tau}(x_{1\tau} - ay_{21\tau}) + (ay_{21\tau} - 1)(x_{3\tau} - ay_{23\tau}) - r(x_1 - ay_{21}) \\
& - 9(x_2 - ay_{22}) \\
\dot{x}_3 =& -bx_3 + x_1x_2 + a\Delta b y_{23} - ay_{22\tau}(x_{1\tau} - ay_{21\tau}) + (2.8 - ay_{22\tau}) + (b - 7.5)(x_3 - ay_{23}) \\
& - 0.01(x_{3\tau} - ay_{23\tau})
\end{aligned} \tag{3.29}$$

The effectivity of the proposed method will be verified by calculating the Eqs. 3.29 and 3.23. The parameters are taken as follows: $\tau = 0.01$, $\sigma = 10$, $r = 28$ and $b = 8/3$, which ensures the time-delayed system used for encryption in chaotic state. For simplicity but not losing generality, the mismatched parameters $\Delta\sigma$ and Δb are set to be 0, and only $\Delta r = 1$. The calculation result is shown in Fig. 3.15, where it is seen that the time series of x_1 of the commander and y_{21} of the sensor node 2 is achieved CS, which also can be further verified by plotting x_1 vs y_{21} and error dynamics $e = x_1 - y_{21}$, as shown in Fig. 3.15 (b) and Fig. 3.15 (c). The CS of other dimensions of the systems have achieved CS as well, which are not shown here. In addition, the chaotic attractors of the commander and sensor node 2 are shown in

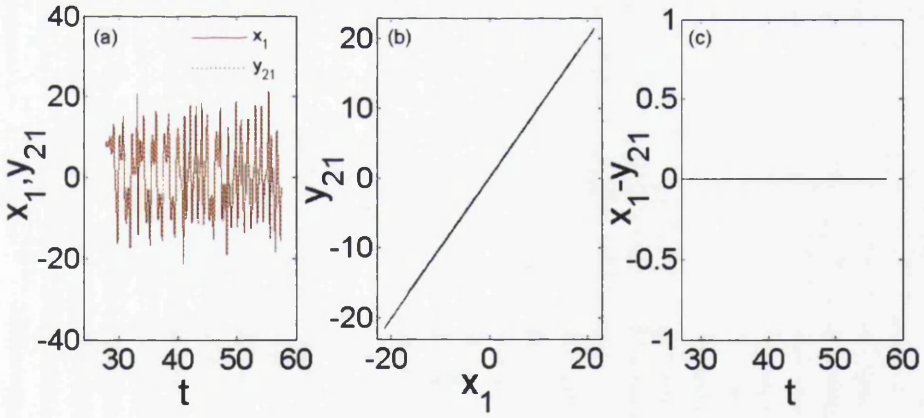

Fig. 3.15 Calculated results show that the complete synchronization (CS) between the base system and the sensor node 2 has been reached. (a).The time series of x_1 and y_{21} are plotted. (b) and (c) show the calculated results of x_1 vs.y_{21},and the e vs t, respectively.

Fig. 3.16, where it is once again seen that the two systems are completely synchronized with both in chaotic state.

As it is discussed in the first part of this chapter that in practical communication systems, the noise is always unavoidable. Here, a white Gaussian noise $\xi(t)$ [90], represented by random signal with a constant power spectral density and characterized by $\langle \xi(t) \rangle$, has been

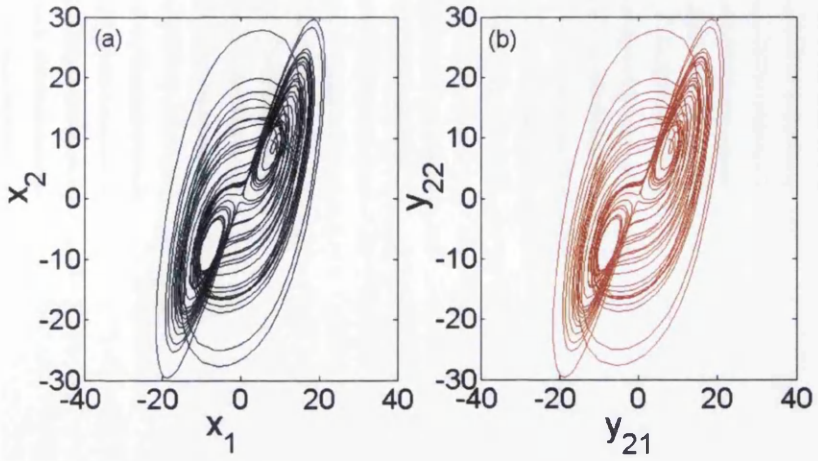

Fig. 3.16 Calculation results of the projection of attractor in x_1-x_2 plane is plotted in (a). (b) shows the projection of attractor in the second sensor node.

considered. The $\xi(t)$ can be generated by using Matlab function $\xi(t) = wgn(t, 1, p)$, where p specifies the power of $\xi(t)$ in decibels relative to a watt. In this study, the p is taken as 0, and the white Gaussian noise with a calculated signal-to-noise ratio 13 dB has been added to both the base station and sensor node 2. The result is shown in Fig. 3.17, where the spectrum versus time is plotted in Fig. 3.17 (a), and in Fig. 3.17 (b) and Fig. 3.17 (c) it is shown that proposed method is still robust even with the presence of the noise.

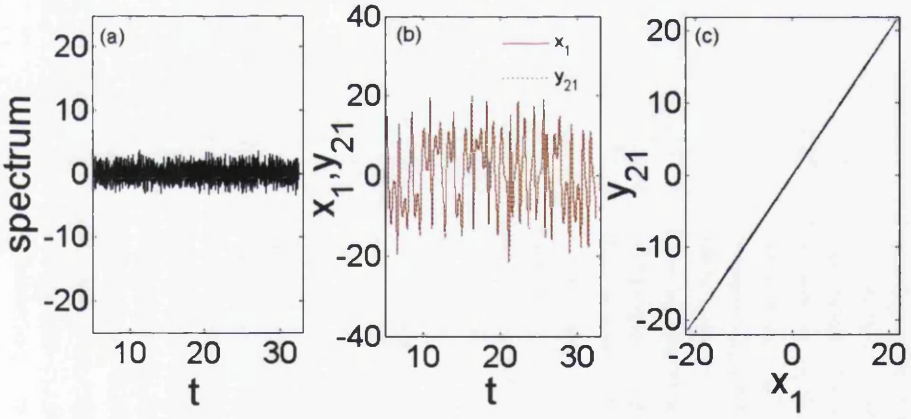

Fig. 3.17 Calculated results show that the complete synchronization (CS) between the base system and the sensor node 2 has been reached under the Gaussian white noise. (a) shows Gaussian white noise signal; y-axis of (a) shows the amplitude of the column vector containing real white Gaussian noise of power 0 dBW. The calculated results for time series of x_1 and y_{21} is shown in (b), x_1 vs. y_{21} is shown in (c).

3.8 Conclusion Remarks

In summary, a novel sensing system with two synchronized MEMS resonators has been proposed and simulated for mass sensor applications. Two MEMS resonators that are all working at the chaotic state have been synchronized using the OPCL based method. One of the MEMS resonators is used as the sensing element, while the other is used as the reference. OPCL algorithm has been applied again for a given range of mass attached; it is shown that under a certain range of mass change ($0 \sim 0.07m$), MLE remained positive confirming that the resonator is in chaotic state. Quantitatively, it has been calculated that for this particular system, the similarity measure δ varies from 0 to 3.25×10^5 for effective mass of the sensing MEMS resonator increasing from m to 1.07 m.

Although two identical MEMS resonators are presented in this work, it is predicated that the methodology can also be applied to two parameter-mismatched MEMS resonators. A practical system has also been discussed based on electrostatically driven doubly clamped resonators. The impact from environmental noises has been analysed for both sensing resonator and fixed resonator.

In the second part of this chapter, a new idea of achieving secured communication between the base station (commander) and sensor nodes in a WSN has been proposed based on a modified OPCL based method. Time-delayed Lorenz system has been used to form the chaotic signals that are added to sensors and the base station. In this method, the chaotic signal in sensor nodes will be unchanged, but the chaotic signal of the base will be modified using the OPCL synchronizer. In the mathematical expression of the synchronizer, the only changing item is the matrix C that is used for identifying each sensor node. A case study exhibiting the synchronization between one of the sensors and the base has been presented, and it is shown from the results that complete synchronization can be reached.

Chapter 4

Analysis of Intrinsic Localized Mode in Microelectromechanical Cantilever Array

4.1 Background

Intrinsic localized modes (ILMs) that are well known as "discrete breathers" or "lattice solitons" have been gaining attention since they were found by Sievers and Takeno in 1988 [91]. The ILM is a spatially localized and temporally periodic solution, which arises from the inherent nonlinearity of the systems, and has been proved to be a general phenomenon in various fields, such as in Josephson junctions, optical waveguide arrays, photonic crystal circuits, Bose–Einstein Condensates (BECs) in optical lattices [92][93][94] etc. Tremendous number of studies on proving the existence of the ILMs, investigating the dynamical stability and movability of the ILMs and developing computational methods to obtain ILMs have been contributed.

In work [95], the authors reported the observation of ILMs in the system of nonlinear electrical lattice. They claimed the first evidence of the ILMs can be generated, and especially, stabilized by sub-harmonic and/or parametric driving which is homogeneous in space. In work [96], Daniel Brake et al. investigated the possibility of generating and observing the ILMs in crystalline linear array of nano pillars, and they concluded that the ILMs do form in this system but they were strongly affected by the crystals properties. M. E. Manley et al. in [97] reported their experimental observation of ILMs in a remarkably simple ionic crystal, NaI, at high temperatures, and the consistency with the classical predictions and molecular dynamic simulations had been proved. The existence of ILMs in metallic crystals [98]

such as Ni and Nb, in Heisenberg ferromagnetic spin chain [99] and in a discrete electrical transmission line [100] have also been reported.

Moreover, the travelling ILMs in one-dimensional homogeneous granular chains with no precompression have been studied by Yuli Starosvetsky et al. [101]. By computing the different families of nonlinear travelling waves with the developed systematic semi-analytical approaches, they demonstrated that homogeneous granular chains possess complex intrinsic nonlinear dynamics. The mechanism responsible for ILMs motion in the electrical lattice was studied by L.Q.English et al. [102], and furthermore, they demonstrated the manipulation of ILMs experimentally. By conducting the molecular dynamics simulations, the crucial role of ILMs in the atomic scale as a trigger of defecting nucleation in carbon nanotube (CNT) [103] and transferring concentrated vibrational energy over large distances along crystallographic directions [104] has been investigated.

While, there is another important research branch of ILMs that deserves a mention here, i.e. ILMs in nonlinear discrete mechanical systems. The first experimental observation of ILMs in such a systems were claimed by M. Sato et al. in [105], where the authors found the ILMs by imaging and recording the time-dependent vibration envelope of a micro-mechanical oscillator array in the presence of a chirped driver. And subsequently, by employing the Klein–Gordon lattice model, detailed work on the dynamics of ILMs in micro-mechanical oscillator array such as creation, locking, interaction, and relaxation had been conducted by them [106]. The position shift of ILMs in the mechanical beam array were achieved by using a local impurity [107], and the dynamical stability of ILMs in the same system were also numerically investigated [108]. By taking a parametrically driven nonlinear resonators array as a platform, Eyal Kenig et al. studied the ILMs by using an amplitude equation in the form of nonlinear Schrödinger equation. The creation, stability, and interaction of ILMs were investigated, and also the authors confirmed that the ILMs can form bound states and two ILMs could be splitted from one [109]. Experimentally, a newly proposed macro-mechanical cantilever array that consists of cantilevers, electromagnets faced on the cantilevers, elastic rods for coupling between cantilevers, and a voice coil motor for external excitation were tested for realizing ILMs in work [110], which have provided a suitable experimental model to study the manipulation of ILMs using localized impurity.

Following on the above works, lots of efforts have been made with the aim for understanding ILMs from the viewpoint of dynamics and controlling. For example, the relationship between ILMs and nonlinear vibration modes were investigated [111]. The work has answered the question: could ILM be possibly realized as a forced nonlinear normal mode or nonlinear vibration mode? In experiment work [112], the bifurcation dynamics of an ILMs in a driven 1-D nonlinear mechanical lattice was studied. By measuring the linear

response spectrum of the auto-resonant ILM, the authors have argued the important role of soft-phase mode and its four-wave-mixing partner playing in the bifurcation transitions. Still by the same group, recently, they experimentally investigated the dynamical behaviour of an ILM in 1-D cantilever array when the laser-induced impurities were placed nearby. The ILM was found to be attracted or repulsed depending on the frequency of the impurity modes. The dynamical mechanism of ILMs that arises in mechanical beam array was studied systematically by Qingfei Chen el al. [37]. They argued that the conditions such as initial noise and frequency chirping scheme that had been considered to be necessary for realizing ILMs can all be relaxed, and it is the inherent spatio-temporal (ST) chaos which provides the natural platform for realizing the ILMs. By conducting a detailed bifurcation analysis, they have found the ST chaos in the system is ubiquitous, while under such nonlinear regime, many possible unstable modes are existing and a sudden frequency change could be capable of "restoring" the ILMs from the corresponding ILM saddles. In another work of them [113], they addressed the problem whether an arbitrary site in a micro-electromechanical cantilever arrays can be a desirable target for realizing ILMs. They have designed a global closed-loop control strategy that takes advantage of the spatial heterogeneity and temporal irregularity offered by ST chaos, and they also proposed a possible experimental scheme for realizing the strategy.

Can ILMs in the MEMs oscillator arrays be used for energy harvesting? In the past decade, with the increasing exploration of micro-scale energy harvesting devices, optimising energy output has been one of the predominant targets in many investigations. Research was conducted to maximize the energy output for the vibrational energy harvesting devices by designing arrayed cantilever beams [114], using the 'square shaped' coil structure [115], and making use of nonlinear vibrations [116]. For arrayed structures, a hypothesis would be whether operating the energy harvesting devices at ILM could achieve higher energy output.

The work in this chapter discusses a novel approach simulating an arrayed energy harvesting beams that are driven to ILM, which is targeted to discover whether the device operated at ILM can achieve high/concentrated power output. In the following, the contents will start by introducing the basic of piezoelectric theory that will be employed for calculating the charge generation, and then an energy harvesting device model will be presented. Based on the parameters taken in previous experimental works and by combining beam theory with the piezoelectric equations, the analysis of realizing ILM in the proposed structures will be given. After the realization of the ILM, the output of the charge in the energy harvester will be calculated, and the comparison with the case when there is no ILM arising will be conducted too. In the end, a bifurcation analysis of a two cantilevers system will be studied,

which is expected to shed light on understanding the ILMs in this energy harvesting cantilever array.

4.1.1 Piezoelectric Effect

Piezoelectric effect reflects the direct coupling between the mechanical and the electrical state in crystalline materials such as ZnO, and essentially it relies on the electric dipole moments inside the solid. Take the ZnO for example, it has the wurtzite crystal structure that polarization of ions in crystals is non-central symmetry [117], and when the stress is applied there is piezoelectric effect created, as shown in Fig. 4.1. Mathematically, the piezoelectric

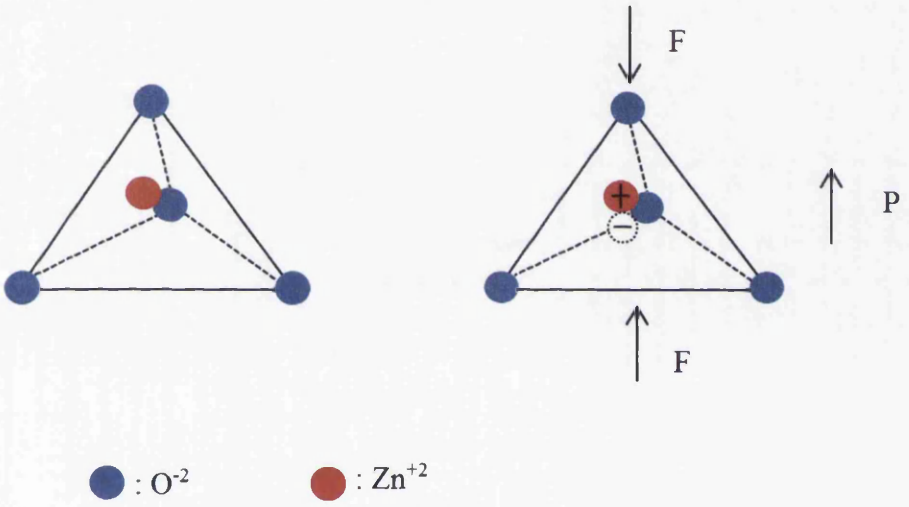

Fig. 4.1 The crystal structure of ZnO (left) and the polarization due to the applied force (right).

effect in the material can be described by the conventional theory of piezoelectricity and elasticity, and the constitute equation is given by:

$$\{D\} = [d]\{\sigma\} + [\varepsilon^T]\{E\} \tag{4.1}$$

where D is matrix for the electric displacement, $[d]$ is the matrix for piezoelectrical coefficients, σ is the matrix for stress field, $[\varepsilon]$ is the permittivity and T stands for transposition of

a matrix, and E is the electric field in the material. Specifically, the Eq. 4.1 can be written as:

$$\begin{bmatrix} D_1 \\ D_2 \\ D_3 \end{bmatrix} = \begin{bmatrix} 0 & 0 & 0 & 0 & d_{15} & 0 \\ 0 & 0 & 0 & d_{24} & 0 & 0 \\ d_{31} & d_{32} & d_{33} & 0 & 0 & 0 \end{bmatrix} \begin{bmatrix} T_1 \\ T_2 \\ T_3 \\ T_4 \\ T_5 \\ T_6 \end{bmatrix} + \begin{bmatrix} \varepsilon_{11} & 0 & 0 \\ 0 & \varepsilon_{22} & 0 \\ 0 & 0 & \varepsilon_{33} \end{bmatrix} \begin{bmatrix} E_1 \\ E_2 \\ E_3 \end{bmatrix} \tag{4.2}$$

According to the Eq. 4.2, the charge generated due to the stress field can be calculated, where the relevant coefficients involved are normally given by the material.

4.2 Model Construction

An array that consists of 64 identical pairs of bi-morph microelectromechanical (MEM) oscillator has been constructed in this section. In each pair, or can be called an unit, there are two beams with different length. Each beam has two layers made of different materials. One is piezoelectric material film that can be used to convert strain to electrical charge. The other one is serving as the mechanical support. The specific materials of the two layers have been chosen to be zinc oxide (ZnO) and silicon nitride (Si_3N_4), respectively. ZnO, as an environment-friendly and low-cost material, has been widely used in energy harvesting, especially in the nano-scale self-powered sensing field [118]. The energy harvesting devices based on ZnO have high energy transfer efficiency. Therefore, taking ZnO as the material in this model has significance for exploring the potential applications that use ZnO as the energy harvesting component. Si_3N_4 has good elastic properties, and it is always adopted for making cantilevers. Besides, in this model Si_3N_4 substrate because of its electronic properties, it plays the role as an insulator layer. An unit of the MEM array is shown schematically in Fig. 4.2, where it is seen that the two beams are root-connected by overhang. The length of the two beams are represented by L_i and L_{i+1}, respectively, where index i represents the position of the beam in the array. The other geometrical and mechanical properties of the model are listed in table 4.1.

4.3 Model Analysis

There is stain induced in the beams of the MEM array when they are vibrating. In Fig. 4.3, a typical deformation of a beam has been plotted. According to Klein-Gordon equation [119],

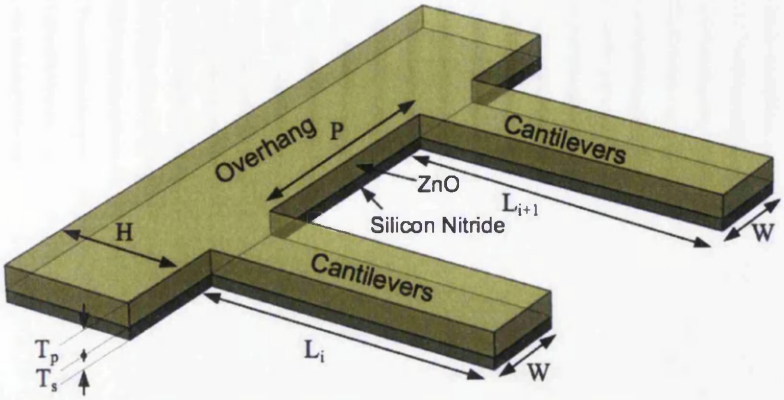

Fig. 4.2 Schematic of a single cantilever unit consisting two coupled cantilevers with identical widths and slightly different lengths.

Table 4.1 The material and geometrical parameters of two beams in one unit.

Layer name	ZnO	Silicon nitride
Length of the beams(μ m) L_i/L_{i+1}	50/55	0.91
Thickness(μ m)	$T_p = 0.2$	$T_p = 0.1$
Width (μ) W	15	15
Density (kg/m) ρ	5606	2300
Poisson's Ratio ν	0.36	0.28
Young's modulus(Gpa) E	161	110

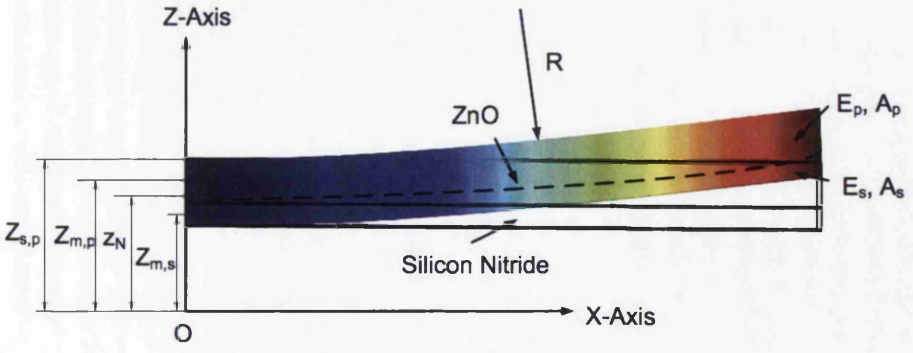

Fig. 4.3 Schematic of the cross-sectional view of a bimorph beam.

the dynamical motion of the beam i ($i = 1,2,...,128$) can be described by the following equation when only the coupling effect from neighbour beams is considered:

$$m_i\ddot{z}_i + b_i\dot{z}_i + k_{2i}z_i + k_{4i}z_i^3 + k_I(2z_i - z_{i+1} - z_{i-1}) = m_i acos(2\pi ft) \tag{4.3}$$

In Eq. 4.3, m_i is the effective mass, b_i is the damping coefficient, k_{2i} and k_{4i} are on-site harmonic and the quadratic spring constants of the beam i, respectively. k_I is the coupling coefficient among the beams, which is determined by properties of overhang as shown in Fig. 4.2, and it is usually extracted from experimental data. The $m_i acos(2\pi ft)$ represents the external drive force in which a is the acceleration and f is driving frequency. z_i is the tip displacement of the ith beam.

In order to calculate the induced strain due to the vibration in an instant time t, the vibrating beam can be assumed to be a part of arc with radius R, as shown in Fig. 4.3. Because the beam thickness is much less than the induced arc, the R is taken the same for both layers. Thus, the curvature r_i of beam i can be derived from tip's displacement $z_i(t)$, which is given by:

$$\frac{1}{r_i} = 2z_i/L_i^2 \tag{4.4}$$

It should be noted that the curvature induced by shear effect and residual stress has been ignored. Now the axial strain $\varepsilon_{x,i}$ that induced on the surface of the piezoelectric layer (top layer) can be calculated based on the beam theory [120], as:

$$\varepsilon_{x,i} = \varepsilon_{x,i}(Z_{s,p}) = \frac{z_N - Z_{s,p}}{r_i} \tag{4.5}$$

where z_N is the neutral axis between two layers, defined from arbitrary reference, and the $Z_{s,p}$ is the distance between the same reference and the top surface of the piezoelectric layer. The z_N can be obtained by:

$$z_N = \frac{Z_{m,p}E_pA_p + Z_{m,s}E_sA_s}{E_pA_p + E_sA_s} \tag{4.6}$$

where $Z_{m,p}$ and $Z_{m,s}$ are the distance from the middle of the layers to the same reference as for the z_N, respectively. E_p and E_m are Young's modulus for the piezoelectric and substrate layers, respectively. A_p is the cross section area of the piezoelectric layer and A_m is substrate's. The axial stress $\sigma_{x,i}$ in the piezoelectric layer of beam i can be derived by using the Hooke's

law and piezoelectricity theory, as:

$$\sigma_{x,i} = E_p(\varepsilon_{x,i} - d_{31}\bar{E}) \tag{4.7}$$

where d_{31} is the piezoelectric coefficient of the ZnO layer, which determines the intensity of the coupling between the external electrical field $\bar{E}$ and axial stress.

The electric filed displacement D_i generated on the piezoelectric layer i is defined by:

$$D_i = \varepsilon_{x,i}\bar{E} + d_{31}\sigma_{x,i} \tag{4.8}$$

Combining Eq. 4.7, Eq. 4.8 and Eq. 4.5, the electric filed displacement D_i can be further expressed as:

$$D_i(t) = 2d_{31}E_p(z_N - z)z_i(t)/L_i^2 \tag{4.9}$$

where the external electrical field is zero. It is obvious to see that in Eq. 4.9 the electric filed displacement D_i and the induced strain ε_i have been related. In equation. 4.9, the z is the position of the piezoelectric material along z-axis, and therefore the electrical displacement on the surface of the piezoelectric layer can be obtained by taking $z = Z_{s,p}$, which is:

$$D_i(t) = 2d_{31}E_p(z_N - Z_{s,p})z_i(t)/L_i^2 \tag{4.10}$$

So the electrical charge generated due to mechanical strain across on the surface of the beam i is described as:

$$Q_i(t) = D_i(t)WL_i = \frac{2Wd_{31}E_p(z_N - Z_{s,p})}{L_i} \cdot z_i(t) \tag{4.11}$$

The Eq. 4.11 gives the linear relation between the generated charge on beam i and its tip's displacement at an instant time, and if combining with Eq. 4.3 the dynamical expression of Q_i can be derived, which is:

$$m_i\ddot{\bar{Q}}_i + b_i\dot{\bar{Q}}_i + k_{2i}\bar{Q}_i + k_{4i}\bar{Q}_i^3 + k_I(2\bar{Q}_i - \bar{Q}_{i+1} - \bar{Q}_{i-1}) = m_i acos(2\pi ft) \tag{4.12}$$

where the relation $\bar{Q}_i = L_iQ_i/(2d_{31}E_p(z_N - Z_{s,p})W)$ has been used, and here the symbol $\bar{Q}$ is used for easy demonstration of electrical charge generated by the device.

4.4 ILM Realization

It is known that when the amplitude of the external driving source is sufficiently large and the frequency of the driving source is close to the resonant frequency of the beam, the beam will be in the dynamical bi-stable region where there are two stable states exhibiting different amplitudes [113], which provides the necessary condition for realizing ILMs. In the bi-stable region, the state that has the higher amplitude is actually the ILM and the other one in low energy state (LES). However, in an MEM array that has many beams coupled together, the dynamics of each beam becomes complicated, and ILMs are usually not stable. Under a certain driving frequency and amplitude, the MEM array would be in a modulational instability state, in which the ILMs exist as unstable saddles. The dynamics of each beam in such a state is chaotic, and the vibrating state of the beam are approaching now and then to various ILMs saddles. If at this moment the driving frequency changed abruptly which behaves like a perturbation, one ILM would be captured when the vibration of the beam is visiting the neighbourhoods of the ILMs saddles. Therefore, it is necessary to realize the modulational instability state in the MEM array before achieving ILM. In this model, the modulational instability state also means chaotic state.

In the following simulation, the parameters of the dimensions and material properties of the MEM array are taken from table 4.1. The harmonic k_{2i} and the quadratic spring constants k_{4i} of beam i are calculated by:

$$k_{2i} = \frac{12.36E_eI}{L_i^3}, \quad k_{4i} = \frac{24.79E_eI}{L_i^5} \tag{4.13}$$

according to [107], where E_e is the effective Young's modulus, and it can be obtained by: $E_E = E_pT_p + E_sT_s/(T_p + T_s)$. The I in the Eq. 4.13 is moment of the inertia, and it can be given by: $I = (W \times T^3)/(12)$. The effective density $\rho_e = \rho_pT_p + \rho_sT_s/(T_p + T_s)$ of the beam also has been taken into account for calculating the effective mass. $b_i = 6.24 \times 10^{-11} kg/s$, $d_{31} = -2.3pC/N$ and $k_I = 0.0241$ [105]. The driving frequency is set as: $f = 1.151 \times 10^5 Hz$, which is chosen closing to the fundamental resonant frequency of the beams.

Based on the parameters above, the numerical simulation based on the set of Eqs. 4.12 has been conducted. Firstly, the time series of the equivalent charge $\bar{Q}$ generated on the 43^{th} beam has been plotted in Fig. 4.4, where it is shown that the series of charge generation time is bursting in various short time intervals, which proves the happening of the modulational instability state. It should be mentioned that the modulational instability state also exists on other beams even though only the 43^{th} has been plotted. A global picture of the MEM array's charge generation in both spacial and temporal dimensions when all the beams are in

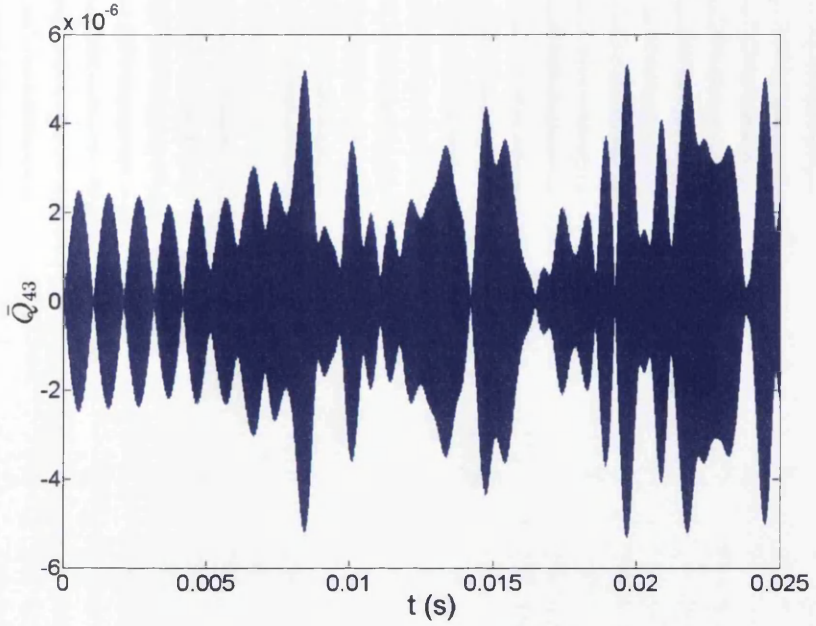

Fig. 4.4 Equivalent generated electrical charge $\bar{Q}_i = 0.035Q_i$ on 43^{th} beam is plotted with parameters: $m_1 = 9.88 \times 10^{-13}$ kg; $b_1 = 5.76 \times 10^{-11}$ kg/s; $k_{21} = 0.46$ N/m; $k_{41} = 3.85 \times 10^8$ N/m^3; $m^2 = 10.49 \times 10^{-13}$ kg; $b_2 = 6.24 \times 10^{-11}$ kg/s; $k_{22} = 0.36$ N/m; $k_{42} = 2.39 \times 108$ N/m^3; $f = 1.151 \times 10^5$ Hz; $\alpha = 1.78 \times 10^4$ m/s^2; $kI = 0.0241$.

modulational instability state has been presented in Fig. 4.5. It is seen that in Fig. 4.5 that all

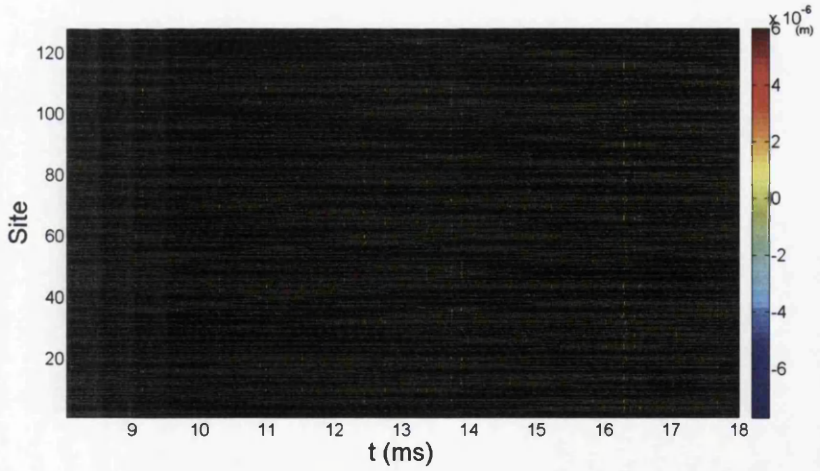

Fig. 4.5 Spatio-temporal chaos for all the beams versus time before changing the driving frequency with parameters same as used in Fig. 4.4. It shows that all beams are experiencing chaotic vibrations but no obvious ILM.

the beams are in ST chaotic state, which is ready for realizing the ILMs [37]. As we can see,

there are many signatures of ILM saddles indicated by deep colour in Fig. 4.5, signifying the vibrating trajectory of beams to visit the neighbourhoods of various ILM saddles randomly. In order to have an insight on how the beams are visiting the ILM saddles, the $\bar{Q}$ for all the beams in a certain instant time $t = 0.016s$ has been plotted in Fig. 4.6, where it can be seen that a large spikes appears instantly at one site of the MEM array. If another instant time is calculated, the large spike may appear in some other beam sites, which can be seen as one of distinctive features of the ST chaotic state. As it is discussed in last section that an abrupt

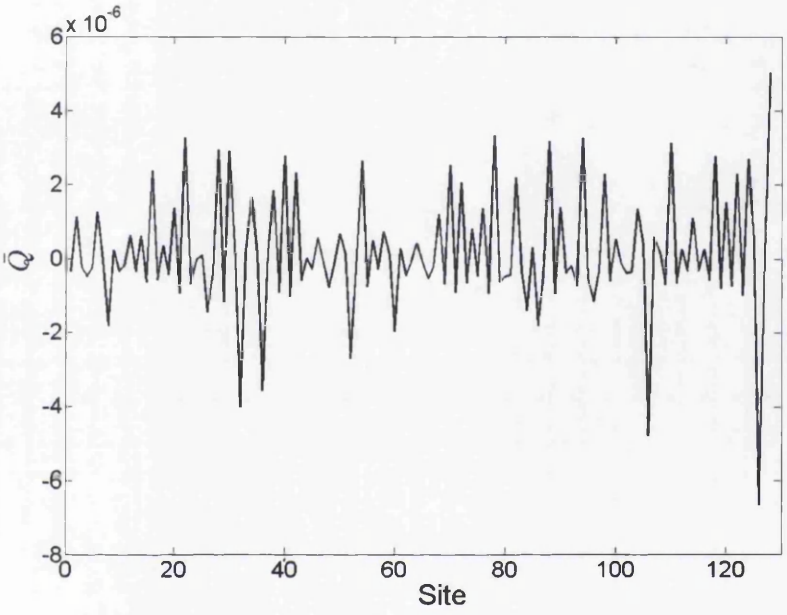

Fig. 4.6 Spatial profile of the charge generation at $t = 0.016$ s.

driving frequency change can be seen as a perturbation that may lead to ILM occurring. Next, an abrupt frequency change has been applied at $t_b = 0.0188s$ when the driving frequency is increased to 1.1763×10^5. The result has been shown in Fig. 4.7. It is seen that one ILM is occurring at site 60^{th} indicated by the dark colour line, while there are other unstable ILMs occurring on the other beams. The next step is to investigate the power output of the MEM array when it has the ILM. Firstly, a comparison of charge generation between the 60^{th} and 97^{th} beam has been given in Fig. 4.8, where it is seen that the charge generated on 60^{th} is approximated 10 times higher. Then, the absolute charge generation of the ILM beam has been plotted in Fig. 4.9, where the peak to peak charge generation is about 0.3 pC. Lastly, the total charge generation of the 128 beams with respect to two states: without ILM and with ILM have been calculated, as shown in Fig. 4.10 and Fig. 4.11, respectively, where it can be concluded that the output is higher when the MEM array has the ILM.

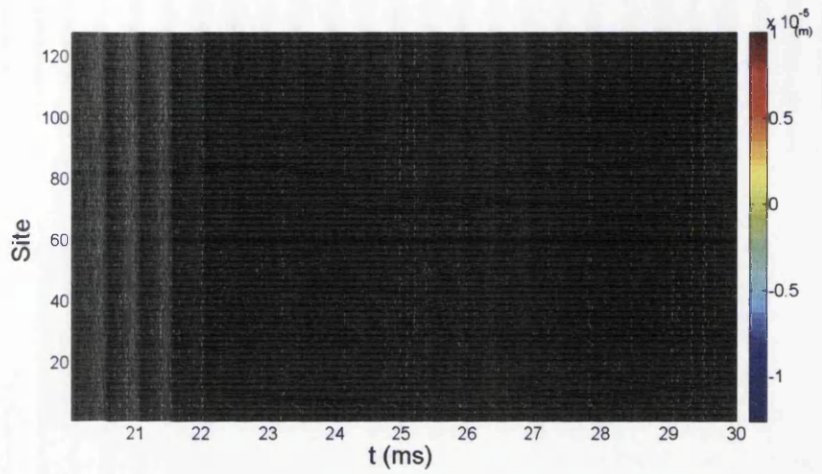

Fig. 4.7 ILM on the 60^{th} beam after changing the driving frequency abruptly to 1.1763×10^5 Hz at $t_b = 0.0188$ s.

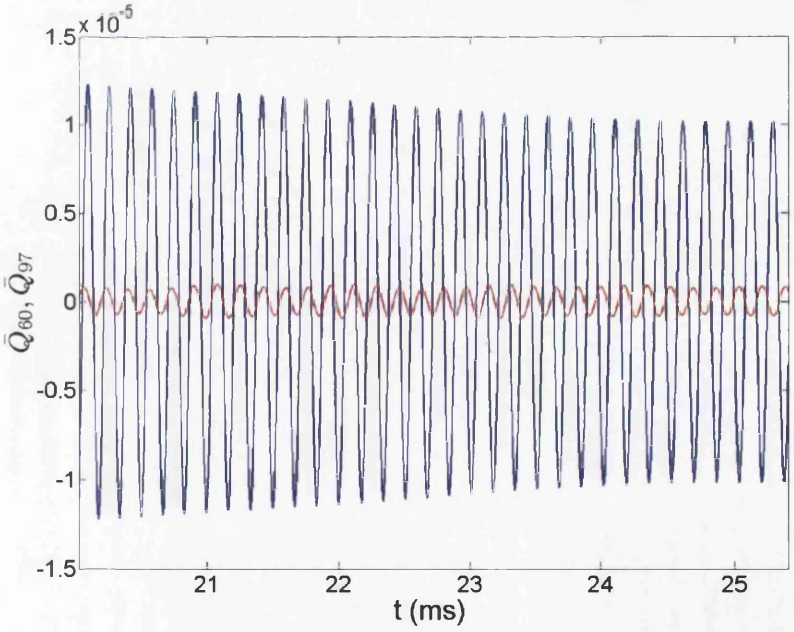

Fig. 4.8 Comparison of charge generations by the 60^{th} beam and 97^{th} beam with parameters same as used in Fig. 4.4 except for the driving frequency $f = 1.1763 \times 10^5$ Hz at which ILM appears on the 60^{th} beam.

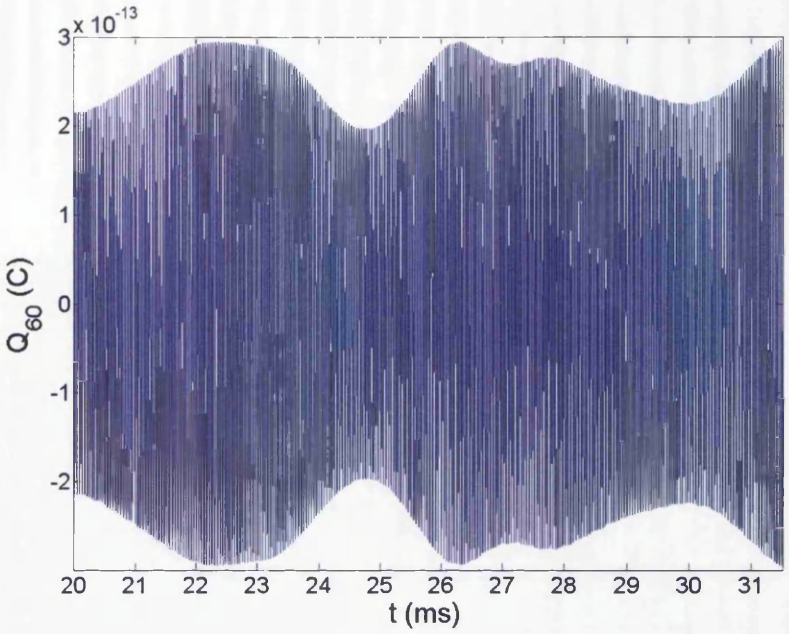

Fig. 4.9 The absolute charge generation from the beam 60^{th} when it works at ILM state.

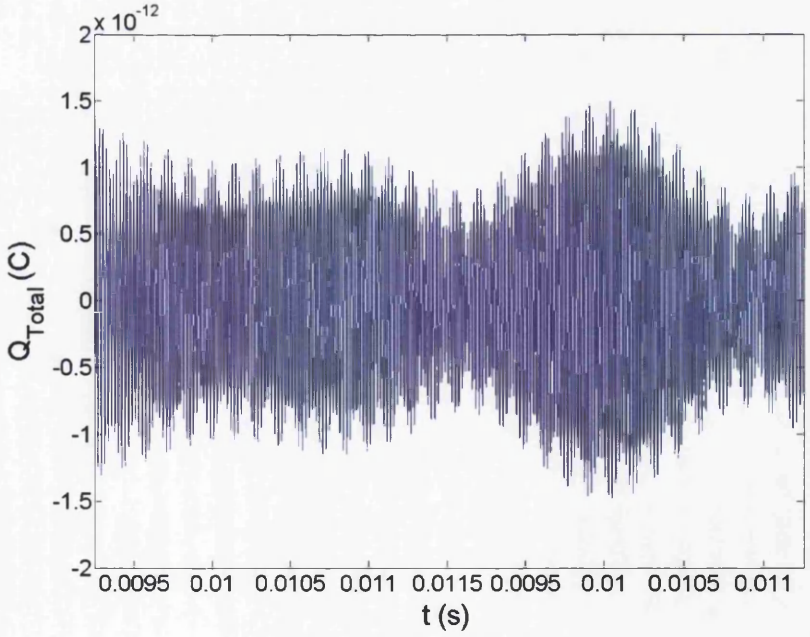

Fig. 4.10 The total charge generation of the 128 beams when it is in chaos state.

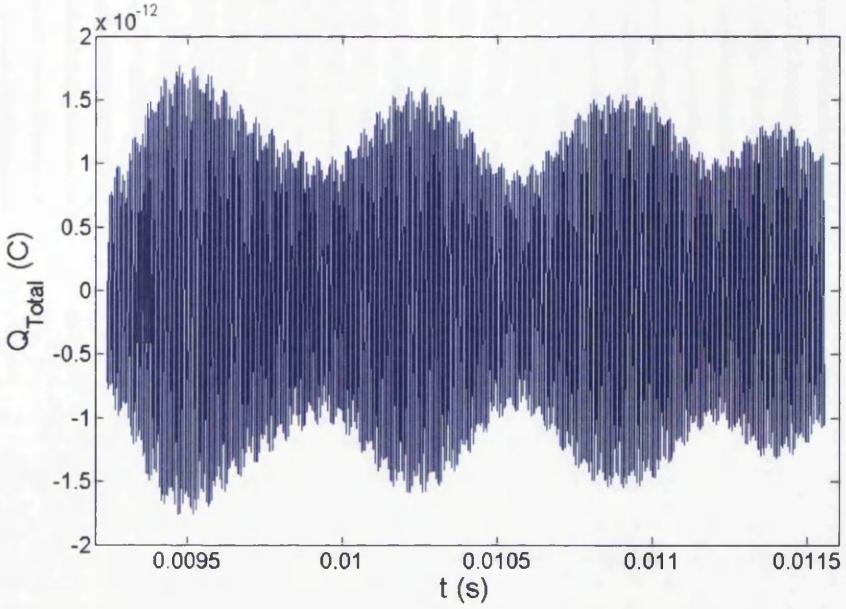

Fig. 4.11 The total charge generation of the 128 beams when it is in ILM state.

4.5 Bifurcation Analysis

As discussed in the above sections, the generation of ILMs in the MEM array are essentially relying on the platform provided by the occurrence of modulational instability state (ST chaos), in which many unstable ILMs saddles exist. The bifurcation analysis of the route to modulational instability state is expected to shed the light on understanding the ILMs. Here, a bifurcation analysis of a representative unit of the MEM array has been conducted. The K_I is taken as the bifurcation parameter.

By employing averaging technique [121], the solution of Eq. 4.12 can be assumed as:

$$\bar{Q}_i = X_i(t)cos(2\pi ft) - Y_i(t)sin(2\pi ft) \tag{4.14}$$

Then substituting the Eq. 4.14 to Eq. 4.12 and conducting the periodic averaging, a new set of equations can be obtained, as:

$$\begin{aligned}
\dot{X}_i &= -\frac{1}{4\pi f}\left[(4\pi^2 f^2 - \frac{k_{2i}}{m_i})Y_i - \frac{3k_{4i}}{4m_i}Y_i(X_i^2 + Y_i^2) + \frac{2\pi f b_i}{m_i}X_i + \frac{k_I}{m_i}(Y_{i+1} - 2Y_i + Y_{i-1})\right] \\
\dot{Y}_i &= \frac{1}{4\pi f}\left[(4\pi^2 f^2 - \frac{k_{2i}}{m_i})X_i - \frac{3k_{4i}}{4m_i}X_i(Y_i^2 + X_i^2) + \frac{2\pi f b_i}{m_i}Y_i + \frac{k_I}{m_i}(X_{i+1} - 2X_i + X_{i-1})\right] + a
\end{aligned} \tag{4.15}$$

Based on the Eq. 4.15, and taking all other parameters as same as the above except for $f = 9.8 \times 10^4$ Hz, the equilibrium solutions of the unit system when $i = 1, 2$: X_{10}, Y_{10}, X_{20} and Y_{20}, have been calculated, which are shown in Fig. 4.12. In the Fig. 4.12, the relations $A_1 = \sqrt{X_{10}^2 + Y_{10}^2}$ and $A_2 = \sqrt{X_{20}^2 + Y_{20}^2}$ have been used, where A_1 and A_2 represent the amplitudes of beam 1 and beam 2, respectively. Meanwhile, the stability of the equilibrium solutions has been judged by linearizing the Eq. 4.15. It is shown in Fig. 4.12 that there are two stable equilibrium solutions of the unit system when $k_I < 0.016$ with beam 1 in ILM and beam 2 in LES. However, when the k_I is increased over 0.016, the two stable solution all lost their stabilities, from then the dynamics of the two beams start to behave in a modulational instability state.

Likewise, if $i = 128$ were considered, there should be also a k_I point existing, after which the MEM array will start to evolve into the ST state, and once such a state is occurred there is the possibility for realizing the ILM by frequency changing.

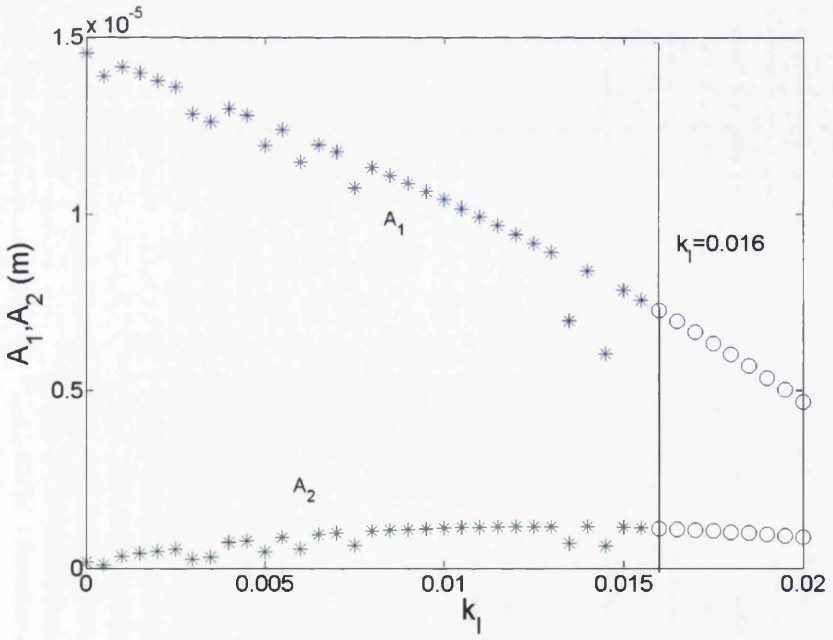

Fig. 4.12 The stable equilibrium solutions versus k_I. Stable equilibrium solutions are represented by $'*'$ before $k_I \approx 0.016$, after which the solutions have lost their stability, which is indicated by $\circ$.

4.6 Conclusion Remarks

In summary, a coupled energy harvesting bi-layer cantilever array has been modelled and analysed. The emphasis of this work is to innovatively analyse the nonlinear dynamic

behaviour of the beams to observe the ILM with the idea of realizing large energy output. It has been found that due to the nonlinear mechanical vibrations, the charge generated across the piezoelectric surface is representing the mechanical vibrations and exhibiting spatio-temporal chaos under suitable coupling k_I. It is seen from the simulation that the ILM can be triggered by varying the driving frequency from 1.151×10^5 Hz to 1.1763×10^5 Hz abruptly. The averaging equations of this model when $i = 2$ has been solved, which can explain why the ILM occurs qualitatively. The size of the cantilever array and the formation structure of the beam unit do have an effect for the occurrence of the ILM, as the dynamics of the whole structure is closely related to the geometrical parameters. However, in this work, it focus on the investigation that whether the ILM would increase the energy harvesting so only one specific model has been studied. It will be the further work to investigate how to achieve the optimal energy harvesting with varying size and structure. Overall, this work has potential applications in the energy harvesting devices, as it will increase the energy output significantly by operating the device in the ILMs.

Chapter 5

Chaos Control of Parametric Driven Duffing Oscillators

5.1 Backgroud

In the past few chapters, it has been discussing of the nonlinear phenomenons in MEMS/NEMS resonators, such as chaos in CNT nanotube resonator (chapter 2) and MEMS resonator (chapter 3), and ILMs in MEM resonators array (chapter 4). Mathematically, these systems have been modelled by a similar formalism (Duffing equation) as Eq. 1.2 given in the introduction chapter if without considering the specific external driving term. In the sense that different polarity of spring constant k_1 in Eq. 1.2, which determines the intensity as well as direction of the restoring force, the Duffing resonators can be further classified into two types: one with negative k_1 and the other one with positive k_1, which has been discussed in the first chapter.

Of the first type Duffing resonator with negative k_1, chaos has been experimentally observed. In the famous work [6], F. C. Moon and P. J. Holmes fabricated a ferromagnetic beam buckled between two magnets as shown in Fig. 5.1 (a), and they found the system can be modelled by a single degree of freedom oscillator with negative k_1. Both in the experimental and theoretical work, they proved the occurrence of deterministic chaos in the system. Systematic study of the model has been put in the book [121], where the author studies the global nature of the attracting motions arising as the result of bifurcations and characterizes the strange attractor by means of Poincaré map. Similar to the set-up in [6], a broadband piezoelectric power generation device was designed and tested. It is found that the generator can work both in periodic and chaotic state, and can generate an order of

magnitude larger power compared with the commonly employed piezoelastic counterpart at several frequencies [122].

The investigation of nonlinear dynamics in the other type of Duffing resonator with positive k_1 are more frequently seen [3][70] [71]. But of this type, there is one special kind of resonator which has a additional parametric driving (pump) added in parallel with the spring constant, has not been paid attention so far. According to existing works, parametric resonators are playing an important role for realizing functions such as parametric resonance and amplification, and have been extensively studied in the context of MEMS. For example, in [123], a parametric cantilever was devised as an amplifier, which can be used to produce mechanical squeezed states and improve force detection sensitivity. In [124], based on NEMS techniques, a very high frequency (>100 MHz) parametric amplifier were realized, as shown in Fig. 5.1 (b). The parametric amplification were also investigated in an array of piezoelectric NEMS systems [125]. In addition, MEMS oscillators utilising parametrically excited non-interdigitated comb drive actuators have been designed and characterized to demonstrate the tuning of oscillator stiffness [126], The presence of chaos was also discovered in this type of MEMS oscillators [127].

In this chapter, the chaos control in these two types of Duffing resonator will be discussed. As a matter of fact, to control the chaos in MEMS resonators has been a hot topic among the existing works. Many methods have been proposed and tried. For example, optical linear feedback control, SDRE control, Fuzzy sliding mode control, output-feedback control [38] and second-order fast terminal sliding mode control [128]. A control method that can also enhance the device output energy was proposed in [77].

While in this chapter, for the type of Duffing resonator with negative spring constant, the chaos controllability will be investigated by adding a parametric pump. The control method by using a weak harmonic perturbations has been verified to be effective [129][130], but to suppress chaos by adding the additional forcing term into spring constant as a pump has not been explored. Moreover, the research of chaos control in this type duffing oscillator has not been discussed too.

For the second type with positive constant, a parametric Duffing resonator that has been experimentally realized will be employed. Firstly, the reliability of the model will be verified by comparing with the experiment result. Whether the model have the deterministic chaos will be investigated, and by adjusting the driving conditions of pump, the chaos controllability will be investigated as well.

Conclusively, chaotic oscillations of resonating systems with negative and positive spring constants are identified to investigate in this chapter. Parametric driver imposed on these two systems affects nonlinear behaviours, which will be theoretically analysed with regard

to variation of driving parameters (frequency, amplitude). Systematic calculations will be performed for these two systems driven by parametric pumps to unveil the controllability of chaos.

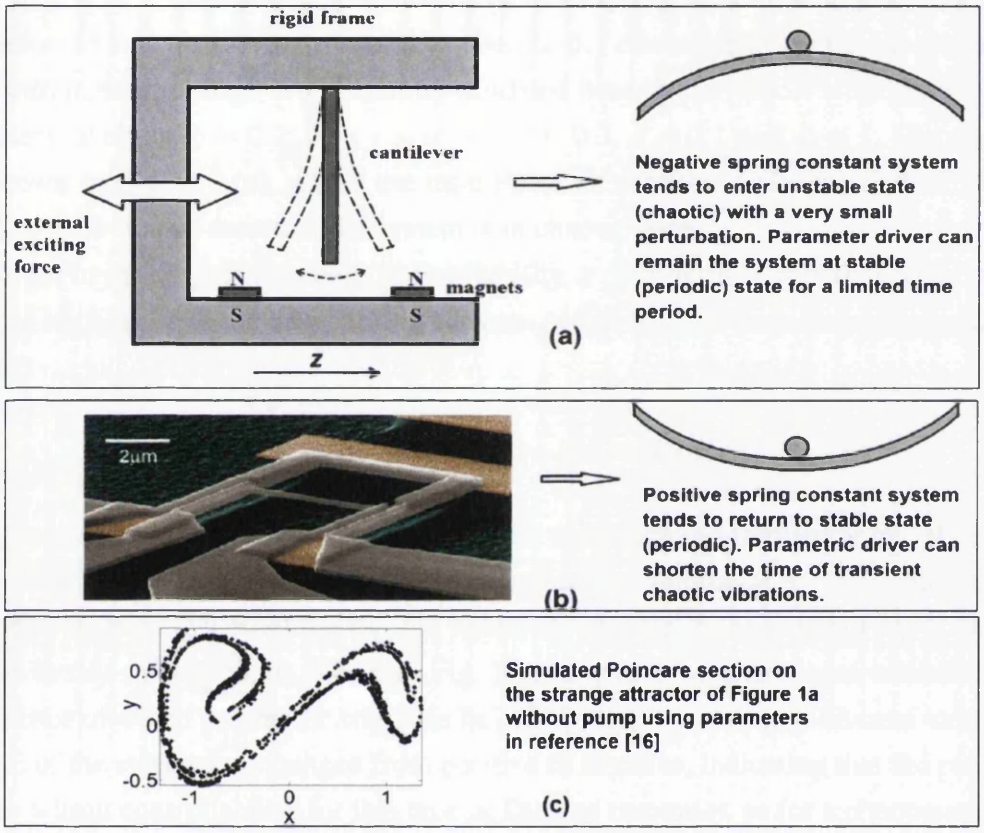

Fig. 5.1 (a) Schematic picture of a Duffing oscillating system with negative spring constant. (b) Scanning electron micrograph on the left shows a device made by Roukes group. (Reprinted with permission from R. B. Karabalin, X. L. Feng, and M. L. Roukes, Nano Lett. **9**, 3116 (2009). Copyright 2009 American Chemical Society.7) In this type of systems, from theoretical analysis presented in this paper, chaos can be remained for a limited time period. (c) The simulated poincare section on the strange attractor of the model (a).

5.2 Duffing Resonator with Negative Spring Constant

The vibration of the system in Fig. 5.1 (a) can be described mathematically by a non-dimensionalized equation that has been proved to be satisfactory with respect to the experiment [6], which is expressed as:

$$\ddot{z} + \delta\dot{z} + \beta z + \alpha z^3 = \gamma cos(\omega t), \tag{5.1}$$

where z represents the displacement in z-axis, δ is the damping ratio which depends on the working environment, β is the spring constant and it is negative in this case, α is the cubic spring constant that controls the amount of non-linearity in the restoring force. On the right side of the Eq. 5.1, the term stands for the external driving force in which γ is the driving amplitude and ω is the driving frequency. The Eq. 5.1 can exhibit chaotic behaviour given proper parameters settings, which can be validated here by numerical simulating with the parameters taken as: $\delta = 0.2$, $\beta = -1$, $\alpha = 1$, $\gamma = 0.3$, $A = 0.1$ and $\omega = 1$. The result has been shown in Fig. 5.1 (c), where the time Poincare section of phase z and $\dot{z}$ have been plotted. It is obviously seen that the system is in chaotic state.

In order to investigate the chaos controllability, a parametric driver that behaves like a pump has been added to the linear spring constant of Eq. 5.1, and the new motion equation is given by:

$$\ddot{z} + \delta\dot{z} + (\beta - A cos\omega_p t)z + \alpha z^3 = \gamma cos(\omega t), \tag{5.2}$$

where the added term $Acos\omega_p t$ has a amplitude A and a driving frequency ω_p. By keeping the parameters δ, β, α, γ, A and ω unchanged and taking amplitude $A = 0.2$, the Maximum Lyapunov exponent (MLE) of the Eq. 5.2 versus ω_p varying in the range of $\omega_p \in [0.8 \quad 10]$ has been firstly calculated, as shown in Fig. 5.3, in which the chaos controllability as the consequence of added parametric term can be clearly seen that in some discrete value of ω_p the MLE of the system has changed from positive to negative, indicating that the parametric term has a limit controllability for this type of Duffing resonator, as for a chaotic system its MLE should be positive. Furthermore, the time series of z, phase portrait (x vs. y, where the relations of $x = z$ and $y = \dot{z}$ have been employed) and Poincaré section of the system with some discrete parametric driving frequency ω_p have been calculated, as shown in Figs. 5.3, 5.4, 5.5 and 5.6. It is seen in Fig. 5.3 that when $\omega_p = 0.8$ the system is still in the chaotic state, while in Figs. 5.4, 5.5 and 5.6 the system has been controlled into periodic states. Specifically, by analysing the Poincare section, the system has been controlled into 1-period state when $\omega_p = 1$ (Fig. 5.4), in 4-period when $\omega_p = 1.5$ (Fig. 5.5) and in $\omega_p = 2$ (Fig. 5.6).

5.2.1 Melnikov's Method

With the aim for illustrating the mechanism of the parametric controllability, the Melnikov's method has been applied. Firstly, the Eq. 5.2 can be re-written in the perturbed form, as:

$$\begin{aligned} \dot{x} &= y \\ \dot{y} &= -\beta x - \alpha x^3 - \varepsilon(-\delta' y + A' cos\omega_p t x + \gamma' cos(\omega t)) \end{aligned} \tag{5.3}$$

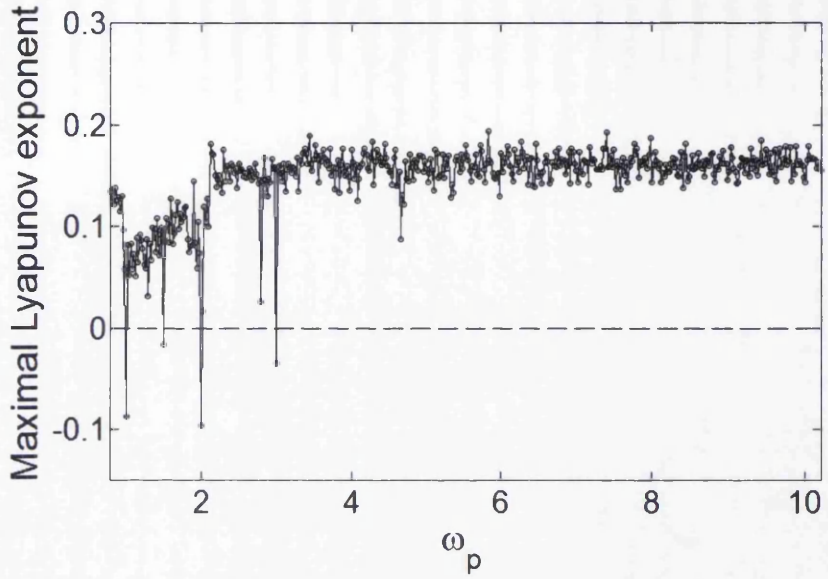

Fig. 5.2 Calculated MLEs of the Duffing system (negative spring constant) with a parametric pump with varying frequency ω_p.

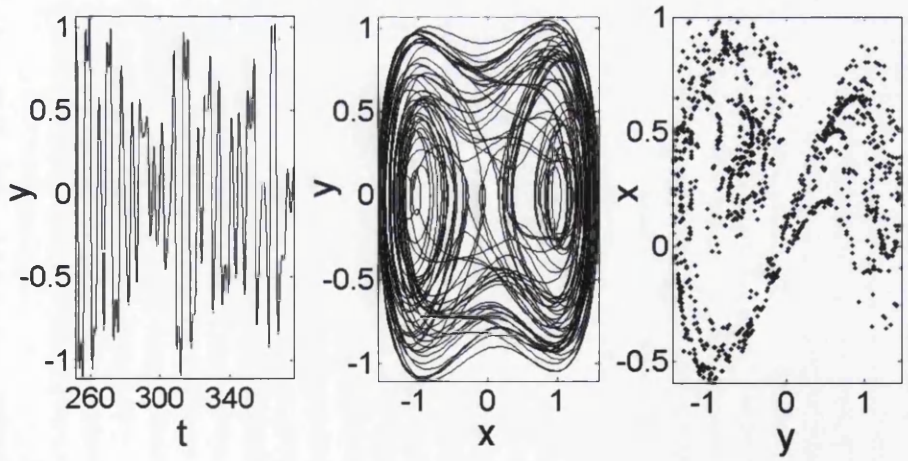

Fig. 5.3 Calculated phase portrait of the Duffing system (negative spring constant) with the parametric pump.

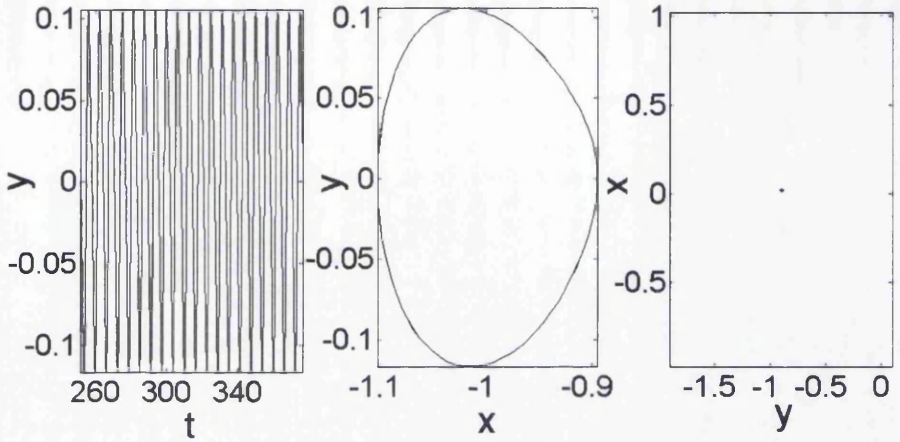

Fig. 5.4 Calculated phase portrait of the Duffing system (negative spring constant) with the parametric frequency $\omega_p = 1$.

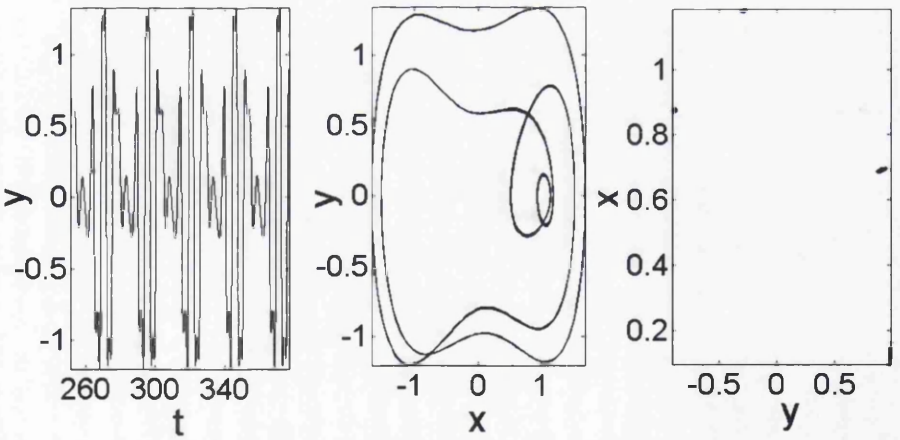

Fig. 5.5 Calculated phase portrait of the Duffing system (negative spring constant) with the parametric frequency $\omega_p = 1.5$.

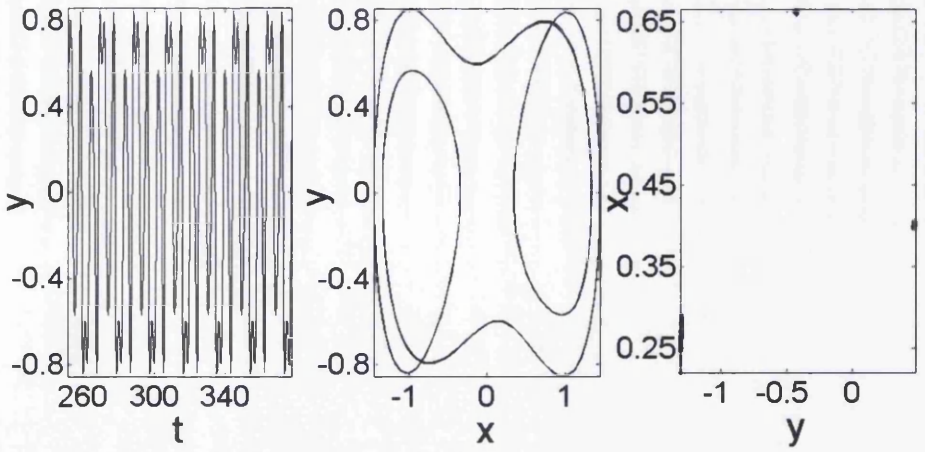

Fig. 5.6 Calculated phase portrait of the Duffing system (negative spring constant) with the parametric pump.

where $\varepsilon\delta' = \delta$, $\varepsilon A' = A$, $\varepsilon\gamma' = \gamma$, and ε is a small parameter. From the Eq. 5.3, the unperturbed system can be obtained, as:

$$\begin{aligned} \dot{x} &= y \\ \dot{y} &= -\beta x - \alpha x^3 \end{aligned} \tag{5.4}$$

, which is actually a Hamiltonian system, and its Hamiltonian function is given by:

$$H = \frac{1}{2}\delta y^2 + \frac{1}{2}\beta x^2 + \frac{1}{4}\alpha x^4 \tag{5.5}$$

, based on which the Eq. 5.4 ($\delta = 0$) can be derived easily by calculating $\dot{x} = \partial H/\partial y$ and $\dot{y} = -\partial H/\partial x$. One can derive easily that Eq. 5.5 has two homoclinic orbits $\Gamma_{\pm}$, which are given by:

$$\Gamma_{\pm} : (x_0(t), y_0(t)) = (\pm\sqrt{2}Sech(t), \mp\sqrt{2}Sech(t)\cdot tanh(t)) \tag{5.6}$$

where the $x_0(t)$ and $y_0(t)$ correspond the coordination of a specific point that evolves with time on the orbit $\Gamma_{\pm}$. Moreover, $x_0(t)$ and $y_0(t)$ will be used in solving the Melnikov function. The Melnikov function of the Eq. 5.3 is then obtained as:

$$M(t_0) = \int_{-\infty}^{\infty} [y_0(-\delta y_0 + \gamma cos\omega(t+t_0) + Acos\omega_p(t+t_0)\cdot x_0)]dt \tag{5.7}$$

t_0 is the time of flight from a point $(x_0(t), y_0(t))$ to the point $(x_0(0), y_0(0))$ on the homoclinic connection. Substituting Eq. 5.6 into Eq. 5.7, then the Eq. 5.7 can be re-organized into three integrals summed together, $M(t_0) = M_1 + M_2 + M_3$, where M_1, M_2 and M_3 can be calculated separately:

$$M_1 = \int_{\infty}^{\infty} -\delta y_0^2 dt = \int_{\infty}^{\infty} -2\delta \left(\frac{2}{e^t + e^{-t}}\right)^2 \left(\frac{1-e^{-2t}}{1+e^{-2t}}\right)^2 dt = -2\delta \cdot \frac{2}{3} \tag{5.8}$$

$$\begin{aligned} M_2 &= \int_{\infty}^{\infty} \gamma y_0 cos\omega(t+t_0)dt = \int_{\infty}^{\infty} \mp\sqrt{2}\gamma \left(\frac{2}{e^t + e^{-t}}\right) \left(\frac{1-e^{-2t}}{1+e^{-2t}}\right) cos\omega(t+t_0)dt \\ &= \sqrt{2}\gamma \left(\frac{1}{2} i\pi\omega Sech(\pi\omega/2)(e^{it_0\omega} - e^{-it_0\omega})\right) \\ &= \pm\sqrt{2}\gamma\pi\omega Sech(\pi\omega/2) sin(t_0\omega) \end{aligned} \tag{5.9}$$

$$\begin{aligned} M_3 &= \int_{\infty}^{\infty} A y_0 cos\omega_p(t+t_0) x_0 dt \\ &= \int_{\infty}^{\infty} \sqrt{2}A \left(\frac{2}{e^t + e^{-t}}\right) \left(\frac{1-e^{-2t}}{1+e^{-2t}}\right) cos\omega_p(t+t_0) \cdot \sqrt{2} \left(\frac{2}{e^t + e^{-t}}\right) dt \\ &= -4A \left(\frac{1}{8} i\pi\omega_p^2 Csch(\pi\omega_p/2)\right) \\ &= A\pi\omega_p^2 Csch(\pi\omega_p/2) sin(t_0\omega_p) \end{aligned} \tag{5.10}$$

Based on the Eqs 5.7, 5.8, 5.9 and 5.10, the Melnikov function can be given explicitly:

$$M(t_0) = \frac{4}{3}\delta \pm \sqrt{2}\gamma\pi\omega Sech\left(\frac{\pi\omega}{2}\right) sin(\omega t_0) + A\pi\omega_p^2 Csch\left(\frac{\pi\omega_p}{2}\right) sin(\omega_p t_0) \tag{5.11}$$

According to the Melnikov analysis, the first variation of distance function between stable and unstable manifolds of homoclinic orbits is proportional to Melnikov function. When chaotic motion arises in the system, there should exist simple zeros in the Melnikov function of Eq. 5.11, which implies the stable and unstable manifolds intersect transversely with each other. In addition, it is only a necessary condition that when Melnikov function has real root t_0 the system can possibly be at the chaotic state. By employing the Melnikov method, the understanding of the chaos controllability when $\omega_p \approx 1$, as shown in Fig. 5.4, has been further discussed. Numerically, the Eq. 5.11 is solved for t_0 ranging from 0 to

1×10^6 with other parameters remain exactly same as in previous calculations. The case when ω_p is slightly bigger and smaller than 1 have been firstly calculated, as shown in Figs. 5.7 ($\omega_p = 1.0001$) and 5.8 ($\omega_p = 0.9999$), respectively. As we can see from Fig. 5.7 and

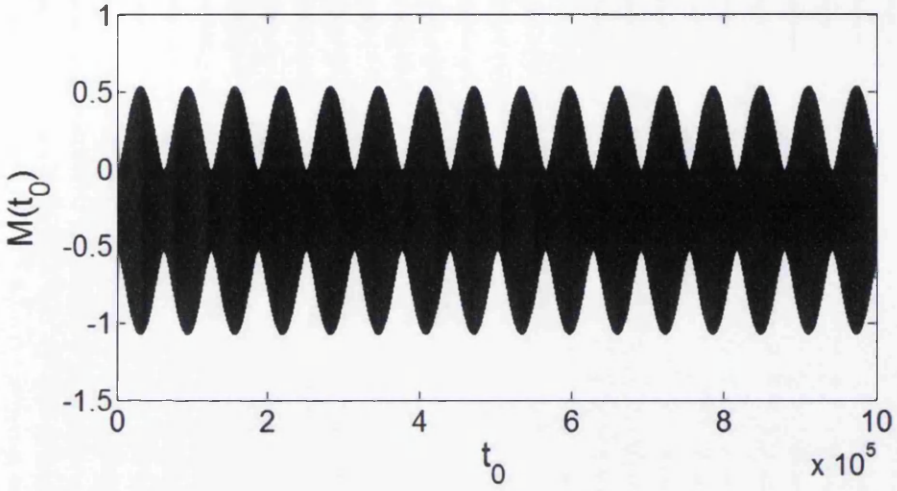

Fig. 5.7 Calculated $M(t_0)$ for $\omega_p = 1.0001\omega$.

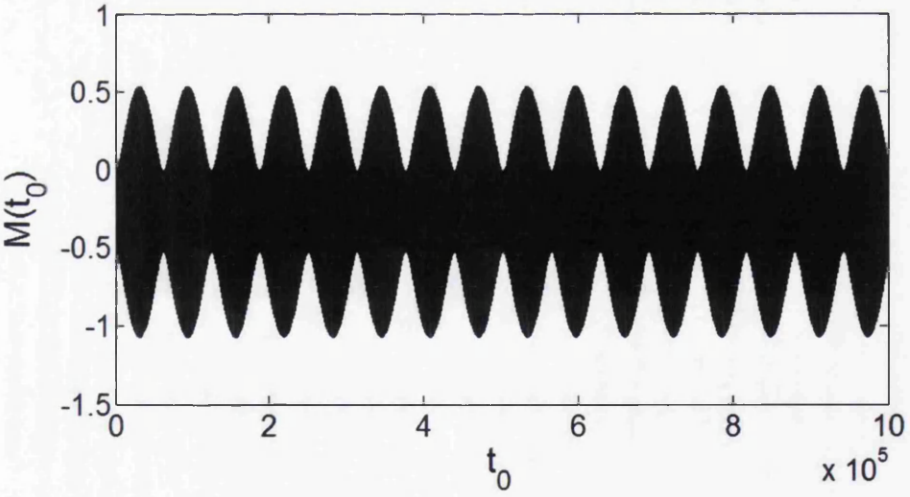

Fig. 5.8 Calculated $M(t_0)$ for $\omega_p = 0.9999\omega$.

Fig. 5.8, there are many points where $M(t_0) = 0$, which indicates that the system can exhibit chaotic behaviour. This results can also be put in the way that there is no chaos controlling effect of the parametric driver when $\omega_p = 1.0001$ and $\omega_p = 0.9999$. However, when ω_p is set to 1 and with all other parameters unchanged, the $M(t_0)$ becomes to be without 0 solution as shown in Fig. 5.9, which indicates that the system will not reach chaotic state,

hence it has been completed suppressed. The result of the Melnikov analysis agrees well with the simulation in the Fig. 5.4, where the chaos controllability when $\omega_p = 1$ has been shown. Here, the ratio of pump frequency change has been defined as $r_\omega = (\omega_p - \omega)/\omega$.

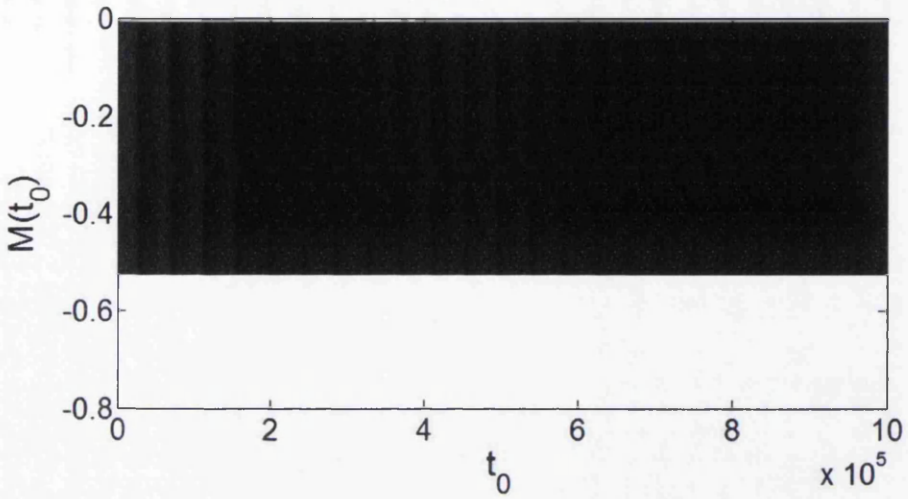

Fig. 5.9 Calculated $M(t_0)$ for $\omega_p = \omega$.

It is noted that Eq. 5.6 has two forms ($\pm$); only minus sign is used in the calculation, as the equation with plus sign gives impractical results. To demonstrate the sensitivity of the parametric chaos control, calculations are conducted for time section t_0, where the $M(t_0)$ is zero versus the ratio of pump frequency change. It is seen from Fig. 5.10 that the relationship between logarithmic t_0 and logarithmic r_ω is almost linear. This indicates that as the pump frequency change gets smaller, the system takes longer time to return to chaotic state. When the pump frequency is exactly same as the frequency of the external exciting force, the chaos is completed suppressed. However, the case of ω_p being exactly same as ω is very difficult to achieve in practice, hence strictly speaking, the suppression cannot hold for long time in reality. The closer the ω_p to the ω, the longer time the suppression holds.

5.2.2 MLEs with Varied Pump Amplitude

Finally, MLEs have been calculated, and results shown in Fig. 5.10 indicates that less impact to the Duffing oscillator when the parametric pump amplitude is small, and the impact becomes more significant as the amplitude increases. This is reasonable as the larger the amplitude of the parametric perturbation, the more significant influence it imposes to the Duffing system.

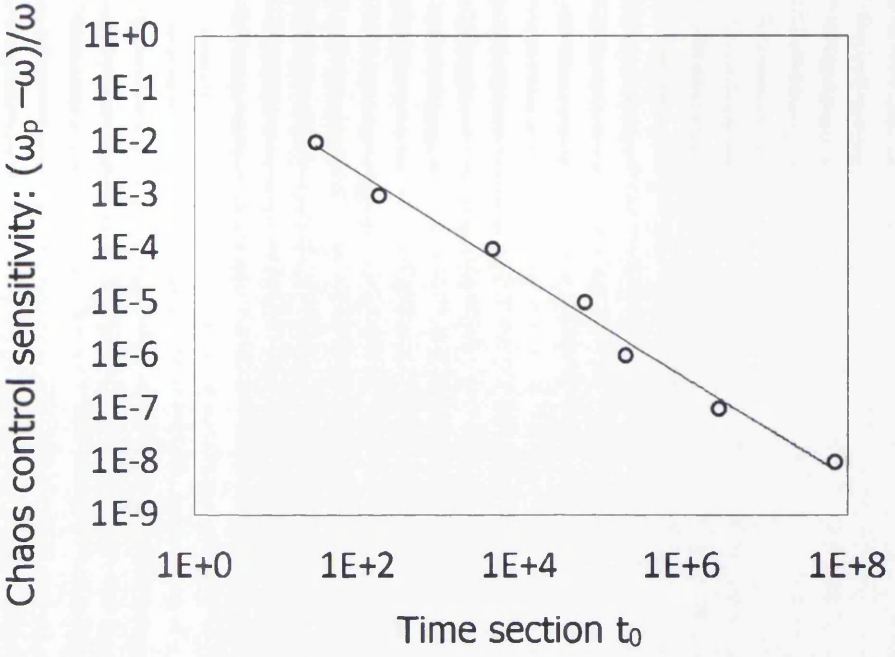

Fig. 5.10 Chaos control sensitivity for ω_p near ω.Horizontal axis is the time section t_0 for the first $M(t_0) = 0$, and vertical axis is the difference between the pump frequency and the external driving frequency.

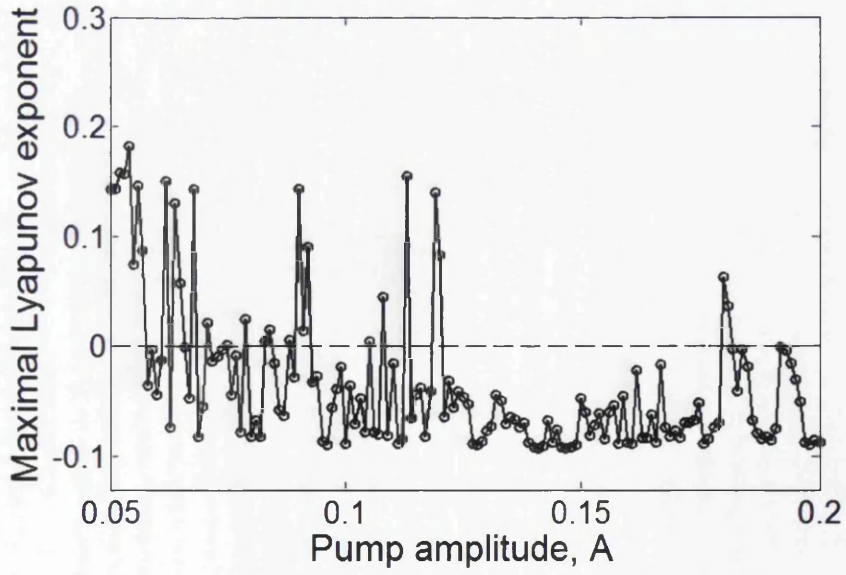

Fig. 5.11 Calculated MLEs of the Duffing system (negative spring constant) with a parametric pump with varying amplitude A.

5.3 Duffing Resonator with Positive Spring Constant

The experimental set-up shown in Fig. 5.1 (b) was fabricated by R.B.Karabalin at al. [124], where the suspended doubly clamped beam is directly driven by the electrostatic force and parametrically driven by two supported pump beams, and the parametric driving is realized through the magnetic force that is induced due to the current flowing in the supported beams while the whole structure is exposed in a magnetic field. The generated pumping force stretches or compresses the doubly clamped resonating beam along its longitude, adjusting its linear spring constant. The equation of describing the in-plane motion of the parametric driven doubly clamped resonator can be expressed as:

$$\ddot{z}(t) + (\omega_0^2 + k_p' cos w_p \omega_0 t) z(t) + \delta \dot{z}(t) + \alpha z^3(t) = 2F_0 cos(w_d \omega_0 t + \phi), \tag{5.12}$$

, which has been employed in previous studies [124], where $\delta = -f_1/(\rho S)$, $\alpha = 8E\pi^4/(9\rho L^4)$, $k_p' = k_p 4\pi^2/(3L)$, $F_0 = \sqrt{2/3} f_0/(\rho S)$, $\omega_0 = \sqrt{16\pi^4 EI/(3\rho S L^4)}$, $\omega_p = w_p \omega_0$ and $\omega_d = w_d \omega_0$. S and L are the cross-sectional area and length of the doubly clamped beam. E is the Young's modulus, and $I = wd^3/12$ is the moment of inertia of the beam's cross-section area. w and d are width and thickness, respectively. ρ is the mass density, ω_p is the pump frequency, and k_p is the pump amplitude which can be changed via modulating magnetic field B or the current applied to the pump beams. $f_0 = \pi \varepsilon_0 V_{dc} V_{ac}/(h(ln(4h/d)^2))$ and $f_1 = -\pi P T_k/4 v_T$, where the electrical potential is $V = V_{dc} + V_{ac} cos(\omega_d t + \phi)$, in which V_{dc} and V_{ac} are dc and ac components, and ω_d as the drive frequency. h is the gap between the beam and the electrode. In the following, the gap will be assumed to be constant as the vibration of resonator is very small. P and T_k are the air pressure and temperature, respectively, $v_T = \sqrt{k_B T_k/m}$ is the air molecule velocity at T_k, k_B is the Boltzmann constant. In the calculation process for deriving Eq. 5.12, the Galerkin's method has been used, which assumes that the displacement in the z direction is $z(t) \times \psi(x)$, $z(t)$ and $\psi(x)$ are the time-dependent amplitude and eigenmode deflection, respectively. $\psi(x) = (2/3)^{1/2}[1 - cos(2\pi x/L)]$ has been assumed, and the it satisfies the boundary conditions $\varphi(0) = \varphi(L) = \varphi''(0) = \varphi''(L) = 0$. Before conducting the calculation of the Eq. 5.12, it can be re-written as:

$$\begin{aligned} \dot{z_1} &= z_2 \\ \dot{z_2} &= -((\omega_0^2 + k_p' cos w_p \omega_0 t)) z_1(t) - \delta z_2(t) - \alpha z_1^3(t) + 2F_0 cos(w_d \omega_0 t + \phi), \end{aligned} \tag{5.13}$$

Based on the Eq. 5.13, the parametric amplification of the resonator in the linear regime with the driving frequency sweeping in the range of $0.95 < w_d > 1.052$ has been firstly studied. The driving voltage V is set to be low, i.e., $V_{dc} = 100$ mV and $V_{ac} = 10$ mV. The parametric

driving frequency, phase and amplitude are taken as $w_p = 2$, $\phi = \pi/2$ and $k_p^{'} = 0.005\omega_0^2$, respectively. Other parameters are taken as $d = 100$ nm, $w = 30$ nm, $L = 3\mu$m, $\rho = 2332$ kg/m^3, $E = 169$ Gpa, $T_k = 300$ K, $P = 0.05$ atm, $h = 1$ μm, and $m = 5.6 \times 10^{-26}$ kg. The result has been plotted in Fig. 5.12, where it is seen that the amplitude of the resonator has increased to 2.88×10^{-10} m with the pump on compared with the case with pump off. The amplitude increase under different driving phase ϕ and w_p has also been investigated, and the result has been plotted in Fig. 5.13. It is seen that in Fig. 5.13 the biggest amplitude of the resonator appeared when $\phi = \pi/2$ and $w_p = 2$, which are consistent with the result reported before [124]. The system will be vibrating in nonlinear regime if higher external

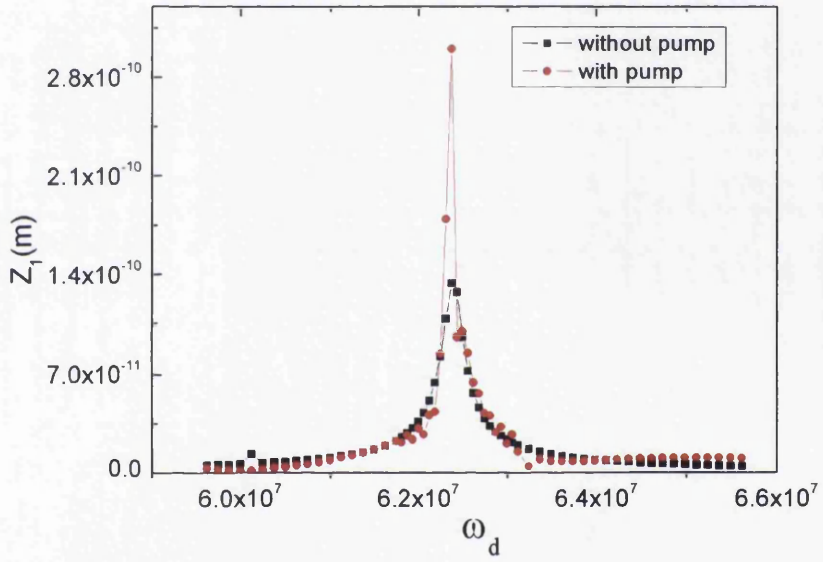

Fig. 5.12 Calculated parametric pumping effect to a Duffing system (positive spring constant) in periodic region. The results are consistent with experimental results in Ref.16 Displacement vs parametric frequency.

driving voltage V is applied. Specifically, the motion of the beam would be exhibiting in a non-regular pattern: transient chaotic state, in which the arisen chaos behaviour can not last for a long time. It is found that the system without pumping ($k_p^{'} = 0$) is in the transient chaotic state before $T = 15000$ (T is a non-dimensional time series, $T = \omega_0 t$) and then the chaotic state is transformed into periodic state when $T = 1500000$, taking the same parameters as above except the voltage V_{dc} and V_{ac} are set to 20 V and 12 V, respectively.

For investigating the chaos controlling effect of the pump, the $k_p^{'}$ has been set to be $0.005\omega_0^2$, and the bifurcation diagram of the system based on the Eq. 5.13 has been plotted in Fig. 5.14. It can be seen that at some certain pump frequencies the transient chaos have

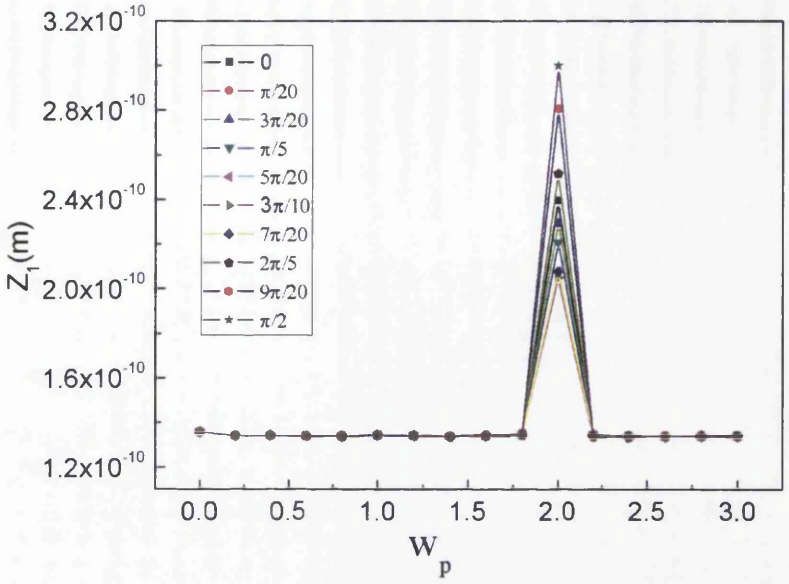

Fig. 5.13 Displacement vs parametric amplitude of Eq. 5.14.

been controlled into periodic states, as indicated by the blue box. However, keeping all the parameters unchanged except $k_p^{'} = 0$ the bifurcation diagram plotted in Fig. 5.15 shows the system is still in transient chaos state. The MLE of the system has been calculated for three evolution time intervals with w_p varying in [0.8 1.6] while keeping other parameters as same as above. The results have been plotted in Fig. 5.16, where it can be seen that the system is mostly chaotic in the first time evolution interval $T = 50000$ as nearly all the MLE are positive, while there are more negative MLE points appeared when $T = 100000$ and much more negative points appeared when T is increased to 1500000, which means the transient chaos in the parametric driving system will enter periodic state eventually but with less time. It should be mentioned that the relation $z_1^{'} = z/h$ and $z_2^{'} = dz_1^{'}/dt$ for normalization has been used in the calculation of MLE. Furthermore, the impact of the $k_p^{'}$ with respect to the phase shape of the system has been explored ($w_p = 2$), the results plotted in Fig. 5.17 shows that the $k_p^{'}$ has the effect to modulate the phase shape. With the increasing of $k_p^{'}$, the number of intersections in the periodic trajectory of the system increases, leading to increased number of periodic states.

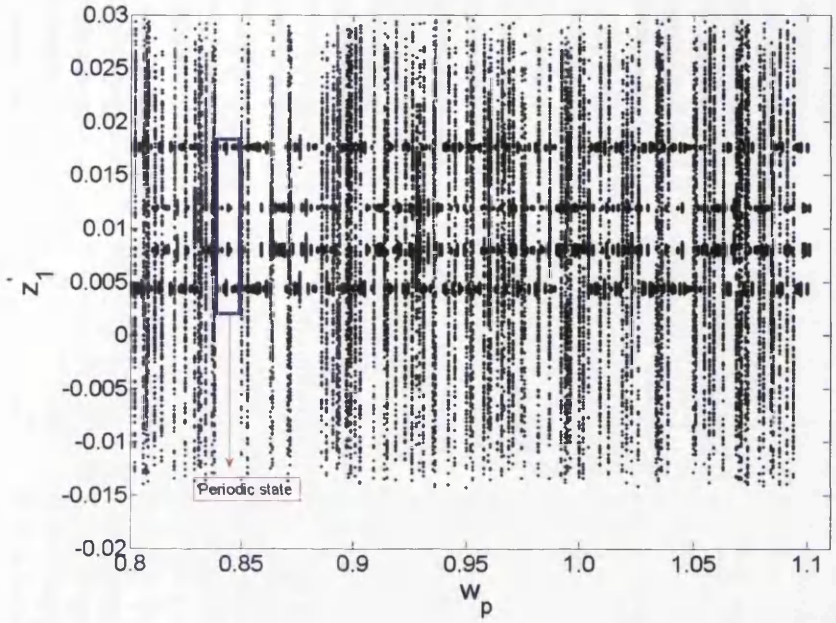

Fig. 5.14 Bifurcation diagram of displacement of the Duffing oscillator with positive spring constant when varying w_p in [0.8,1.1] and $k_p = 0.005w_0$.

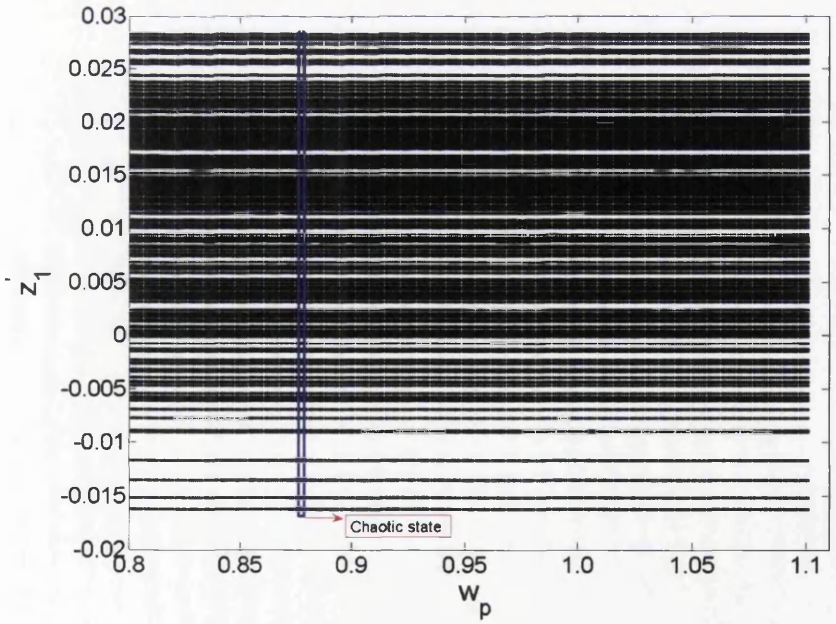

Fig. 5.15 Bifurcation diagram of displacement of the Duffing oscillator with positive spring constant when varying w_p in [0.8,1.1] and $k_p = 0$.

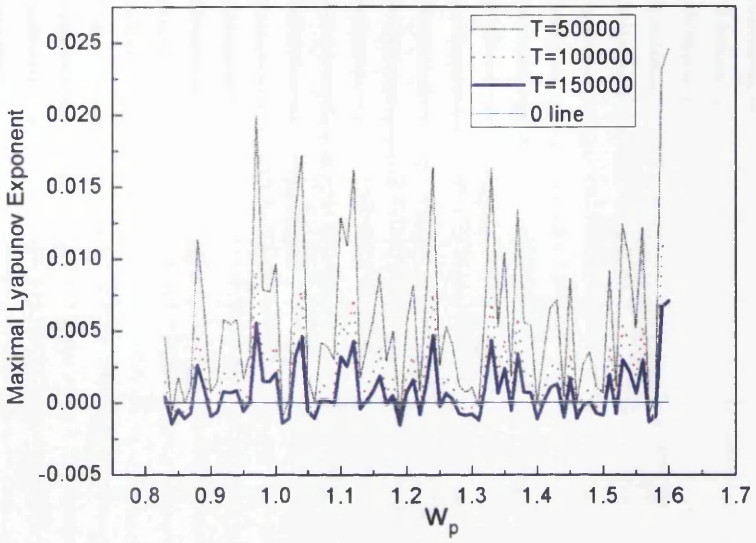

Fig. 5.16 MLE of the Duffing oscillator (positive spring constant) with varying $w_p$in [0.8, 1.6]

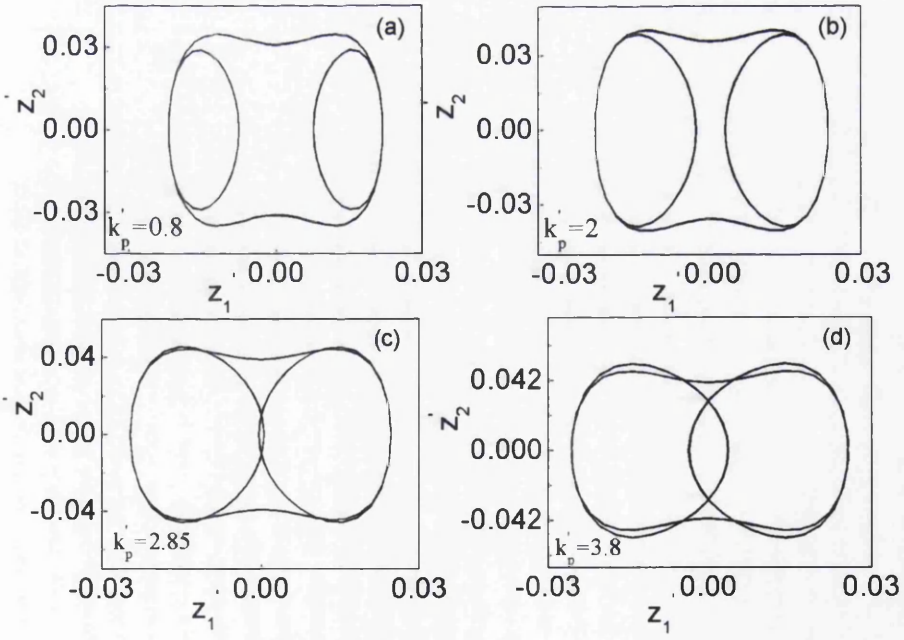

Fig. 5.17 Calculated phase portraits of Duffing oscillator (positive spring constant) when $w_p = 2$.

5.4 Conclusion Remarks

To conclude, Duffing resonators with negative and positive spring constants driven by parametric pump were investigated to unveil the controllability of chaotic vibrations. Calculations were conducted to the two types of dynamic systems using established methods such as Melnikov's method, MLE, and Galerkin's method. All calculations used parameters from previous experiments except for varying driving conditions. For the negative spring constant system, a precise reconfigurability ($\pm 0.0001\omega$) has been demonstrated at the frequency point $\omega_p = \omega$. Calculation also shows that this reconfigurability can be further increased by extending t_0. Nevertheless, the time period during which the chaos being suppressed can be very long if the mismatch is sufficient small. The impact due to the amplitude of the parametric pump has also been investigated. It is shown that as the amplitude increases, the impact becomes greater. For the positive spring constant Duffing system, transient chaos has been demonstrated, which can be controlled using the parametric pump. Varying parametric pump frequency and amplitude, it was found that the transient chaos enter the periodic state with less time than the system without parametric driving. This work theoretically validated dynamic behaviours of two typical systems, stable (positive spring constant) and unstable (negative spring constant). Results of this work will serve a future reference for design of the parametric driven Duffing resonators.

Chapter 6

Novel Mass Sensors Based on Macro-Nano-mechanical Transistor

6.1 Backgroud

6.1.1 Shuttle Mechanism

With the aim of gaining an insight into the Nano-mechanical Transistor (NMT) and large scale electromechanical transistor (LSEMT), it is the best to start with the quantum shuttle mechanism that was first theoretically proposed by Gorelik et al. [131] in 1998. The shuttle mechanism describes the self-oscillation regime of a metallic grains or molecular clusters with a typical size of 1–5 nm embedding between two electrodes, where the metallic grains or molecular clusters are behaving just like the island in a single electron transistor (SET) [132] but its position are not necessarily fixed, and instead they are elastically interlinked with the electrodes. Under a bias applied to the electrodes, the "island" is assumed to be significantly deformed due to the combination effect of Coulomb blockade [132] and the electrostatic force associated with the induced electrical field. For a sufficiently large bias voltage, the "island" can evolve into a special dynamical stage, known as the shuttle mechanism, in which the "island" is oscillating between two turning points. At the first turning point which is near to the positively biased electrode, the "shuttle" loads $2N$ electrons from the electrode. Then it unload the same number of electrons when it reaches the second turning point that is located close to the negatively biased electrodes. The process of the electron transferring is essentially dominated by the quantum tunnelling under the regime of the Coulomb blockade, and the vibration of the "shuttle" is subjected by the coupling effect between restoring force of itself and the electrostatic force, as illustrated in Fig. 6.1. A current will be arising as the "island" shuttling, and the average current can be calculated easily from the plot shown in

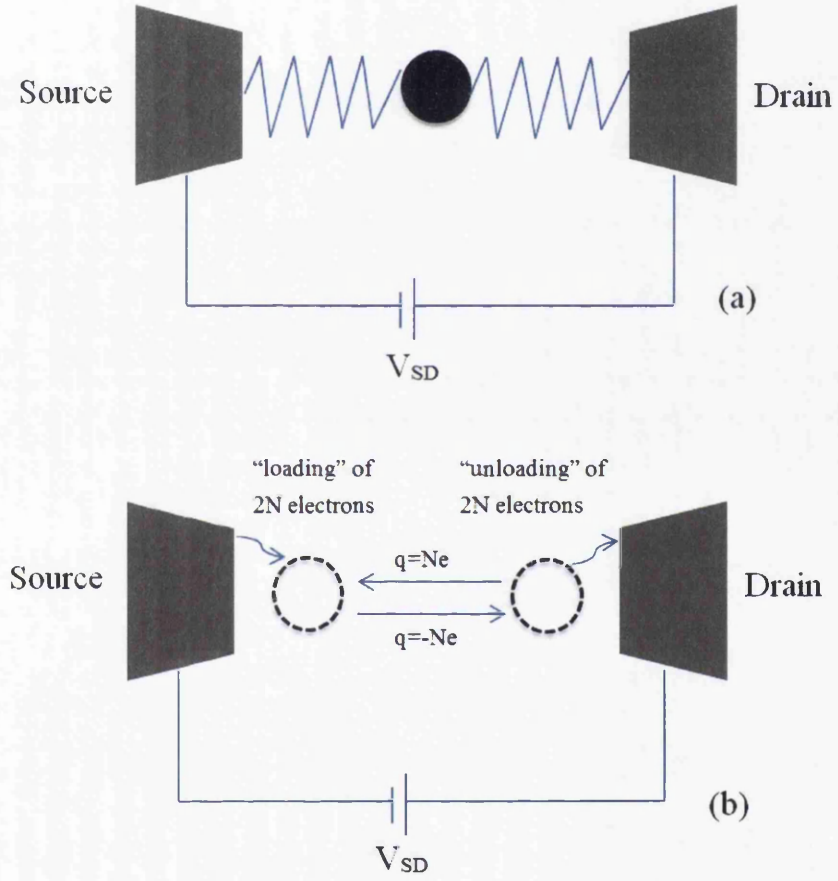

Fig. 6.1 The working principle of the "shuttle". (a) A metallic grain is interlinked with two electrodes and subjected in the electrical field. (b) The working process of the shuttle.

Fig. 6.1. In each circle, there are $2N$ electrons are transported. Thus, the current from the shuttle mechanism can be written as: $I = 2eNf$, where e is the charge of a single electron, and f is the self-oscillation frequency.

Based on the shuttle mechanism of the electron transportation in the nanostructures, lots of work both in theory and experiments have been conducted. A new approach were developed in [133] for investigating the shuttle instability in self-assembled Coulomb blockade nanostructures when the tunnel barriers is high. The coupling between the electronic and mechanical degrees of freedom on the nano-scale structure were demonstrated in [134], and its effect on the shuttling of electrons were studied. In the limit of weak electromechanical coupling, the noise spectrum of the single electron shuttle were studied [135]. The response of shuttle when it is driven by time-dependent driving were investigated, and the electrical properties such as rectification, synchronization, of the shuttle were found [136]. A Kondo shuttle device that were driven by electrical and magnetic fields at the same time were analysed in [137]. The synchronization of a single-electron shuttle with the external drive were achieved in [138]. By employing the Kondo shuttling in NEM-SET model, the manifestation of dynamical symmetries in quantum transport was discussed [139]. How the van der Waals force plays its role in shuttle system was investigated in [140]. The ac-gate were found to be important as to the electron transport in a shuttle device [141]. The charge shuttle was proposed to be a nanomechanical rectifier when it is driven by a time-dependent voltage bias and asymmetrically set [142].

Experimentally, nanomechanical devices relies on the shuttled mechanism have also been widely exploit. For example, in [143], the authors have fabricated a silicon nanopillar for being the shuttle island, which can operate at frequency as high as 350-400 MHz, and the current versus different driving frequencies were measured and compared. In [144], a voltage-sustained nanomechanical electron shuttle was realized, where the device was driven by means of ultrasonic waves, and an array of the shuttles were fabricated and proved to be working well. At the room temperature, Coulomb blockade was observed in a coupled nanomechanical pendula, where the nanomechanical pendula were fabricated to be two serially coupled electron shuttles [145]. A shuttle junction was fabricated by Andrity et al in [146] that consisted of a gold nanopartical as the shuttle island and two gold electrodes. The transition process from the perspective of nonlinear dynamics were demonstrated in a coupling electrons shuttles [147].

6.1.2 NMT

The potential application of the shuttle mechanism includes the new generation of nanomechanical electronic devices, such as transistors, very sensitive electrometers, sensors and

logic gates [146]. The design of a NMT is based on the idea that the shuttle island can be fabricated by attaching a metal grain to the nanomechanical beam, as shown in Fig. 6.2. In Fig. 6.2, the nanomechanical beam between the source and drain are playing the role

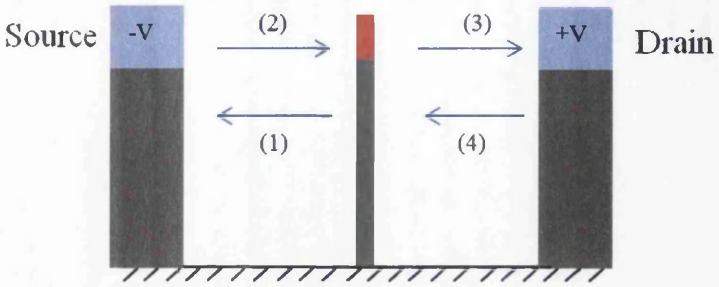

Fig. 6.2 The NMT structure and its working process

same to the shuttle island. Under a proper setting of the bias voltage between source (S) and drain (D), the beam will be oscillating in a limit-cycle regime, as the process described in last section, which includes four phases. As indicated in Fig. 6.2, during the transition phase form (1) to (2) (from (3) to (4)), the mechanical grain attached on the top of the beam will load (unload) $2N$ electrons via quantum tunnelling, and a current that relies on the frequency of the beam is arising. The model in Fig. 6.2 is just a basic configuration of a NMT while there is a multiple-module configuration that can be used to realize current amplification has been proposed [148], as shown in Fig. 6.3. As shown in Fig. 6.3, an array

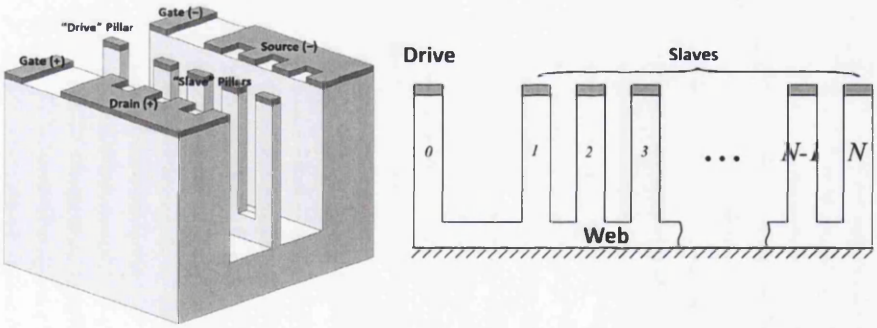

Fig. 6.3 Blicks multiple-module configuration. Architecture referred to United States Patent 7414437B1 —2008.

of nanomechanical beams have been fabricated, and each beam with the facing electrodes are forming a shuttle system, as the one shown in Fig. 6.2. One of the beams functions as the drive pillar labelled "0" and other beams are called slave pillars which are labelled by 1,2,3...N. When the drive pillar starts vibrating due to the driving from the gate voltage, the

slave pillars would be followed to oscillate subsequently because of the coupling effect with the drive pillar. Thus, by modulating the gate voltage, the current flowing through the slave pillars can be controlled so that it can be seen an application current. This is the working principle of the multiple-module NMT.

In this chapter, two mass sensors that are based on the shuttle mechanism and NMT model will be designed. The first one is in nano-scale that includes two coupled nano-beams, with one of them is functioning as the shuttle and the other one as the sensing beam. The whole structure will be verified of working in a self-oscillation regime. The second mass sensor is designed in large-scale with the aim to solve the practical concerns such as the issues in fabrication. The principles of mass sensing of the both will be theoretically explained by the end of the chapter.

6.2 Model Design

As depicted in Fig. 6.4 (a), the device consists of two mechanically coupled cantilevers. Each cantilever has an end that can be vibrating freely, and the other ends are connected by a rectangular cuboid whose bottom surface is anchored. One of the cantilevers is called active beam, to both sides of which there are two mechanically fixed electrodes, acting electrically as source S and drain D. At the free end of the active cantilever, a tunnel junction is fabricated with G and B as the two terminals. Under a DC voltage applied to source and drain, self-excited oscillation of the cantilever along y-axis occurs which drives the intimate cantilever (termed as the passive cantilever) to vibrate through the coupling of the cuboid in y-axis as well. Small amount of mass landed on the passive cantilever causes mechanical properties change, in turn affects the dynamic performance of the active cantilever, which is diagnosed by the tunnelling current of the NMT. To summarize it, the electrical current or charge transport of the NMT based mass sensor varies as a tiny amount of mass attached to the passive cantilever. This device can be represented by a equivalent circuit plotted in Fig. 6.4 (b), where C_{GS} and G_{GS} are the capacitance and conductance between terminal G and terminal S, respectively. Likewise, C_{GD} and G_{GD} represent the same physical quantities between terminal G and terminal D, and the implication of the index applies to C_{GB} and G_{GB} too. Both the C_{GS} and C_{DG} are functions of gaps between S and G, G and D, expressed as: $C_{DG,GS} = C^0_{DG,GS}(g/(g \pm 2y_1))$, where $C^0_{DG,GS}$ is the initial capacitances, g is the initial gap between the S and D and y_1 is the tip displacement of the active cantilever. It is assumed that the initial position of the active cantilever is in the middle of the S and D. Q_G is the charge carried by the terminal G that varies with the y_1. G_{GS} and G_{DG} are also functions of the tip displacement, which is expressed as: $G_{DG,GS} = G^0_{DG,GS}e^{(\mp y_1/\lambda)}$, where $G^0_{DG,GS}$

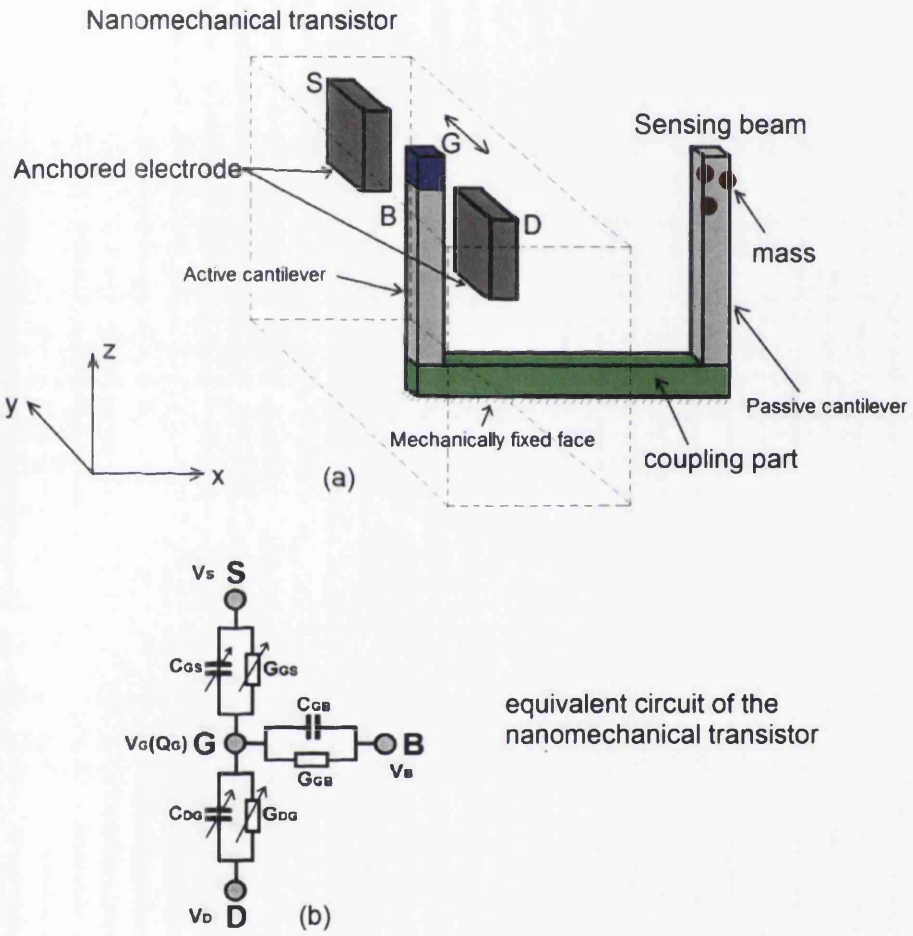

Fig. 6.4 Schematic graph of the NMT mass sensor (a); equivalent circuit of the NMT (b).

is the initial conductance, λ is the tunnelling length defined as $\lambda \approx \left(\frac{2\sqrt{2m_e\varphi}}{\hbar}\right)^{-1}$. In this expression, the m_e is the mass of a single electron, $\hbar$ is the Planck constant divided by 2π, and φ is the work function of the electrode. C_{GB} and G_{GB} are assumed to be constants. The specific geometrical dimensions of the cantilevers will be given in the next section. The active cantilever has the length L_1, width w_1, and thickness d_1. The passive cantilever has the length L_2, width w_2, and thickness d_2. In terms of mechanical aspect, the behaviour of the mechanically coupled device is governed by the coupled motion equation:

$$\begin{aligned} \ddot{y}_1 + \frac{\beta}{m_1}\dot{y}_1 + \omega_1^2 y_1 + \frac{k_{12}(y_1 - y_2)}{m_1} &= \frac{V_D - V_S}{g m_1} Q_G \\ \ddot{y}_2 + \frac{\beta}{m_2}\dot{y}_2 + \omega_2^2 y_2 + \frac{k_{12}(y_2 - y_1)}{m_2} &= 0 \end{aligned} \tag{6.1}$$

where y_1 is the tip displacement of the active cantilever, and y_2 is the tip displacement of the passive cantilever. k_{12} is the coupling coefficient of the two cantilevers. The two cantilevers are in the same environment so that they have the same damping coefficient β. ω_1 and ω_2 are resonant frequencies of the two cantilevers, and they can be obtained by: $\omega_{1,2} = B/(L_{1,2})^2\sqrt{EI_m/\rho A}$, ($B = 1.875$). The two cantilevers are assumed to be made of same material and have same cross section area ($w_1 = w_2$, $d_1 = d_2$). E, ρ and I_m are Young's modulus, moment of inertia and density of the material, respectively, which are same to two cantilevers. V_D, V_S, and V_B are electrical potentials applied on the terminals D, S and B. $m_{1,2}$ is the effective mass of the cantilever. In order to solve the Eq. 6.1, the dynamical equation for describing Q_G need to be firstly derived. It is easy to obtain the expression for Q_G from the equivalent circuit, in which it is seen that charge variation at terminal G: dQ_G/dt, is the sum of electrical currents from other three terminals [12], and it is given by:

$$\dot{Q}_G = V_D G_{DG}^0 e^{-y_1/\lambda} + V_S G_{GS}^0 e^{y_1/\lambda} + V_B G_{GB} - V_G(Q_G) G_\Sigma \tag{6.2}$$

where

$$V_G(Q_G) = \frac{Q_G + V_D C_{DG} + V_S C_{GS} + V_B C_{GB}}{C_\Sigma} \tag{6.3}$$

and

$$\begin{aligned} C_\Sigma &= C_{DG} + C_{GS} + C_{GB} \\ G_\Sigma &= G_{DG}^0 e^{-y_1/\lambda} + G_{GS}^0 e^{y_1/\lambda} + G_{GB} \end{aligned} \tag{6.4}$$

The normalization of the equation 5.1 can be made by using the relation: $y_{1,2} = u_{1,2}\lambda$, and then re-arranging the equation by introducing the relations: $\dot{u_{1,2}} = v_{1,2}$, it arrives:

$$\begin{aligned}
\dot{u_1} &= v_1 \\
\dot{v_1} &= -\frac{\beta}{m_1}v_1 - \omega_1^2 u_1 - \frac{k_{12}(u_1 - u_2)}{m_1} + \frac{V_D - V_S}{g m_1 \lambda} Q_G \\
\dot{u_2} &= v_2 \\
\dot{v_2} &= -\frac{\beta}{m_2}v_2 - \omega_2^2 u_2 - \frac{k_{12}(u_2 - u_1)}{m_2} \\
\dot{Q}_G &= V_D G_{DG}^0 e^{-u_1} + V_S G_{GS}^0 e^{u_1} + V_B G_{GB} - V_G(Q_G) G_\Sigma(u_1)
\end{aligned} \tag{6.5}$$

To simulate the system and model the sensing effect, it is needed to solve the Eq. 6.5 numerically to obtain the equivalent deflection $u_{1,2}$, gate charge Q_G, and electrical current I_{DG} and I_{GS} under various potentials on D, S and B. Electrical currents I_{DG} from D to G , I_{BG} from B to G, and I_{SG} from S to G can be obtained by $I_{DG,BG,SG} = (V_{D,B,S} - V_G)G_{DG,GS,GB}$. Then the relationship between electrical current of the NMT and the added mass on the passive cantilever will be derived, which is described in the next section.

6.3 Numerical Simulation

The simulation of the Eq. 6.5 has been conducted by taking the parameters as follows: $g = 40$ nm, $\rho = 2329$ Kg/m^3, $E = 140$ Gpa, $m_1 = m_2 = 4.52$ zg. Environment temperature is 300 K and air pressure is 1×10^5. The initial conductance between G and D: G_{DG}^0 and initial conductance between G and S: G_{GS}^0 are taken the same as 1×10^{-10} S, and conductance between G and B G_{GB} is 1.67×10^{-8} S. Initial capacitance between D and G: C_{DG}^0 is 1×10^{-18} F, initial capacitance between G and S: C_{GS}^0 is 1×10^{-18} F, and capacitance between G and G: C_{GB}^0 is 1×10^{-18} F. The voltage applied on D and S are 0.15 V and -0.15 V, respectively, and $V_B = 6$ V. Dimensions of two cantilevers are: $L_1 = L_2 = 80$ nm, $w_1 = d_1 = w_2 = d_2 = 10$ nm. The coupling coefficient k_{12} is taken as 0.02 N/m. Derived from the numerical calculation, the relations $u_{1,2}$ versus time series t, Q_G versus t and electrical currents $I_a = I_{DG} + I_{SG}$ versus t have been plotted in Fig. 6.5, where it is seen that the shuttling phenomenon occurs, and the transported electrons are around 60 per circle of motion of the active cantilever. The two cantilevers are both vibrating in linear regime with nearly the same amplitude but opposite phase as shown in Fig. 6.5 (a), and they have the same resonant frequencies, which is 12.29 GHz, because of the identical dimensions. Furthermore, the relations between the added mass on passive cantilever and I_a has been

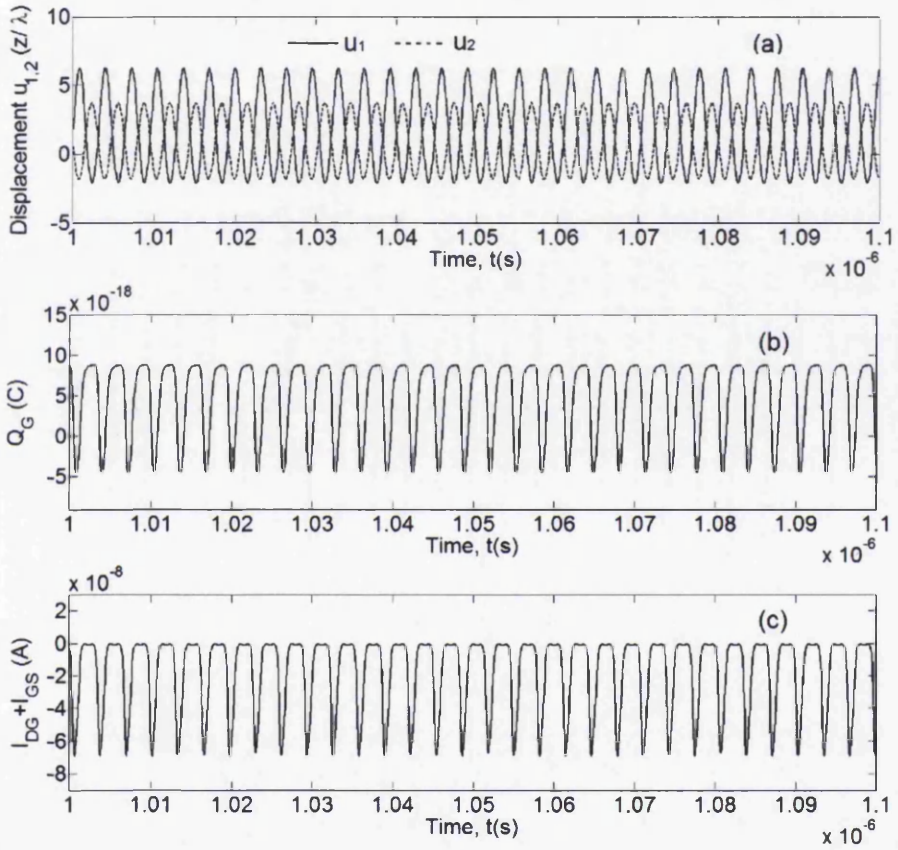

Fig. 6.5 Calculated relationships of $u_{1,2}$ versus time series t, Q_G versus t, electrical currents $I_{DG} + I_{SG}$ versus t.

investigated, and the result is plotted in Fig. 6.6. It is shown that when the added mass m_a increases from 0 to 0.27 zg (0 to 6/100 of the $m_{1,2}$), I_a increases from around 0.11 μA to 0.15 μA, and the amplitude of passive cantilever reduces from around 17.1 to 8.2. The current

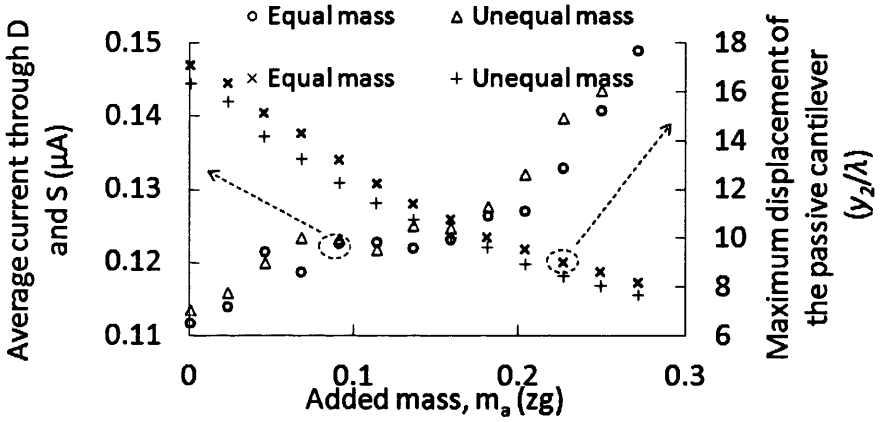

Fig. 6.6 Simulated relation of added mass m_a versus average current through D and S; and maximum non-dimensionalized displacement of the passive cantilever.

increase in the NMT is due to the increasing amplitude of the active beam by adding mass on the passive beam. This phenomenon can be explained by a previously established mode localization theory [149]. The theory elucidates that a small perturbation (added mass) to one of weakly coupled beams leads to vibrational energy localized to the other, leading to increased amplitude. This sensing mechanism has been proven to be much more sensitive than the change of the resonant frequency. The change of amplitude in the active beam is linearly proportional to the added mass subject to the condition that the effect of added mass is much smaller than the coupling factor. The threshold voltage at which the shuttling phenomenon occurs has also been calculated. The applied voltage on D and S has to reach the point where $V_D - V_S \approx 0.13$ V so that the self-oscillating starts, as shown in Fig. 6.7. In the practical fabrication, it is quite difficult to control that the mass of the active cantilever is equal to that of passive cantilever ($m_1 = m_2$), especially in nano-scale. The case when the two cantilevers have a initial difference of the effective mass ($m_2 = 1.005m_1$) has been calculated, and the result is shown in Fig. 6.6, where similar relations between added mass and I_a with the equal mass is observed.

6.4 Model of LSENT

In the last section, a novel mass sensor that is based on the nanomechanical transistor has been described. The device can work in self-oscillating regime, in which the electrons is

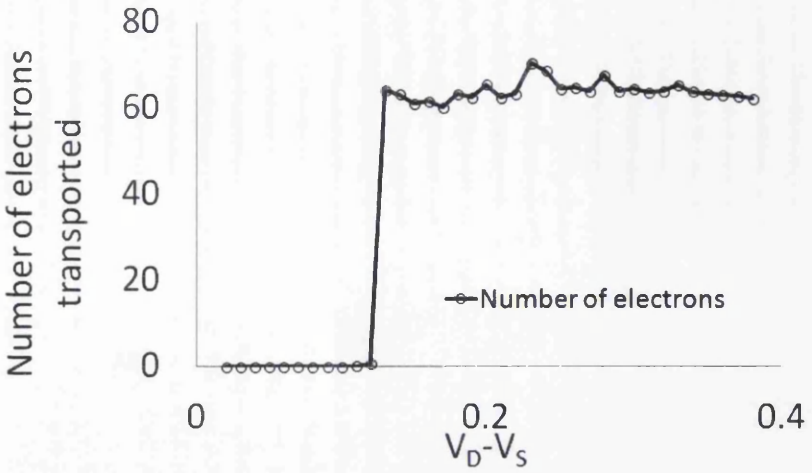

Fig. 6.7 Simulated threshold voltage necessary to achieve self-excitation of the cantilevers.

shuttled from source and drain, and the electrostatic force, as the only driving for the beam, depends on the net charge brought by the transported electrons. The dynamics that involves mechanical motion and the electrons transportation is a self-consistent problem. But to achieve this in reality, it is undoubtedly a challenging task much less in nano-scale. In order to design a more practical and feasible one, a large scale electromechanical transistor has been proposed in this section, which is not relying on the self-oscillating, but instead driven by an external force, and the electrostatic force is so small that it can be ignored in this model. The design has been presented in the Fig. 6.8, where it is seen that the design has a quite similar structure with the one investigated in last section apart from the size. While there are two more electrodes have been designed along the two sides of the active beam. They are called driving electrodes here, which can provide the driving force by forming the adjustable capacitor with the active beam. This driving mechanism has been widely employed in the field of micro-electromechanical systems. Other driving methods such as the piezoelectric and electro-thermal could also be considered. The other different point of the design from the last one is that a pair of needles are employed to realize tunnelling effect with the source and drain. They are fabricated to the two sides of metal bead, facing to the source and drain, respectively. The design in Fig. 6.8 also can be represented by a equivalent circuit, as shown in Fig. 6.8 (b). To verify the feasibility of the device, both theoretical and numerical analysis will be conducted in the following section. A working LSEMT will be demonstrated, and furthermore, the its potential applications in mass sensing will also be explored.

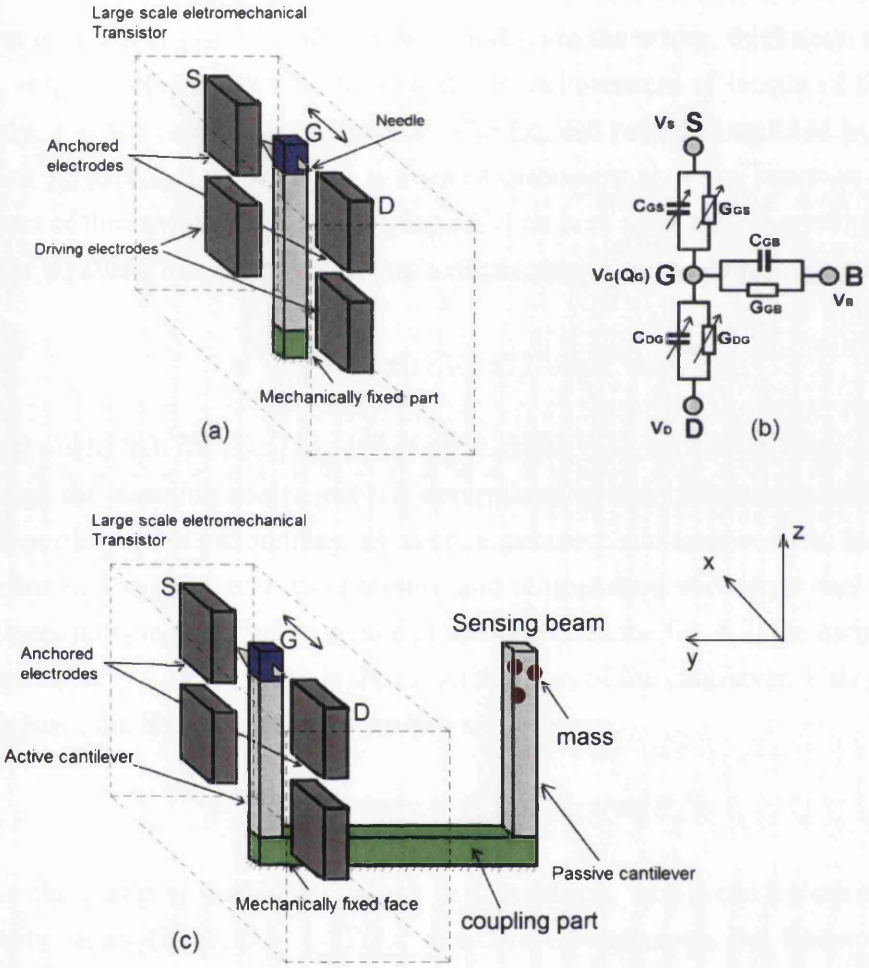

Fig. 6.8 Schematic view of the large scale electromechanical transistor device. (a) schematic of the single device. (b) equivalent circuit for the single transistor device. (c) mass sensor based on the single transistor device (It is noted that the schematic drawings are not to scale.).

6.4.1 Device Construction and Modelling Approach

For a single cantilever beam, its motion can be described by:

$$\rho A\frac{\partial^2 W}{\partial t^2}+EI\frac{\partial^4 W}{\partial s^4}+EI\frac{\partial}{\partial s}\left[\frac{\partial W}{\partial s}\frac{\partial}{\partial s}\left(\frac{\partial W}{\partial s}\frac{\partial^2 W}{\partial s^2}\right)\right]=f \tag{6.6}$$

where the $W(s,t)$ is the displacement of a certain position s on the cantilever in longitudinal direction at a time t. E and $I=wd^3/12$ (w, d and L are the width, thickness, and length of the beam, respectively) are the Young's modulus and moment of inertia of the cantilever, respectively. f is the external driving force. The Eq. 6.6 can be simplified by substituting $W(s,t)$ with $\sum_n \phi_n(s)x_n t$, where $\phi_n(s)$ is a set of orthonormal shape function and x_n is the displacement of the cantilever tip, multiplying $\phi_1(s)$ on both sides and integrating the equation by parts, the equation that describes the tip's displacement of the cantilever can be derived:

$$m\frac{d^2x(t)}{dt^2}+b\dot{x}(t)+kx(t)+k_3x^3=F \tag{6.7}$$

It should be noted that the damping effect represented by term $b\dot{x}$ has been added into the equation, and the damping coefficient b is determined by the surface area of the cantilever and the properties of the surrounding air, such as pressure and temperature. In a very small region enclosing the cantilever, the pressure and temperature variations can be neglected. Hence, a linear damping coefficient is used in the model. In the Eq. 6.7, the natural frequency is given by: $\omega_0=\sqrt{k/m}$, where m is the effective mass of the cantilever. Using the relation $b/k=1/(Q\omega_0)$, the Eq. 6.7 can be re-written as:

$$\ddot{x}+2\beta\omega_0\dot{x}+\omega_0^2x+\omega_0^2k_3x^3/k=\omega_0^2F/k \tag{6.8}$$

where β is the damping coefficient in the new equation, and it can be derived from the given quality factor Q, i.e, $\beta=1/(2Q)$. $k=3EI/L^3$ represents the linear stiffness and $k_3=(24.79EI)/L^5$ represents the Duffing nonlinear coefficient. The $\omega_0=\sqrt{\frac{3EI}{\alpha\rho wdL^4}}$, where $1/\alpha$ is a non-dimensional stiffness enhancement factor, taking the value of 0.24267 in this work. ρ refers to the density of the cantilever. The relation of the tip displacement versus time can be readily solved with Eq. 6.8 providing the force F is defined. F is the electrostatic force, which is obtained by: $F=V_e^2\varepsilon_0\varepsilon_r A/(2(g+x)^2)$, where ε_0 is the permittivity in vacuum, and ε_r is the relative permittivity of the media where the cantilever vibrates. A is the cross sectional area of the cantilever, and g denotes the gap between the side wall of the cantilever and the side wall of the driving electrode. Apart from the mechanical motion part of the beam described, the electronic part of the device will be elaborated as the device works

phenotypically as a standard field effect transistor. It is shown in Fig. 6.8 (a), there are two electrodes mechanically fixed in the vicinity of the cantilever tip forming the source S and drain D of the LSEMT. Unlike the model in nano-scale the tunnelling effect in this model occurs between the needle and electrodes, and the driving force is dominated by the F and the electrostatic force between the source and drain is assumed to be negligible. The motion of the beam determines the gap between needles and S (D), and meanwhile determines the tunnelling effect distance. Therefore, the charge shuttled Q_G is closely related to the motion (tip displacement). For modelling the dynamics of the Q_G, once again a equivalent circuit is used, shown in Fig. 6.8 (b). It has three terminals representing source S, drain D and gate B. Obviously, in between any two terminals, there are equivalent circuit components: conductance and capacitance forming the real and imaginary parts of the impedance. Just like in last section, $G_{DG,GS,GB}$ represent the conductance between the terminals with terminal G, with the same indication applies to the capacitance $C_{DG,GS,GB}$. The metal bead which is responsible for carrying electrons is the centre terminal G, and the dynamics of the Q_G can be expressed as the electrical currents flowing from terminal D, S and B to the G terminal as follows:

$$\dot{Q}_G = V_D G^0_{DG} e^{-x'/\lambda} + V_S G^0_{GS} e^{x'/\lambda} + V_B G_{GB} - V_G(Q_G) G_\Sigma \tag{6.9}$$

where V_D, V_S and V_B are voltages applied on terminals D, S, and B, respectively. $G^0_{DG,GS}$ means the initial value of conductance between terminal D(S) and G, and $C^0_{DG,GS}$ means the initial value of capacitance between terminal D(S) and G. $V_G(Q_G) = (Q_G + V_D C_{DG} + V_S C_{GS} + V_B C_{GB})$, where $C_\Sigma = C_{DG} + C_{GS} + C_{GB} + C_{G0}$. x' is defined as the displacement when the needle approaches the tunnel distance (1 nm in this work) to the D and S, $x' = g_t - (g_o - (l_n \mp x))$, where g_t represents the gap where tunnelling is coming into effect. g_o is the original gap between the tip of the needle and the wall of the electrode D or S, and l_n denotes the length of the needle. $G_\Sigma = G^0_{DG} e^{-x'/\lambda} + G^0_{SG} e^{x'/\lambda} + G_{GB}$, where the λ is the tunnelling length, and has the same expression as in last section. As the dimensions of the cantilever are far larger than those of archetypal NMTs, the displacement is also large, some modifications to Eq. 6.9 have to be made to reflect the microscopic dimensions. The modifications are shown as:

$$\dot{Q} = \begin{cases} V_D G^0_{DG} e^{-x'/\lambda} - G^0_{DG} e^{-x'/\lambda}(Q + V_D C_{DG})/(C_{DG} + C_{G0}) \ldots\ldots\ldots x \leqslant g_t + l_n - g_0 \\ V_S G^0_{GS} e^{-x'/\lambda} - G^0_{GS} e^{-x'/\lambda}(Q + V_S C_{GS})/(C_{GS} + C_{G0}) \ldots\ldots\ldots x \geqslant -g_t - l_n + g_0 \\ 0 \ldots\ldots\ldots g_t + l_n - g_0 < x < -g_t - l_n + g_0 \end{cases} \tag{6.10}$$

In Eq. 6.10, the potential applied on terminal B as well as all related passive parameters are ingored, such as conductance and capacitance. Basically, the Eq. 6.10 is the piecewise function of Eq. 6.9 splitted in three different regions. In the first region, only the conductance and capacitance between G and D are considered as the the relatively large gap causes the G_{GS} and C_{GS} are insignificant when the needle approaching to the terminal D (within 1 nm range). The second region is for the needle approaching to the terminal S, where the C_{DG} and G_{DG} are ignored. The third region is for the needle vibrating out of 1 nm range away from both the D and S, where there is no tunnelling effect and the Q_G remains the same as the nearest value, i.e. $\dot{Q} = 0$. This modelling protocol for the electronic part is applied throughout the following text, and the charge transferred, current voltage $(I-V)$ characteristics of the device due to the mechanical vibration can be obtained by solving Eq. 6.8 and Eq. 6.10. In the next section, comprehensive analysis of the device characteristics such as $I-V$ will be investigated.

6.4.2 Numerical Simulation and Analysis

The parameters with respect to the geometry, material, electric and environment have been chosen carefully for conducting a quantitative study of the model described, which are given in Table 6.1. Firstly, when the device is under a small external driving voltage, i.e., $V_e = 1$ V, the numerical simulation based on Eq. 6.8 and Eq. 6.10 has been conducted, and the result has been plotted in Fig. 6.9. Specifically, the relation between tip displacement and time has been plotted in Fig. 6.9 (a), where it is seen that the cantilever is oscillating periodically (the resonant frequency has been calculated to be 78.69 kHz.), and the peak to peak resonating amplitude is about 20 nm. The shuttled charge Q_G versus time is shown in Fig. 6.9 (b) with $V_D = 7$V,$V_S = -7$ V and $V_B = 0$ V applied, where the charge shuttled in every circle is about 3.4×10^{-17} C and the Q_G is behaving in a squared shaped waveform, which is due to the narrow tunnelling distance compared with the state in which the cantilever vibrates in the long range of nowhere near the side walls of the D or S. In Fig. 6.9 (c), the sum of current I_{DG} and I_{GS} versus time has been plotted, where the overall current displays a waveform containing regular sparks. This is elucidated that the current has the maximum value when the Q_G changes abruptly from negative to positive or vice versa. The average current I_a that is calculated by summing of all the current values through D and S in unit time is 0.267 pA. The results shown in Fig. 6.9 indicates that micrometre sized LSEMT can be achieved using an external periodic driving force.

Furthermore, under different V_e (0.975 V to 1 V), the relations between I_a and ΔV ($\Delta V = V_D - V_S$) has been calculated, as shown in Fig. 6.10 (a). It is obviously to see that I_a is linearly increased with the increasing of ΔV, and the higher V_e the larger slope. This can be

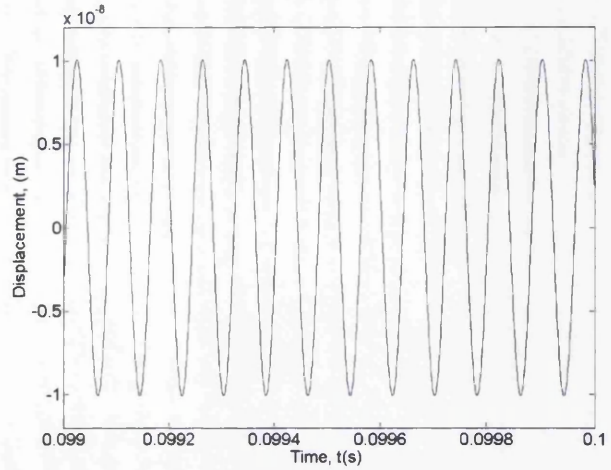

(a) Tip displacement of the cantilever under an external driving force.

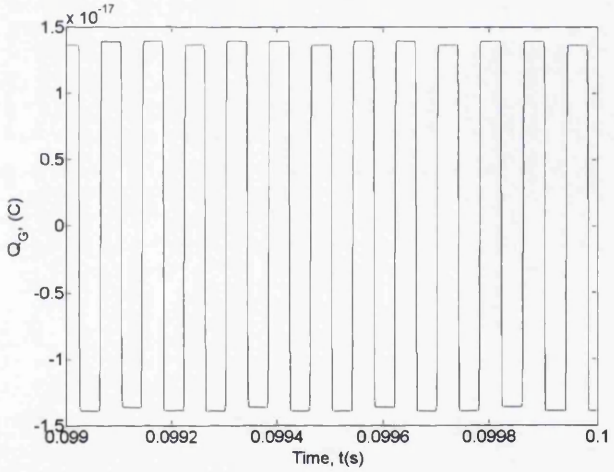

(b) charge value at G terminal when the device is oscillating.

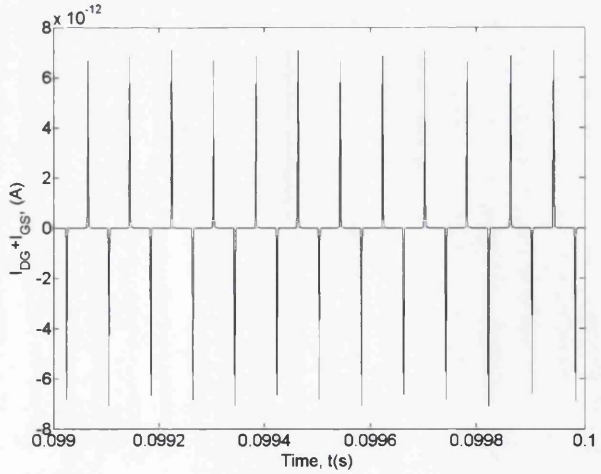

(c) electrical current flowing through terminal D and S.

Fig. 6.9 Simulated electromechanical transistor.

Table 6.1 Parameters used in the numerical simulation for a LSEMT.

Parameter		Value
Geometrical parameters of the cantilever	Length, L	1 mm
	Thickness, d	10 μm
	Width, w	10 μm
	Length of the needles, l_n	1 μm
Material properties of the cantilever	Density of the cantilever, ρ	2329 Kg/m^3
	Young's modulus, E	140 GPa
Electrical parameters	Initial conductance between D and G, G^0_{DG}	1×10^{-20} S
	Initial conductance between S and G, G^0_{GS}	1×10^{-20} S
	Conductance between B and G, G^0_{GB}	0 S
	Initial capacitance between D and G, C^0_{DG}	1×10^{-18} F
	Initial capacitance between G and S, C^0_{GS}	1×10^{-18} F
	Capacitance between G and B, C_{GB}	0 F
	C_{G0}	0 F
Geometrical parameters of the device	g	50 μm
	g_t	1 nm
	g_0	1010.09 nm
Environmental parameter	Damping coefficient, β	0.005

understood easily as the higher V_e will lead to the cantilever vibrating closer to the source and drain, which cause more electrons to be shuttled. From the circuit point of view, the conductance increases exponentially with the displacement, therefore increasing the averaged current. Conversely, under different ΔV, the relations between V_e and I_a has also been calculated in Fig. 6.10 (b). As shown in Fig. 6.10 (b), the relation is not linear, and instead an exponential relation in the first part, followed by a peak value, then reducing to smaller values can be seen. This is a little bit obscure, as it seems from the results that there is an optimal V_e, under which the I_a reaches to the maximum value. The phenomenon is elucidated as follows: The electrical current from D to S is calculated by the product of the potential difference ΔV and conductance between D, S and the centre electrode G. Mathematically, it is expressed as $I_{DG,GS} = (V_{D,S} - V_G)G_{DG,GS} = \Delta V \cdot G_{DG,GS}$. From the previously mentioned data, ΔV decreases as $V_{D,S}$ is a constant value and V_G is increasing with the increasing Q, which is governed by the gap between G and $D(S)$ determined by the external driving voltage V_e. On the other hand, the $G_{DG,GS}$ exponentially increases with the tip displacement of the cantilever. In the first part of the I_a-V_e curve, exponentially increased $G_{DG,GS}$ dominates the trend of the $I_{DG,GS}$, while there must exist an optimal $I_{DG,GS}$ where the decreasing ΔV meets the increasing $G_{DG,GS}$. From the view point of device physics, it can be elucidated that although the increasing displacement due to an increased driving voltage causes more

charges being induced on the terminal G (this has been validated in the calculation), the actual number of transported charges contributing to the overall electrical current reduces because the potential drop ΔV has a much lower value leading to less electrons being loaded (unloaded) to the terminal G. Further increase in the V_e is not possible as the displacement will exceed the 1 nm range, leading to inaccurate results. Finally, the threshold voltage V_e at

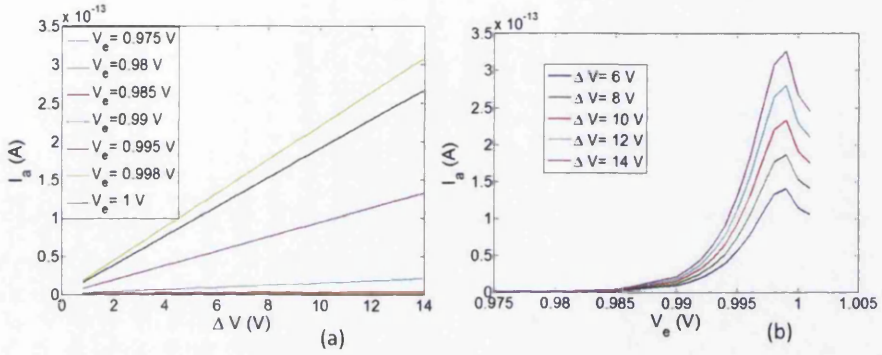

Fig. 6.10 Simulated results for the aver-age current I_a versus applied voltages. (a) I_a versus DC voltages applied to terminal D and S. (b) I_a versus external driving voltages to the cantilever V_e.

which the shuttle regime starts working has been investigated with $\Delta V = 13$ V. It is seen in the Fig. 6.11 the threshold is at the $V_e = 0.965$ V, as the I_a is increased abruptly at that point.

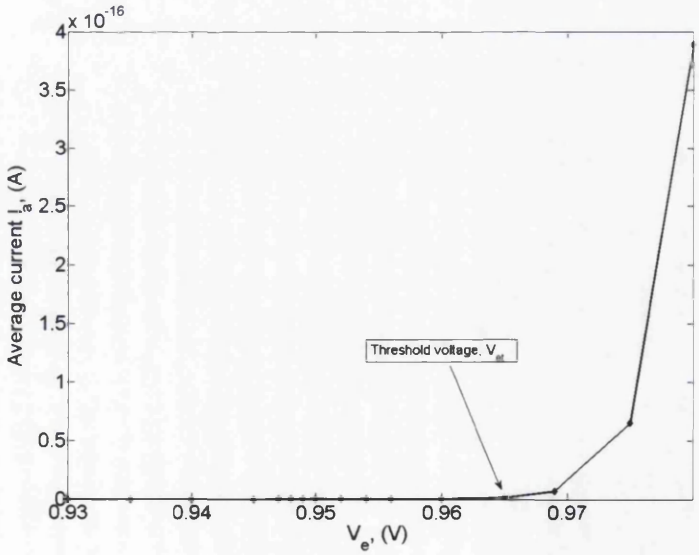

Fig. 6.11 Calculation of the I_a versus V_e to obtain the threshold voltage V_{et}.

6.5 Application of The LSEMT to A Mass Sensor

The novel mass sensor proposed in the first section has the merits such as high sensitivity, small size and energy-saving. It has the potential applications for ultra-sensing such as in zg scale, but there is always a trade off between sensitivity and controllability. To control such a nano-device is a challenging work. Besides, the fabrication process can be imagined to be very difficult. Here, by employing the LSEMT, a more controllable and practical mass sensor has been investigated, as shown in Fig. 6.8 (c). It has the similar structure with the one studied already, but the motion of the active beam is driven externally, in which the tunnelling effect is becoming adjustable and controllable. And the fabrication is supposed to be easier as it is practically designed in large size.

Numerically, the investigation starts form the mathematical modelling of the two coupled beams (active and passive). It is quite easy to give the motion equations. For the active:

$$m_1\ddot{x}_1 = -b\dot{x}_1 - kx_1 - k_3x_1^3 - k_{12}(x_1 - x_2) + F \tag{6.11}$$

For the passive:

$$m_2\ddot{x}_2 = -b\dot{x}_2 - kx_2 - k_3x_2^3 - k_{12}(x_2 - x_1) \tag{6.12}$$

where k_{12} is the coupling coefficient determined by the overhang part, and it usually extracted from the experiment. Here, the value of k_{12} is designated to a small value (0.0002), so that the two cantilevers can be treated as weakly coupled. Re-arranging Eqs. 6.11 and 6.12, it arrives:

$$\begin{aligned} \ddot{x}_1 + 2\beta\omega_1\dot{x}_1 + \omega_1^2x_1 + \omega_1^2k_3x_1^3/k + \omega_1^2k_{12}(x_1 - x_2)/k = \omega_1^2F/k \\ \ddot{x}_2 + 2\beta\omega_2\dot{x}_2 + \omega_2^2x_2 + \omega_1^2k_3x_2^3/k + \omega_2^2k_{12}(x_2 - x_1)/k = \omega_1^2F/k \end{aligned} \tag{6.13}$$

where ω_1 and ω_2 are resonant frequencies of the active and passive cantilever, respectively, and it is assumed that the two have the same damping ratio β and the same geometrical dimensions as in Table 6.1. By keeping the same initial electronic boundary conditions of the active beam and combining the Eqs. 6.11, 6.12 and 6.10, a quantitative study can be conducted to investigate the performance of the mass sensor. First of all, the case without mass attached to the passive beam has been simulated. The result is shown in Fig. 6.12. It is seen that the passive cantilever has been excited by the active cantilever through the coupling effect. The peak-peak oscillating amplitude ($\approx$ 1 nm)of the passive one is much lower than that of the active cantilever ($\approx$ 20 nm). The charge on G has also been calculated and shown in Fig. 6.12 (b). Fig. 6.12 (c) shows the current flowing through the terminal D and S. It

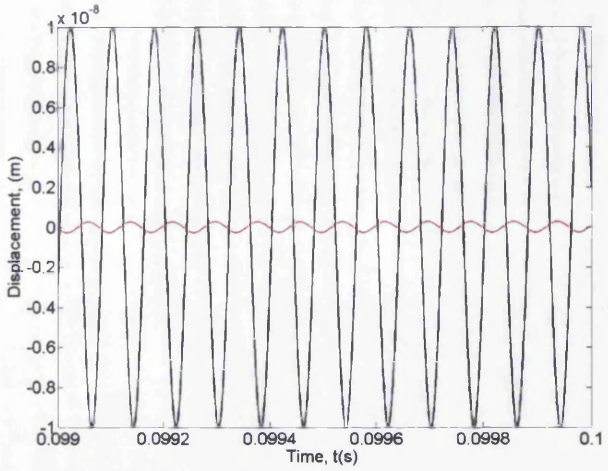

(a) simulated tip displacements for two coupled cantilevers.

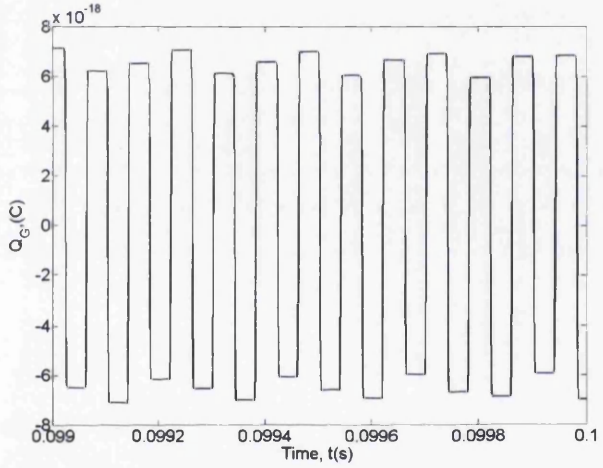

(b) calculated charge G_Q.

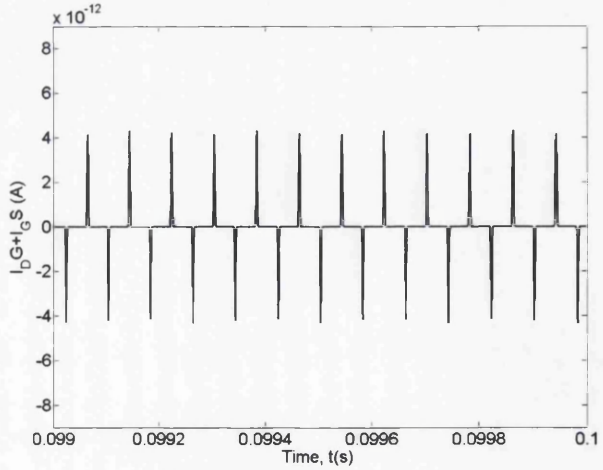

(c) calculated electrical current through terminals D and S.

Fig. 6.12 Calculated results for two coupled cantilevers, one of which forms the electromechanical transistor.

is seen although the exact values in results shown in Fig. 6.12 are slightly different from those in Fig. 6.9, hinting that with an coupled mechanical beam attached, the performance of the LSEMT remain qualitatively stable. Simulation results have validated that the idea of the coupled mechanical cantilever with one embedded in a LSEMT is viable. Further, mass sensing is analysed using an equivalent value of mass in comparison to the beam mass. Suppose that the ratio of the added mass m_a over the effective beam mass m_e increases from around $0.002 \sim 0.0039$, the change of the average electrical current I_a has been calculated and shown in Figs. 6.13, 6.14, 6.15 and 6.16. Fig. 6.13 shows that the I_a linearly increases with the increase in ΔV. Fig. 6.14 shows that the relation between I_a and the mass ratio

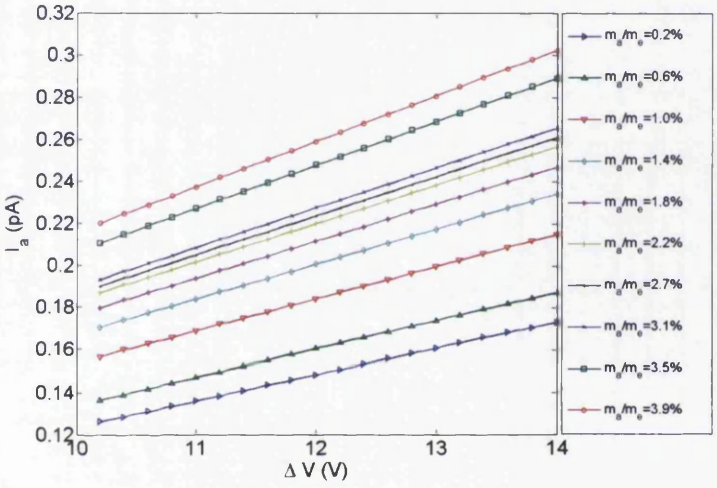

Fig. 6.13 Electrical current versus voltage applied on D and S with various added mass on the passive beam.

m_a/m_e is not linear, there exists a region (0.033 – 0.035) within which the I_a is most sensitive with the mass change. The increased electrical current with added mass is elucidated by the results shown in Fig. 6.15, wherein the ratio of the displacement amplitudes of the two cantilevers A_a/A_p versus the ratio of added mass m_a/m_e is presented. It is seen that the vibrational amplitude of the active cantilever increases with the added mass, leading to an increase of the electrical current. In order to investigate the impact of the k_{12} on the device performance. k_{12} ranging from 1×10^{-12} to 0.00047 has been varied. It has been found from Fig. 16 that the average current I_a has a maximum value at $k_{12} = 0.0001$ above which I_a reduces with increasing k_{12}. The value of 0.00047 has been calculated to be the maximum value beyond which I_a becomes to zero due to the much reduced vibration amplitude of the active beam. Also it has been concluded from calculations that I_a reduces to nearly a constant

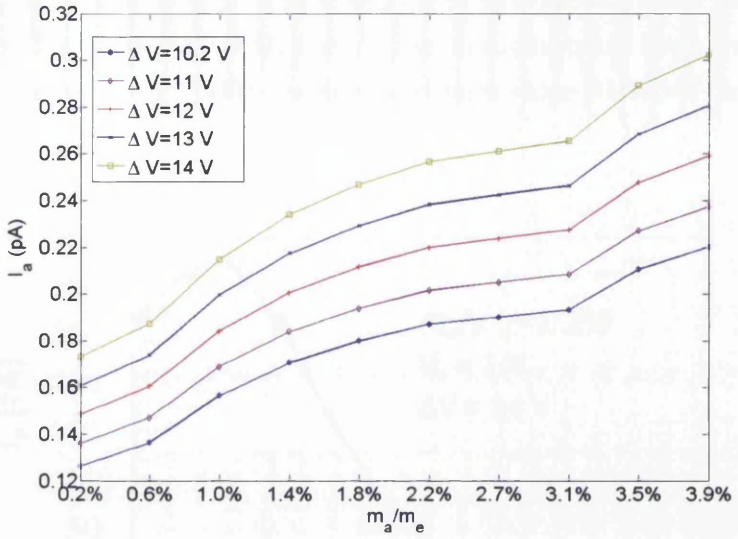

Fig. 6.14 Electrical current versus added mass at different δV.

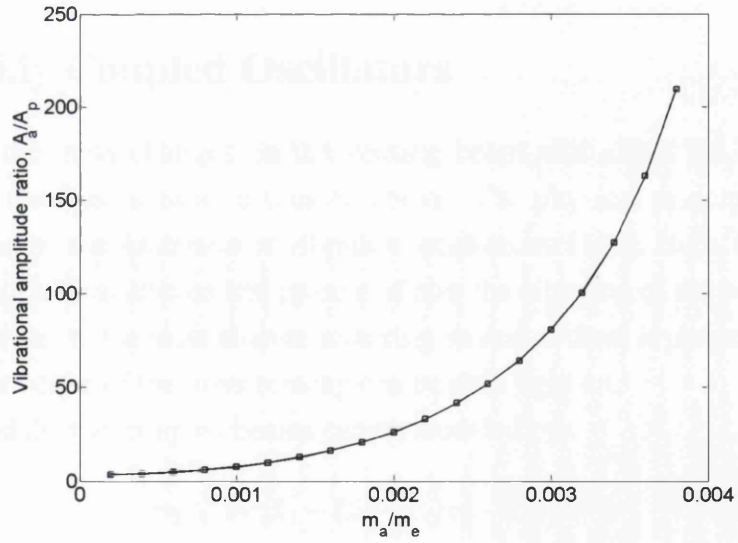

Fig. 6.15 The displacement ratio (A_a/A_p) of the active beam and passive beam versus added mass ratio (m_a/m_e).

value when k_{12} is smaller than 0.0001. I_a remains unchanged when further reducing k_{12} to 1×10^{-12}. It is envisaged that the very small k_{12} indicates the two cantilevers are almost separate; hence, any added mass on the passive cantilever will not affect the dynamics of the active cantilever. The value of 0.0002 used in the simulation has been chosen in the linear region of the range between 0.0001 and the maximum value (0.00047) in order to achieve meaningful results.

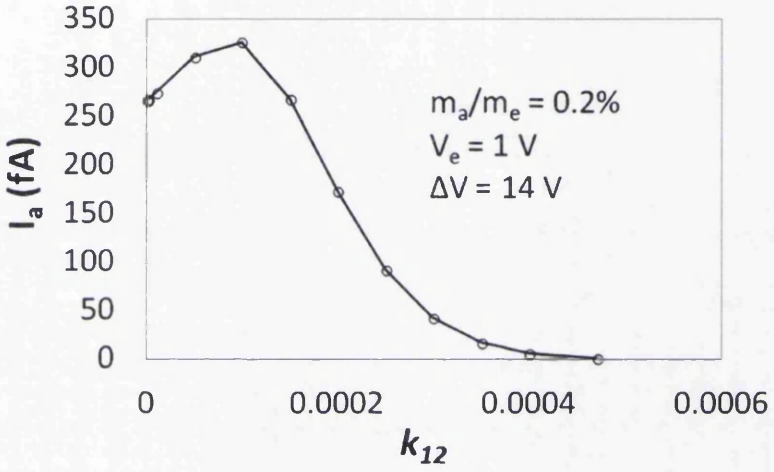

Fig. 6.16 Calculated results for I_a versus k_{12}.

6.6 Weakly Coupled Oscillators

It is seen that the mass changes on the sensing beam will affect the amplitude of the active beam in the mass sensors discussed above. The physical principle behind of this can be explained by the Anderson or vibration localization [149]. Here, by employing the perturbation theory, the mathematical process of how the vibration of the two coupled beams affect each other due to the mass change occurring on one of them is presented, and from the deduction the principle of the mass sensing can be shed lignt on.

It is assumed the two coupled beams can be modeled by:

$$\begin{aligned} m_1\ddot{x}_1 + c_1\dot{x}_1 + (k_1 + k_c)x_1 - k_c x_2 &= 0 \\ m_2\ddot{x}_2 + c_2\dot{x}_2 - k_c x_1 + (k_2 + k_c)x_2 &= 0 \end{aligned} \tag{6.14}$$

where $m_{1,2}$, $k_{1,2}$, $c_{1,2}$ and $x_{1,2}$ are corresponding to mass, spring constant, damping ratio and displacement of the beam 1 and 2. k_c is the coupling coefficient. The Eq. 6.14 can be written

in a matrix form, as:

$$[M]\{\ddot{x}_i\} + [C]\{\dot{x}_i\} + [K]\{x_i\} = 0 \tag{6.15}$$

where

$$M = \begin{bmatrix} m_1 & 0 \\ 0 & m_2 \end{bmatrix} \qquad C = \begin{bmatrix} c_1 & 0 \\ 0 & c_2 \end{bmatrix} \qquad K = \begin{bmatrix} k_1 + k_c & -k_c \\ -k_c & k_2 + k_c \end{bmatrix} \tag{6.16}$$

and $i = 1,2$. For simplicity, the two beams are taken to be identical so that $m_1 = m_2 = m$, $k_1 = k_2 = k$ and $c_1 = c_2 = 0$, where the damping force is ignored. By taking $[x_1 \quad x_2]^T = [u_1^0 \quad u_2^0]^T e^{j\omega t}$ and $\lambda = \omega^2$, the Eq. 6.15 can be turned into an eigenvalue problem, which is given by:

$$[K][u_1^0 \quad u_2^0]^T = \lambda [M][u_1^0 \quad u_2^0]^T \tag{6.17}$$

Solving the Eq. 6.17, the eigenvector and eigenvalue are calculated to be:

$$u_1^0 = \frac{1}{\sqrt{2}}\begin{bmatrix} 1 \\ 1 \end{bmatrix}, \quad \lambda_1^0 = k/m \quad and \quad u_2^0 = \frac{1}{\sqrt{-2}}\begin{bmatrix} 1 \\ -1 \end{bmatrix}, \quad \lambda_2^0 = (k+2k_c)/m \tag{6.18}$$

If there is a small mass change on the second beam (sensing beam), the vibration modes will be changed as well, which can be reflected by the vibration amplitude $u_{1,2}^0$ and frequency λ. According to the perturbation theory, the perturbed eigenvalue and amplitude are give by:

$$\begin{aligned} \lambda_i &= \lambda_i^0 + u_i^{0T}(dK - \lambda_i^0 dM)u_i^0 \\ u_i &= u_i^0(1 - \frac{1}{2}u_i^{0T} dM u_i^0) + \sum_{j=1, j\neq i}^{N} \frac{u_j^{0T}(dK - \lambda_i^0 dM)u_i^0}{\lambda_i^0 - \lambda_j^0} u_j^0 \end{aligned} \tag{6.19}$$

where the dK means the changes on the K, but here $dK = 0$. Likewise, dM is the changes on M, which is: $[0 \quad 0; \quad 0 \quad d]^T$. The d represents the mass change d on the sensing beam. By calculating from the Eq. 6.20, relative change of the frequency and amplitude of the beam without mass change (active beam) are obtained, as:

$$\begin{aligned} \frac{\lambda_1 - \lambda_1^0}{\lambda_0} &= -\frac{d}{2} \\ \frac{u_1 - u_1^0}{u_1^0} &= \left(\frac{1}{4} + \frac{k}{4k_c}\right) d \end{aligned} \tag{6.20}$$

It is seen from the Eq. 6.20 that relative amplitude change on the active beam is affected by coupling coefficient k_c, and if the k_c is decreased the relative change on amplitude can be made orders of magnitude greater than the relative change on the frequency. This conclusion implies the merit of detecting amplitude change is easier than the frequency change in mass sensors designed. To be more accurate, the relationship between the relative amplitude changing and the ratio of k/k_c in the Eq. 6.20 has been calculated and the result has been shown in Fig. 6.17, where it is seen that only when the ratio of k/k_c is larger than 1 the relative amplitude changing is larger than the relative frequency changing (1/2) which is not related to the coupling constant k_c. The zone indicated by the red box in Fig. 6.17 means the relative frequency changing is larger.

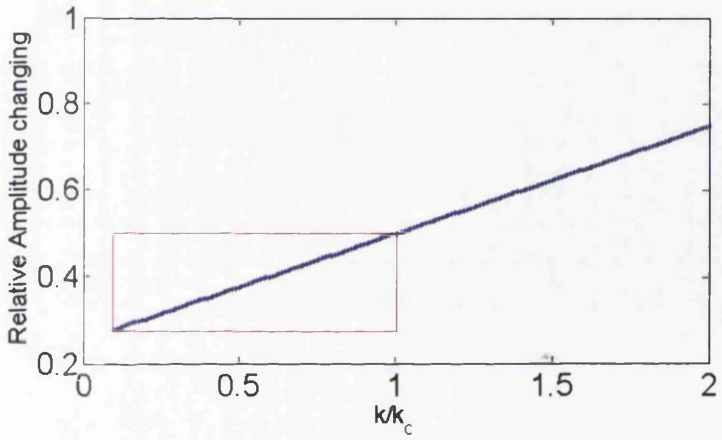

Fig. 6.17 Amplitude changing versus the ratio: k/k_c. Red box indicates the zone when relative frequency changing is larger.

6.7 Conclusion Remarks

In the first part of this chapter, a novel mass sensor based on two coupled mechanical cantilevers, one of which is embedded in a NMT, has been presented. Numerical simulation on this device shows that the device is able to sense the added mass by observing the current flow in the NMT. With the practical concern, the LSEMT has been designed and subsequently simulated using the motion equation and charge transfer equation. Results show that using an external periodic driving force, the cantilever can be excited to vibrate, demonstrating successfully the charge shuttling effect. A practical design of a mass sensor based on the LSEMT has also been proposed, which consists of two coupled mechanical cantilevers, one serving as the shuttle of the LSEMT, and the other serving as purely the sensing function. The advantage of the sensor design is that the active cantilever is embedded inside the LSEMT

free from measured purely performing signal extraction and excitation, only leaving the passive cantilever as a probe exposed in the environment to detect the mass change. Due to the nature of detecting vibrational amplitude change (eigenstate shifts method), high sensitivity can be achieved. Numerical simulations have been conducted to quantitatively validate this concept.

Chapter 7

An Optical Driven Electromechanical Transistor Based on Quantum Tunnelling Effect

7.1 Background

7.1.1 Existing Works

The field of cavity optomechanics has been attracting many researchers to make their efforts both in theoretical work and experiments. Phenomenon such as quantum entanglement [150], Quantum manifestation [25], dynamical back-action, bi-stability, optomechanical cooling [151] [152] and so on have been intensively investigated. Experimentally, due to the rapid advance of micro/nano-mechanical fabrication, various of optical devices have been designed [152]. The researchers have conducted many interesting experiments. For example, the motion of a thermal cloud of Cs atoms trapped inside an optical cavity was cooled by cavity optomechanics in [153]. Quantum-coherent coupling of a mechanical oscillator to an optical cavity mode has been achieved in [154], and this achievement have paved the way for establishing an efficient quantum interface between mechanical oscillators and optical photons. Based on the standard processing techniques, D. K. Armani et al. [155] have successfully fabricated an Ultra-high-Q (UHQ) silica toroid micro-cavity on a chip, and it has opened a new window for investigating the optical-mechanical coupling effect. Take Tal Carmon's work for example, in [156], it is observed that the input cw pump power, as it is increasing, can be modulated by the coupled UHQ toroidal micro-cavity into random oscillations. In [157], they found the radiation pressure induced vibration of the micron-scaled on-chip resonators can modulate the input cw light to be chaotic by calculating

the Lyapunov exponent. And in [158], the optoexcited vibrations of a micron-scale on-chip resonator were analysed, and different eigen-mechanical modes with greater than 1 GHz frequency were reported.

7.1.2 The Concept of Radiation Pressure

Essentially, almost all the work described above are based on radiation pressure (RP), which plays the role for coupling the optical and mechanical field [159] [160]. Quantumly, the

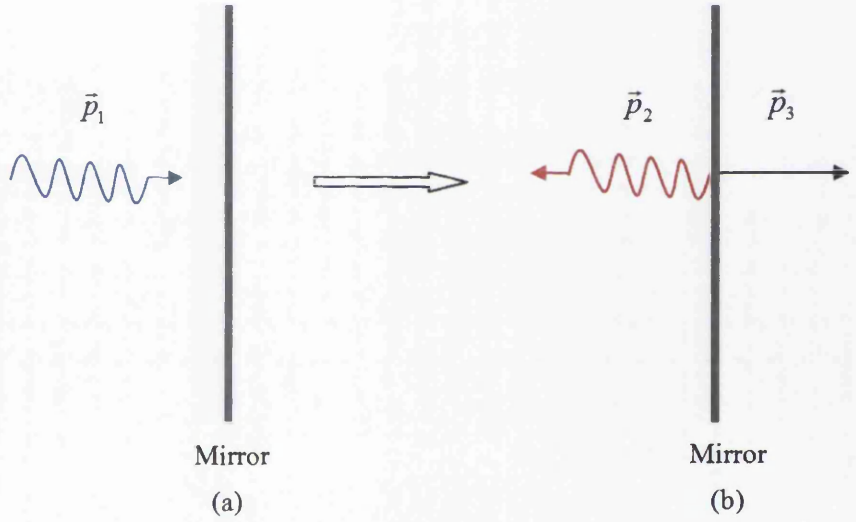

Fig. 7.1 Schematic diagram of a photon interact with a mirror.

light (electromagnetic wave) is described by the particle called photon. For a photon, its momentum is given by: $\vec{p} = \hbar\vec{k}$, where $\hbar$ is the reduced Planck constant and $\vec{k}$ is the wave vector, and the energy of a photon is given by: $E = \hbar\omega = hc/\lambda$, where h is Planck constant, c is the light velocity and λ is the wavelength of the light. In order to understand what the RP is, a schematic graph that illustrates the interaction between a photon and a mirror has been presented in Fig. 7.1. In Fig. 7.1 (a), a photon with momentum $\vec{p}_1$ is hitting towards a stationary mirror. After the interaction, in Fig.7.1 (b), it is shown that the photon is bouncing back with momentum $\vec{p}_2$ and the mirror has gained a momentum $\vec{p}_3$. According to the momentum conservation law, it has: $\vec{p}_1 = \vec{p}_3 - \vec{p}_2$. The $\vec{p}_2$ is assumed to be $-\vec{p}_1$. Thus, the change in momentum of a photon is $2\vec{p}_1 = 2\hbar k$. If there is a incoming light with optical power P, it will have N photons per second involved, where the N can be calculated by the optical power divided by the energy per photon, i.e. $N = P/(\hbar\omega)$. Then, the total momentum change per second (i.e. RP) can be easily calculated by $2\hbar k \times P/(\hbar\omega)$. To summarize it, the RP comes from the momentum change of all the involved photons per second.

7.1.3 The Applications of RP

The RP behaves like a bridge connecting the optical field (laser) and mechanical part (could be a cavity). A very tiny changes occurring on the two sides might affect each other through the bridge because of the small wavelength the light field holds. Based on this mechanism, many applications have been exploit by employing optomechanical systems. For example, in [161], they have fabricated an optomechanical oscillator (OMO) for high-resolution mass sensing, in which a very tiny mass changes on the resonator can be detected by observing the modulated transmitted optical power. In [162], the sensitive transduction of the motion of a micro-scale cantilever using optomechanical method has been realized, where the displacement sensitivity can reach as high as about 4.4×10^{-16} m/(Hz)$^{1/2}$. A high resolution microchip optomechanical accelerometer that makes use of ultra-sensitive displacement readout using a photonic-crystal nano-cavity has been designed and tested [163]. A hybrid on-chip optomechanical transducer that has high force sensitivity (74 aN Hz$^{1/2}$) and stable readout were achieved in [164]. Apart from the sensing applications, the cavity optomechanics on a non-solid resonator with liquids were also tried [165]. However, the applications referenced have an unfavoured aspect that they all need a very complicated readout unit, which might be used for frequency measurement, and this indeed limits practical use. And as a matter of fact, the high integrated device would be more favoured for really making the designs to be better realized. Is there a direct way to couple the optical, mechanical and electrical field together? In this chapter, the possibility for coupling the three fields together will be explored. By employing an UHQ cavity that were experimentally realized and the shuttle mechanism that were studied in last chapter, a novelty optical driven electromechanical transistor will be proposed, which can capture the mechanical motion and transfer it directly into current by quantum tunnelling. A coupled dynamical system that describe the whole coupled system will be analysed, and from the result the working range, switch voltage and performance of the device will be presented. This design is believed to have potential applications in sensing field [163] and information procession area [166].

7.2 Model Construction

The design of the device is schematically shown in Fig. 7.2. It consists of an Ultra-high-Q (UHQ) toroid cavity and a CW laser pump. The laser is coupled into the cavity by the fibre taper. There are two electrodes (D and S) mechanically fixed in the vicinity of the cavity forming the drain and source. The G point on the cavity, essentially a small metallic grain, is working as the gate. Under the circulating optical power built in the cavity, the cavity will be deformed because of the radiation pressure (RP). This deformation, at the same time, breaks

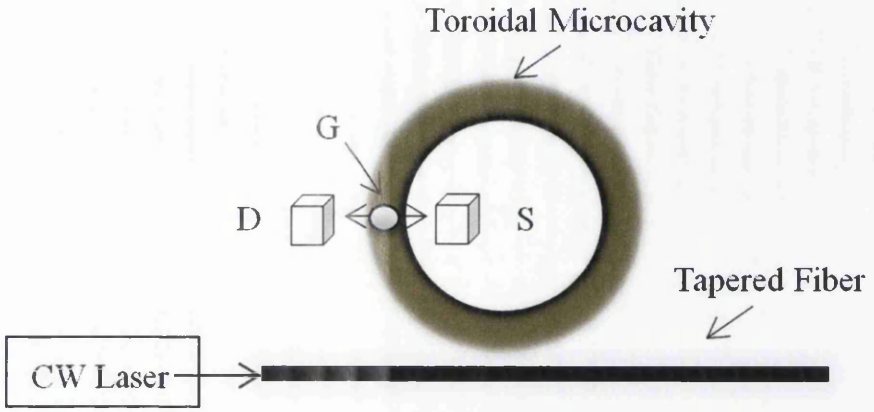

Fig. 7.2 Schematic graph of the transistor which is driven by a CW laser pump.

the resonance between the cavity and the CW laser wave, and thereby lowering the RP. Due to the restoration of the mechanical flex, the cavity will repeat the expansion and extraction process, behaving as an oscillator. The motion of the oscillator that depends on the input power of the CW laser will be oscillating periodically or even quasi-periodically. In such a dynamical regime, under a DC voltage applied between source and drain, the metal bead G will load from S and then download to D a small amount of electrons based on tunnelling effect, which is known as the shuttle regime. This model can be represented by the equivalent circuit as depicted in Fig. 6.8 (b), where C_{GS} and C_{DG} are capacitance between terminals S and G, and G and D respectively. C_{G0} is the capacitance between bead and ground. Q_G is the charge carried by the G, which varies with the displacement of the cavity. G_{GS} and G_{DG} are conductance between S and G, G and D respectively, which are functions of the cavity displacement, that is $G_{DG,GS} = G^0_{DG,GS} e^{(\mp x_1/\lambda)}$, where $G^0_{DG,GS}$ is the initial conductance. x_1 is the displacement of the cavity. λ is the tunnelling length defined as: $\lambda = (2\sqrt{2m_e\phi}/\hbar)^{-1}$. Here m_e is the mass of a single electron, $\hbar$ is the Planck constant divided by 2π, ϕ is the working function of the electrode. The terminal B to G is a tunnelling junction, where G_{GB} and C_{GB} are conductance and capacitance between G and B. The dynamics of the Q_G, which describes the charge on the G, can be expressed as [167]:

$$\dot{Q}_G = V_D G^0_{DG} e^{-x_1/\lambda} + V_S G^0_{GS} e^{x_1/\lambda} + V_B G_{GB} - V_G(Q_G) G_\Sigma \tag{7.1}$$

Where the voltage of G is a function of Q_G, and it is written as:

$$V_G(Q_G) = \frac{Q_G + V_D C_{DG} + V_S C_{GS} + V_B C_{GB}}{C_\Sigma} \tag{7.2}$$

and

$$\begin{aligned} C_{\Sigma} &= C_{DG} + C_{GS} + C_{G0} \\ G_{\Sigma} &= G^{0}_{DG} e^{-x_1/\lambda} + G^{0}_{GS} e^{x_1/\lambda} \end{aligned} \tag{7.3}$$

Apart from the electronic part, the motion of the cavity ring can be modelled as a mechanical oscillator that is driven under the radiation force (RP). The RP can be calculated by considering that a photon transfers 4 times its linear momentum to the cavity's walls every time it completes a round trip. As the consequence of total momentum conservation the RP can be obtained as: $f = 2\pi|A(t)|^2 n/c$, where c/n is the velocity of light in the cavity with n is the refractive index and c is vacuum velocity of light, and $A(t)$ is the slowly varying field amplitude. Then, the dynamical displacement of the ring cavity $x_1(t)$ can be described by the following equation:

$$m\ddot{x}_1(t) + b\dot{x}_1(t) + kx_1(t) = \mu f \tag{7.4}$$

where m is the effective mass of the cavity, b is the damping ratio and k is the spring constant of the oscillator. μ is a evaluated constant that gives the conversion of horizontal to lateral force. The motion of the cavity structure leads to the optical resonance shifting, and the time-varied wavelength difference can be obtained by:

$$\Delta\omega(t) = \Delta\omega_0 - \omega\mu x_1(t) 2\pi n/(\lambda_0 N) \tag{7.5}$$

where $\Delta\Omega_0$ is the initial cavity resonance difference when the input pump beam at frequency Ω. N is the number of optical resonance wavelengths along the cavity circumference. Inside of the cavity, the evolution of the circulating optical field amplitudes is described by the established theory in [156], as:

$$\dot{A}(t) + A(t)\left[\frac{\alpha c}{n} - i\Delta\omega(t)\right] = iB\sqrt{\frac{\alpha c}{n\tau_0}} \tag{7.6}$$

where α is the optical loss in the cavity, B is the input pump field, and τ_0 is the circulation time for a photon travelling inside the cavity. The dynamical behaviour [$A(t)$,$r(t)$] of the system can be investigated by combining Eqs from 7.4 to 7.6. For better conducting the calculation, a set of equations that in autonomous form can be further derived by employing

$A(t) = E_{re} + iE_{im}$ and $\dot{x_1} = x_2$, expressed as:

$$\begin{aligned} \dot{x_1} &= x_2 \\ \dot{x_2} &= -ax_2 - bx_1 + c_1(E_{re}^2 + E_{im}^2) \\ \dot{E_{re}} &= (e - fx_1)E_{im} - dE_{re} \\ \dot{E_{im}} &= gE_p - (e - fx_1)E_{re} - dE_{im} \end{aligned} \tag{7.7}$$

, which has four dynamical variables: x_1, x_2, E_{re} and E_{im}. Obviously, The first two equations describe the motion of the cavity. The third and fourth equations describe the dynamics of the intra-cavity field in the cavity. The optical field is detuned by the cavity displacement x_1, which is represented by the term of $(e - fx_1)E_{im,re}$. In equation 7.7, $a = \omega_m/Q_m$, $b = \omega_m^2$, $c_1 = n/(c\rho\pi r^2 R)$, $e = \omega_o - \bar{\omega}$, $d = \alpha c_0/n$, $f = \omega_o^2 n/(cN)$, and $g = \sqrt{\alpha c/n\tau}$. ω_m and Q_m are the frequency and quality factor of the cavity, respectively. ρ is the material density. R and r are the major and minor toroid radii, respectively. ω_o is the frequency of the optical wave, and $\bar{\omega}_o$ is the optical resonance at mechanical equilibrium. τ is the time that light takes to accomplish one round trip in the cavity. $|E_p|^2$ is the input power of the CW laser pump that can be used to modulate the vibrating mode of the cavity. In the calculation, $|E_p|^2$ and $|E|^2$ are the normalized and take the unit of a.u.(dimensionless).

7.3 Numerical Simulation

By combining the Eqs 7.1-7.3 and 7.7 and taking the experimentally adjustable parameters, the simulation has been conducted. The taken parameters are: $a = 1.4 \times 10^6$ Hz, $b = 1.2 \times 10^{17}$ Hz^2, $c = 9779$ Ns, $d = 1.2 \times 10^8$ Hz, $f = 1.1 \times 10^{20}$ sm^{-1} and $g = 2.2 \times 10^{10}$ 1/s^2. The tunnelling length λ is taken 0.5×10^{-10} m. The initial conductance $G^0_{DG,GS}$ are all 1×10^{-10} S. C_{GS} and C_{DG} are all 1×10^{-18} F. $C_{G0} = 2 \times 10^{-18}$ F. The toroidal cavity used here is taken from [156], where it has been experimentally realized. The major and minor of the toroid radii are 14.5 and 3 μm. The mechanical Q_m and optical quality factor Q_e are taken as 250 and 1×10^7, respectively. The metallic gate G is supposed to be a very thin film that has an ignorable effective mass comparing with the toroidal cavity. Thus it will not affect the mechanical resonance of the cavity. Meanwhile the optical quality factor is defined as $Q_e = \omega_e \tau 2\pi/l$, where l is fractional power loss. Obviously, the gate G will not have an effect on any variables in the definition of Q_e. I_{DG} and I_{SG} are defined as currents flowing from D to G , and from S to G, respectively. Results of the numerical calculation when applying DC voltage $V_{DS} = 16$ V and the input power $E_p = 0.2$ are shown in Fig. 7.3, in which it is seen that the Q_G in (a) and $I_{DG} + I_{SG}$ in (b) versus time are all shuttling periodically with

approximately 60 electrons per cycle. The relationship between x_1 and x_2 has been presented in Fig. 7.3 (c), in which there is a single circle meaning the motion of mechanical cavity is in single period/frequency. While in Fig. 7.3 (d), the plot of E_{re} versus E_{im} is performing multi-period motions as more complicated circles are shown. Increasing the input power E_p

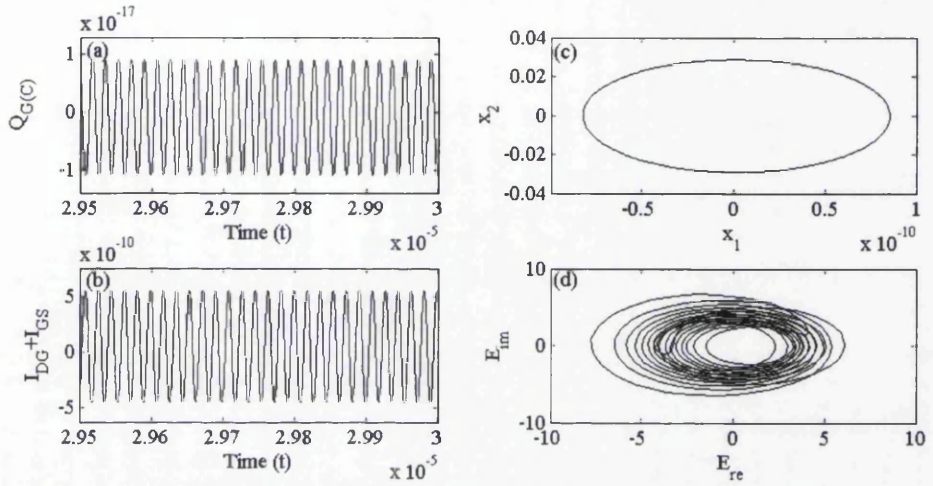

Fig. 7.3 Simulated optical transistor. (a), Charge value at G terminal when the micro-cavity is oscillating periodically. (b), Electrical current flowing through terminal D and S. (c), Plot mechanical deformations x_1 and its velocity x_2. (d), Plot the real part Ere vs imaginary part E_{im} of the slowly varying electric field of the circulating optical mode.

to 1 as well as keeping all other parameters unchanged, the simulation results has been shown in Fig. 7.4. In Fig. 7.4 (a), it is shown that the Q_G has changed to quasi-periodic with about 193 electrons being shuttled per cycle. That is because, under a higher input optical power, the vibration amplitude of the cavity has increased, which leads to an enhanced tunnelling effect. The similar pattern of $I_{DG} + I_{SG}$ versus time is plotted in Fig. 7.4 (b). Meanwhile the 3-dimensional projection of the optical dynamic system (E_{im} and E_{re}) in Figs. 7.5 and 7.6, where a chaotic attractor is displayed in 7.5, and a non-chaotic attractor is shown in 7.6 when $E_p = 0.2$. Furthermore, the Lyapunov exponents of the Eq. 7.7 have been calculated, and it is seen in Fig. 7.8 that the largest exponent $\lambda_1 > 0$, which proves that the optical field (E_{im} and E_{re}), is in chaotic state. The threshold at which the shuttling phenomenon starts with varying input power E_p from 0.005 to 0.4 has been investigated in Fig. 7.9. It is shown that the shuttling begins at $E_p = 0.025$ but with very weak tunnelling, while as E_p increased, it is seen that the maximum Q_G is increased. The range between $E_p = 0.21$ to $E_p = 0.345$ is the best operating range as the transported charge Q_G is more stable. Q_G is directly related to the displacement x_1. Higher E_p values cause the optical resonance to exhibit multi-periodic and eventually chaos, but the peak amplitude of the RP no longer increases. Therefore, x_1/Q_G will saturate at a threshold E_p. Finally, the average current I_a that flows from the source to

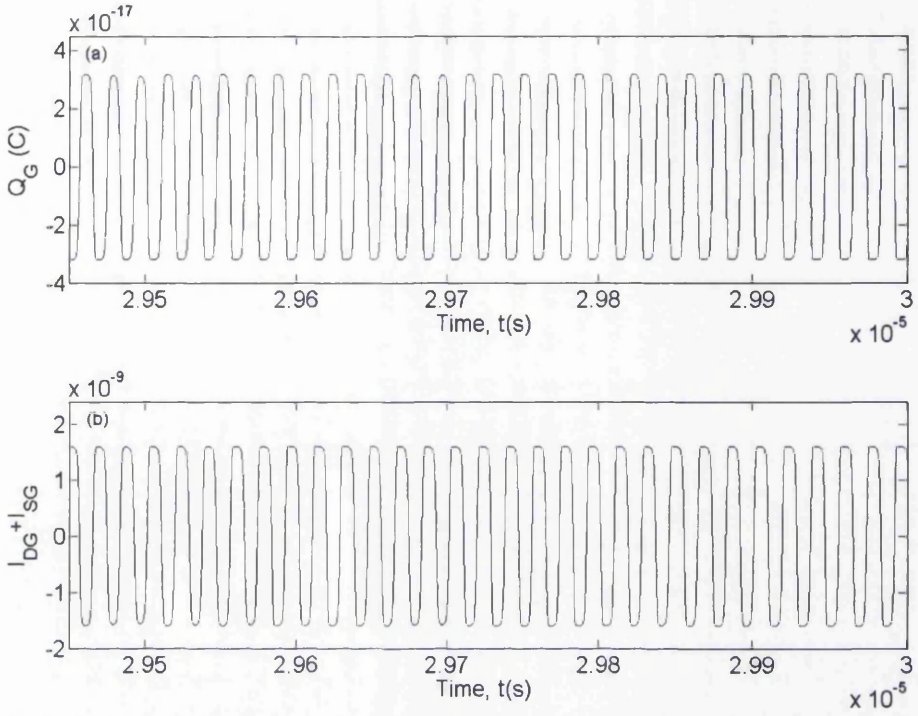

Fig. 7.4 Simulated optical transistor. (a), Charge value at G terminal when the micro-cavity is oscillating in chaotic state. (b), Electrical current flowing through terminal *D* and *S*.

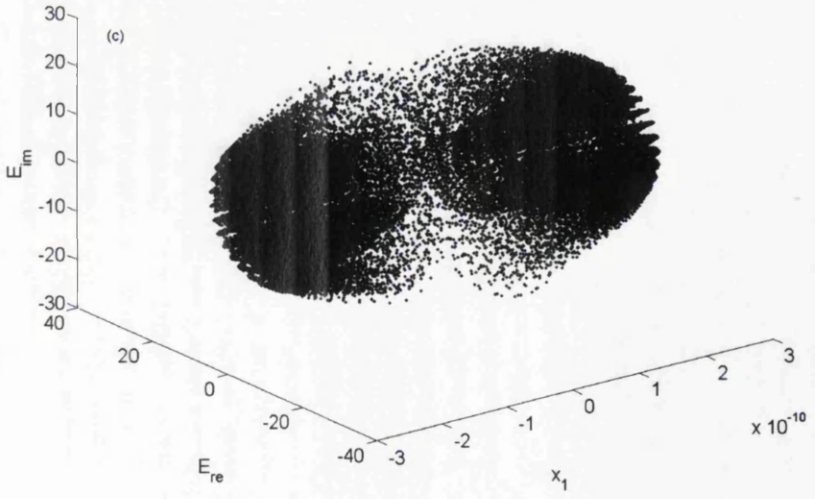

Fig. 7.5 Chaotic attractor of the optical power field.

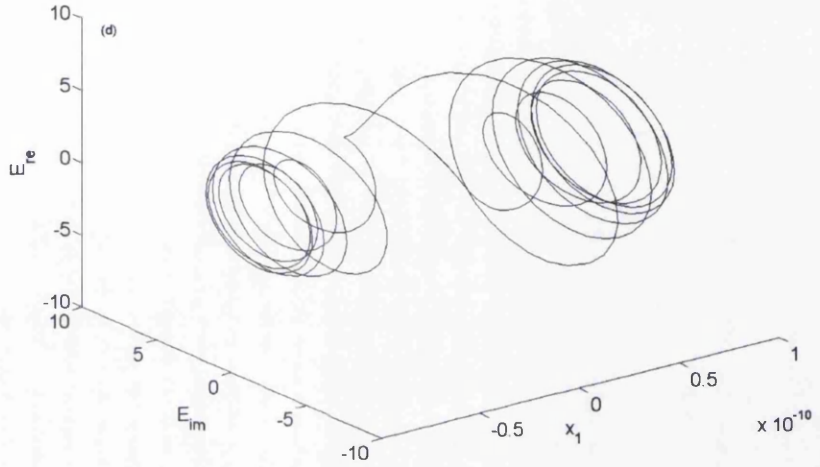

Fig. 7.6 Non-chaotic attractor of the mechanical motion of the cavity when $E_p = 0.2$.

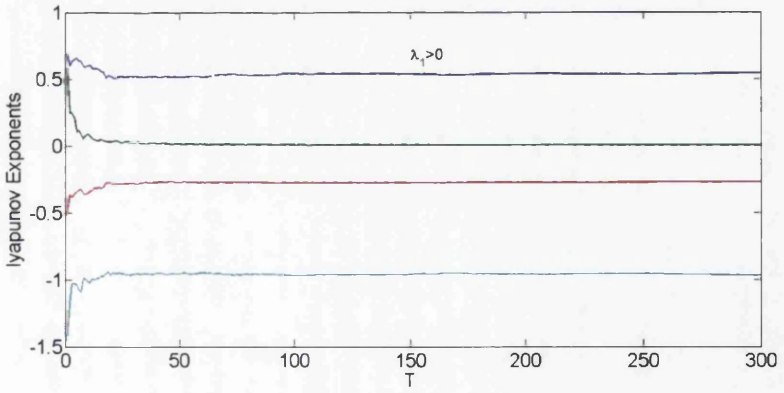

Fig. 7.7 Lyapunov Exponents of the system when pump power Ep=1.

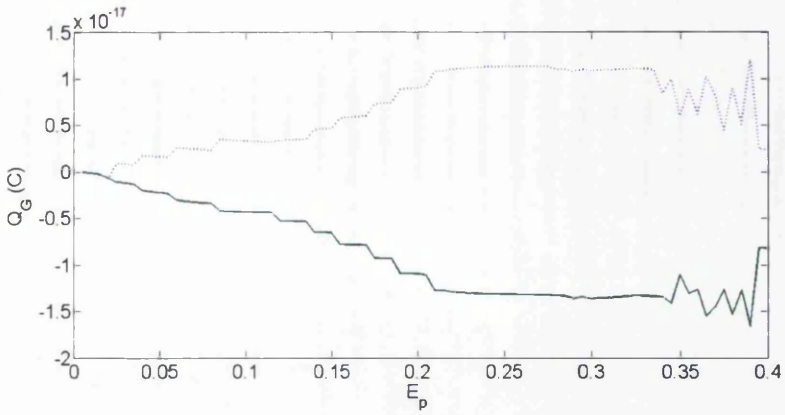

Fig. 7.8 Calculated threshold pump power E_p of opto-electromechanical transistor.

drain with varying potential between V_D and V_S in Fig. 7.9. The upper line is the case when the optical field is in the chaotic state $E_p = 1$ and the lower line is calculated at $E_p = 0.2$ at which the optical field is in the period state. It is interesting to find that both the two states have a linear curve even when the system is driven at high input power. It is found from the simulation results that the electromechanical transistor system has a much wider stable range than the optical resonating system in the cavity. This is interpreted as follows. At high input optical power, the optical wave inside the cavity has been driven into the chaotic state by the large mechanical vibration amplitude of the cavity. However, the chaotic optical field inside the cavity can not drive the mechanical structure into non-periodical regions due to the small quality factor of the mechanical structure compared to very large optical quality factor, as well as the large mechanical restoring force. In other words, the mechanical cavity structure functions as a filter damping out all optical oscillations except for the oscillation at the mechanical resonant frequency. In the meantime, the mechanical vibration still drives the optical field into non-periodic states. This phenomenon is actually advantageous in the proposed transistor device, as the device is able to work in a much wider input optical power range despite the optical filed inside the cavity already displays non-stable vibrations.

7.4 Conclusion Remarks

In conclusion, a new electro-mechanical transistor device operated by optomechanical cavity has been proposed and subsequently modelled. The coupled opto-mechanical-electronic simulation has validated that the device is able to work as a transistor device controlled by the optical RP. Nonlinear analysis of the mechanical vibrations under large driving power has also been analysed. The results conclude that the transistor device has a much wider working

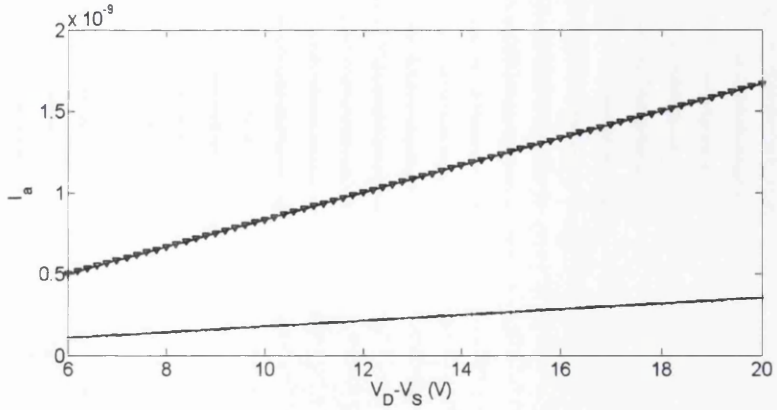

Fig. 7.9 Average current I_a versus applied DC voltage between drain and source ($V_D - V_S$). The upper line is for the optical wave in the chaotic state, and the lower is in linear state.

range compared with the optical field inside the cavity, which has been elucidated from the viewpoints of the mechanical properties of the cavity.

The proposed transistor has potential applications in a few areas. As the optical cavity is compatible with the silicon technology so it could be used as a transducer in the silicon photonics, which can transfer the photon directly into tunnelling current and has the potential to reach very high resolution as a single photon could induce the quantum tunnelling electrons to change. For sensing applications, any changes on the cavity or laser filed can be transferred directly into quantum current which can be easily detected by the electric circuit that is integrated with the tunnelling electrodes. This detection mechanism can greatly scale down the whole device, making the device compact and reducing the noise and unwanted thermalization effects. In quantum information processing area, this device offers a new architecture that can serve as a universal transducer to mediate long-range interactions between stationary quantum systems [152]. Eventually, the proposed device can be used for exploiting the full functionality of micro- and nano- mechanical devices, which can utilize the mechanical motion to achieve the couplings between quantum systems.

Chapter 8

Conclusions and Discussions

8.1 A Brief Summary

From chapter 2 to chapter 7, studies of various of the MEMS/NEMS resonators have been discussed. Theoretical analysis has been given to each of the resonator models that could be the single, the coupled, the arrayed and the multidisciplinary involved. Accompanying with the numerical simulation, noval applications ranging from sensors to transistors have been proposed.

To be specific, in chapter 2, the nanotube resonator model has been further analysed theoretically. Compared with previous works, the role of initial surface effect playing in the dynamics of the resonator, particularly in nonlinear working regime, has been firstly presented. It is found that the initial surface effect increase the resonance frequency of the resonator, and the thresholds of jumping, whirling and chaotic behaviour occurring are all increased to a higher driving voltage than the case without surface effect considered. Interestingly, the patterns of the whirling motion have been plotted, which are exhibiting distinctively under the different driving strength. At the end, an accelerator that use the nanotube resonator has been designed and numerically verified. In chapter 3, a mass sensor that takes advantage of the chaotic synchronization between two MEMS resonators has been designed. The sensing function of it relies on detecting the level of de-synchronization when there is extra mass attached on the sensing beam. Unlike the conventional beam sensors, it can work in the chaotic range. And importantly, due to its special sensing mechanism it is noise-robust, which has been investigated by considering the bounded noise. The coupling method (OPCL) taken for synchronizing the two MEMS resonators is realizable which makes the mass sensor more practical. In chapter 4, an energy harvesting beams array has been studied. A set of equations that describe the charge generation of the beams have been derived by employing beam and piezoelectricity theory. Based on the model, ILM has been

observed in the array by using the strategy that is to change the driving frequency suddenly when the array is in the ST state. The charge generation of the array when it is in the states: ST state and ILM state, has been compared. It is found that more energy can be harvested when the array is set in ILM state. This work has deepened the understanding of the energy harvesters. In chapter 5, Duffing resonators have been divided into two categories: one is with negative stiffness and the other one is with positive stiffness. Two experimental models have been employed to represent the two types of resonators. The theoretical work has mainly discussed the role of the parametric term (pump) in controlling the chaos behaviours in these two types of resonators. It is found that the pump can control the chaos effectively in the resonators with negative stiffness, where because of the pump, the chaotic state can be controlled into periodic states. While, in the parametric Duffing resonator of the positive stiffness it is found that the parametric term can make the transient chaos to disappear sooner. In addition, Melnikov analysis has been conducted for understanding the controllability of the pump in the Duffing resonator of negative stiffness. In chapter 6, in the first part, a novel mass sensor based on nano-mechanical transistor (NMT) has been postulated. The novelty is that the mass sensor employs two weakly-coupled beams, and small amount of mass landed on the passive cantilever causes mechanical properties change, in turn affects the dynamic performance of the active cantilever, which is diagnosed by the tunnelling current of the NMT. The mass sensor has the potential in the quantum sensing field. In the second part, a similar device designed in large-scale has been presented. It overcomes the weakness in fabrication of the NMT. In chapter 7, An optical driven electromechanical transistor based on tunnelling effect has been postulated. It is interesting for realizing a device that can couple three physical fields (the electric, the optical and the mechanical) at the same time. The vibrating optical cavity has been used for shuttling the electrons, and therefore the shuttle current can be adjusted by the optical power, which has been verified by the simulation coupled opto-electrol-mechanical equation. Also, it is found that the transistor has a large stable working range that reaches even when optical resonance enters non-periodic states.

8.2 Discussion and Future Work

More efforts are still needed to be put into exploring the fundamental of the MEMS/NEMS resonators talked above, although some achievement have been made. About the nanotube resonator in chapter 2, two partial differential equations (PDEs) have been derived (Eq. 2.11 and Eq. 2.12) for modelling the motion of the nanotube, and the Galerkin's method that assumed eigenmode to be $\varphi(x) = (2/3)^{1/2}[1 - cos(2\pi x/L)]$ has been employed to solve the PDEs. However, this assumption maybe not that accurate especially when the nanotube has a

large deformation. To increase the accuracy of the calculation, one way is to adopt a more complicated eigenmode function which maybe a summation of multi-frequency eigenmodes. Another way can do is to adopt finite element method to calculate the PDEs directly instead of using Galerkin's method for approximation. Apart from the surface effect, there are other effects, such as nonlocal, playing important role in modelling the motion of the nanotube resonator as well. How to incorporate the nonlocal effect into the PDEs is significant, and this would be as one of the future work. The accelerator proposed in chapter 2 has only been investigated numerically while more practical considerations should be discussed. Elliptical Pattern of the motion of the nanotube resonator when the driving voltage is low has been discovered to be distinctive. This phenomenon may need more explorations.

In chapter 3, the mass sensor has been designed based on the chaotic synchronization which has the potential for eliminating the noise. During the theoretical analysis, the sensed mass is assumed to be added to the effective mass of the sensing beam. This assumption is not accurate because the position of the sensed mass has been ignored. A model that takes the distribution of the sensed mass into account is expected. The realization of the mass sensor has been discussed. More details should be considered such as how to reflect the level of de-synchronization electrically. Also the OPCL method can be realized by the circuit, this may need to be verified in this model. The one to many chaotic synchronization applied in WSN also needs to be further investigated with practical information involved. In one word, practical issues will be extensively considered in the future work.

In chapter 4, The ILM has been realized in an MEM beam array, and the higher charge generation under the ILM has been investigated. While the condition given during the theoretical analysis were idealized, such as the driving term has been taken in the form of $fcos(\omega t)$ and the coupling between beams has been assumed only existing in nearest one. These concerns are expected to affect the generation of the ILM. The dynamics of the generated ILM needs to be investigated further. For example, what is the stability of the ILM like? What factors are affecting the movement of the ILM? Are there any other perturbations that could induce the generation of the ILM?

The controllability of the parametric term in the two kinds of Duffing resonators have been investigated in chapter 5. A parametric term has been intentionally added in the Duffing resonator that has negative stiffness, and effective chaos controllability has been observed. However, the practical concern is how to achieve the parametric modulation in reality. This point will be studied in the future. Of the second type of Duffing resonator, transient chaotic behaviour has been observed. The question is whether there are deterministic chaos existing if other parameters been taken differently. Such as the size of the resonator is becoming

much more smaller, the damping ratio is becoming not linear with velocity and the driving is becoming higher etc. These unknown problems will be investigated in the future.

In chapters 6 and 7, the quantum shuttling has been widely applied. Because of the small reaction distance (~ 0.5nm) of the quantum tunnelling, it indeed can be potentially exploited for sensors that working in quantum regime. The shuttling phenomenon involves many aspects such as material, precise controlling, surrounding physical fields etc. However, the models adopted are all taken ideally. Therefore, in the future work, these considerations will be taken into account. From the viewpoint of physics, the light is seen as photon, the vibration can be seen quantumly as phonon and the electron can be modelled by a wave-particle. So the challenging questions come as whether it is possible to understand the problem in quantum physics. In fact, there are a few literatures that [150][25] have investigated the interaction between the optical and mechanical field quantumly. But the quantum theory of the three physical fields coupled together have not been reported. A Hamilton function for this kind of coupled system should be explored. The self-consistent problem of the three physical fields should be discussed quantumly in the future.

8.3 Achievements during PhD Studies

In this project, several contributions have been made, and the relevant publications are:

1. Leisheng Jin, Jie Mei, Lijie Li,Nonlinear dynamics of doubly clamped carbon nanotube resonator considering surface stress, RSC Advances, **5**, 7215-7221 (2015). (Chapter 2)

2. Leisheng Jin, Xiaoping Wang, Lijie Li, Chaotic synchronization of two microresonators with application in mass sensors, Journal of Applied Physics **113**, 093506 (2013). (Chapter 3)

3. Leisheng Jin, Yan Zhang, Lijie Li, One-to-Many Chaotic Synchronization with Application in Wireless Sensor Network, Ieee Communications Letters, **17**, 9 (2013). (Chapter 3)

4. Leisheng Jin, Jie Mei, Lijie Li, Analysis of intrinsic localised mode for a new energy harvesting cantilever array, European Physical Journal-Applied Physics, **66**, 1 (2014). (Chapter 4)

5. Leisheng Jin, Jie Mei, Lijie Li, Chaos control of parametric driven Duffing oscillators, Applied Physics Letters **104**, 134101 (2014). (Chapter 5)

6. Leisheng Jin, Lijie Li, A Novel Mass Sensor Based on Nanomechanical Transistor, IEEE Electron Device Letters, **1**, 68-70 (2015). (Chapter 6)

7. Leisheng Jin, Lijie Li, Large scale electromechanical transistor with application in mass sensing, Journal of Applied Physics, **116**, 213503 (2014). (Chapter 6)

8. Leisheng Jin, Lijie Li, Surface stress on three-terminal vibrational nanomechanical transistor, Applied Physics Letters **105**, 183507 (2014). (Chapter 6)

9. Leisheng Jin, Lijie Li, An optical driven electromechanical transistor based on tunneling effect, Optics Letters, **40** Issue 8, pp. 1798-1801 (2015). (Chapter 7)

10. Leisheng Jin, Lijie Li, Quantum simulation of ZnO nanowire piezotronics, Nano Energy, **15**, pp. 776–781 (2015). (Appendix A)

References

[1] A.M. Tusset, J.M. Balthazar, D.G. Bassinello, Jr. Pontes, B.R., and JorgeLuisPalacios Felix. Statements on chaos control designs, including a fractional order dynamical system, applied to a "mems" comb-drive actuator. *Nonlinear Dynamics*, 69(4):1837–1857, 2012.

[2] Ioan Grosu, E. Padmanaban, Prodyot K. Roy, and Syamal K. Dana. Designing coupling for synchronization and amplification of chaos. *Phys. Rev. Lett.*, 100:234102, Jun 2008.

[3] A. Uranga, J. Verd, and N. Barniol. Cmos–mems resonators: From devices to applications. *Microelectronic Engineering*, 132(0):58 – 73, 2015.

[4] Ulrich Parlitz and Werner Lauterborn. Superstructure in the bifurcation set of the duffing equation. *Physics Letters A*, 107(8):351 – 355, 1985.

[5] P.J. Holmes and D.A. Rand. The bifurcations of duffing's equation: An application of catastrophe theory. *Journal of Sound and Vibration*, 44(2):237 – 253, 1976.

[6] F.C. Moon and P.J. Holmes. A magnetoelastic strange attractor. *Journal of Sound and Vibration*, 65(2):275 – 296, 1979.

[7] Ron Lifshitz and M. C. Cross. Nonlinear dynamics of nanomechanical and micromechanical resonators, chapter 1. *Wiley-VCH Verlag GmbH and Co. KGaA*, pages 1–52, 2009.

[8] L. D. Landau and E. M. Lifshitz. Nonlinear dynamics of nanomechanical and micromechanical resonators, 3rd edition, §20 and 25. *Butterworth-Heinemann,Oxford*, 1986.

[9] Adam M. Gilbertson, Yan Francescato, Tyler Roschuk, Viktoryia Shautsova, Yiguo Chen, Themistoklis P. H. Sidiropoulos, Minghui Hong, Vincenzo Giannini, Stefan A. Maier, Lesley F. Cohen, and Rupert F. Oulton. Plasmon-induced optical anisotropy in hybrid graphene–metal nanoparticle systems. *Nano Letters*, 15(5):3458–3464, 2015.

[10] A. D. O'Connell, M. Hofheinz, M. Ansmann, Radoslaw C. Bialczak, M. Lenander, Erik Lucero, M. Neeley, D. Sank, H. Wang, M. Weides, J. Wenner, John M. Martinis, and A. N. Cleland. Quantum ground state and single-phonon control of a mechanical resonator. *Nature*, 464:697–703, 2010.

[11] Honghua U. Yang, Robert L. Olmon, Kseniya S. Deryckx, Xiaoji G. Xu, Hans A. Bechtel, Yuancheng Xu, Brian A. Lail, and Markus B. Raschke. Accessing the optical magnetic near-field through babinet's principle. *ACS Photonics*, 1(9):894–899, 2014.

[12] Vikrant J. Gokhale and Mina Rais-Zadeh. Phonon-electron interactions in piezoelectric semiconductor bulk acoustic wave resonators. *Scientific Reports*, 4(5617), 2014.

[13] Nam-Young Kim, Kishor Kumar Adhikari, Rajendra Dhakal, Zorigt Chuluunbaatar, Cong Wang, and Eun-Soo Kim. Rapid, sensitive, and reusable detection of glucose by a robust radiofrequency integrated passive device biosensor chip. *Scientific Reports*, 5(7807), 2015.

[14] Cheng Zhang, Tao Ling, Sung-Liang Chen, and L. Jay Guo. Ultrabroad bandwidth and highly sensitive optical ultrasonic detector for photoacoustic imaging. *ACS Photonics*, 1(11):1093–1098, 2014.

[15] Perry Schein, Pilgyu Kang, Dakota O'Dell, and David Erickson. Nanophotonic force microscopy: Characterizing particle–surface interactions using near-field photonics. *Nano Letters*, 15(2):1414–1420, 2015. PMID: 25625877.

[16] Chengming Jiang, Chaolong Tang, and Jinhui Song. The smallest resonator arrays in atmosphere by chip-size-grown nanowires with tunable q-factor and frequency for subnanometer thickness detection. *Nano Letters*, 15(2):1128–1134, 2015. PMID: 25575294.

[17] Shunichi Sawano, Takayuki Arie, and Seiji Akita. Carbon nanotube resonator in liquid. *Nano Letters*, 10(9):3395–3398, 2010. PMID: 20681632.

[18] Steven C. Wasserman Selim Olcum, Nathan Cermak and Scott R. Manalis. High-speed multiple-mode mass-sensing resolves dynamic nanoscale mass distributions. *Nature Communications*, 6(7070), 2015. PMID: 20681632.

[19] Qiang Liu, Xiaojuan Feng, Baolin An, and Yuanyuan Duan. Speed of sound measurements using a cylindrical resonator for gaseous carbon dioxide and propene. *Journal of Chemical & Engineering Data*, 59(9):2788–2798, 2014.

[20] Yu Wang, Mario Matteo Modena, Mitja Platen, Iwan Alexander Taco Schaap, and Thomas Peter Burg. Label-free measurement of amyloid elongation by suspended microchannel resonators. *Analytical Chemistry*, 87(3):1821–1828, 2015. PMID: 25539393.

[21] Ferran Martín and Jordi Bonache. Application of rf-mems-based split ring resonators (srrs) to the implementation of reconfigurable stopband filters: A review. *Sensors*, 14(7807):22848–22863, 2014.

[22] Madhav Kumar and Harish Bhaskaran. Ultrasensitive room-temperature piezoresistive transduction in graphene-based nanoelectromechanical systems. *Nano Letters*, 15(4):2562–2567, 2015. PMID: 25723099.

[23] Pasi Häkkinen, Andreas Isacsson, Alexander Savin, Jaakko Sulkko, and Pertti Hakonen. Charge sensitivity enhancement via mechanical oscillation in suspended carbon nanotube devices. *Nano Letters*, 15(3):1667–1672, 2015. PMID: 25662034.

[24] Anders Pors and Sergey I. Bozhevolnyi. Quantum emitters near layered plasmonic nanostructures: Decay rate contributions. *ACS Photonics*, 2(2):228–236, 2015.

[25] Lei Ying, Ying-Cheng Lai, and Celso Grebogi. Quantum manifestation of a synchronization transition in optomechanical systems. *Phys. Rev. A*, 90:053810, Nov 2014.

[26] AliH. Nayfeh, MohammadI. Younis, and EihabM. Abdel-Rahman. Dynamic pull-in phenomenon in mems resonators. *Nonlinear Dynamics*, 48(1-2):153–163, 2007.

[27] R. B. Karabalin, Ron Lifshitz, M. C. Cross, M. H. Matheny, S. C. Masmanidis, and M. L. Roukes. Signal amplification by sensitive control of bifurcation topology. *Phys. Rev. Lett.*, 106:094102, Feb 2011.

[28] Y.C. Wang, S.G. Adams, J.S. Thorp, Noel C. MacDonald, P. Hartwell, and F. Bertsch. Chaos in mems, parameter estimation and its potential application. *Circuits and Systems I: Fundamental Theory and Applications, IEEE Transactions on*, 45(10):1013–1020, Oct 1998.

[29] Chunbiao Gan. Noise-induced chaos and basin erosion in softening duffing oscillator. *Chaos, Solitons and Fractals*, 25(5):1069 – 1081, 2005.

[30] Abdulrahman Seleim, Shahrzad Towfighian, Emmanuel Delande, Eihab Abdel-Rahman, and Glenn Heppler. Dynamics of a close-loop controlled mems resonator. *Nonlinear Dynamics*, 69(1-2):615–633, 2012.

[31] M. Siewe Siewe and Usama H. Hegazy. Homoclinic bifurcation and chaos control in {MEMS} resonators. *Applied Mathematical Modelling*, 35(12):5533 – 5552, 2011.

[32] Barry E. DeMartini, H.E. Butterfield, J. Moehlis, and K.L. Turner. Chaos for a microelectromechanical oscillator governed by the nonlinear mathieu equation. *Microelectromechanical Systems, Journal of*, 16(6):1314–1323, Dec 2007.

[33] Eyal Buks and Bernard Yurke. Mass detection with a nonlinear nanomechanical resonator. *Phys. Rev. E*, 74:046619, Oct 2006.

[34] J. S. Aldridge and A. N. Cleland. Noise-enabled precision measurements of a duffing nanomechanical resonator. *Phys. Rev. Lett.*, 94:156403, Apr 2005.

[35] Kenichi Maruyama, Kosuke Sawabe, Tomo Sakanoue, Jinpeng Li, Wataru Takahashi, Shu Hotta, Yoshihiro Iwasa, and Taishi Takenobu. Ambipolar light-emitting organic single-crystal transistors with a grating resonator. *Scientific Reports*, 5(10221), 2014.

[36] Ciyuan Qiu, Weilu Gao, Robert Vajtai, Pulickel M. Ajayan, Junichiro Kono, and Qianfan Xu. Efficient modulation of 1.55 μm radiation with gated graphene on a silicon microring resonator. *Nano Letters*, 14(12):6811–6815, 2014. PMID: 25403029.

[37] Qingfei Chen, Liang Huang, Ying-Cheng Lai, and David Dietz. Dynamical mechanism of intrinsic localized modes in microelectromechanical oscillator arrays. *Chaos*, 19(1):–, 2009.

[38] Alexander Jimenez-Triana, Guchuan Zhu, , and Lahcen Saydy. Output-feedback control of a chaotic mems resonator for oscillation amplitude enhancement. *Mathematical Problems in Engineering*, 2014(745963):–, 2014.

[39] Steven H. Strogatz. Nonlinear dynamics and chaos: With applications to physics, biology, chemistry and engineering. *Perseus Books*, pages 311–319, Jun 1994.

[40] Hsin-Ying Chiu, Peter Hung, Henk W. Ch. Postma, and Marc Bockrath. Atomic-scale mass sensing using carbon nanotube resonators. *Nano Letters*, 8(12):4342–4346, 2008. PMID: 19053791.

[41] B. Lassagne, D. Ugnati, and M. Respaud. Ultrasensitive magnetometers based on carbon-nanotube mechanical resonators. *Phys. Rev. Lett.*, 107:130801, Sep 2011.

[42] J. Moser, J. Güttinger, A. Eichler, M. J. Esplandiu, D. E. Liu, M. I. Dykman, and A. Bachtold. Ultrasensitive force detection with a nanotube mechanical resonator. *Nature Nanotechnology*, 8(0):493–496, 2013.

[43] B. Arash and Q. Wang. Detection of gas atoms with carbon nanotubes. *Scientific Reports*, 3(1782), 2013.

[44] Merce Pacios, Nihan Yilmaz, Iñigo Martín-Fernández, Rosa Villa, Philippe Godignon, Manel Del Valle, Jordi Bartrolí, and Maria Jose Esplandiu. A simple approach for {DNA} detection on carbon nanotube microelectrode arrays. *Sensors and Actuators B: Chemical*, 162(1):120 – 127, 2012.

[45] Ahmed M. Elseddawy, Walid A. Zein, and Adel H. Phillips. Carbon nanotube-based nanoelectromechanical resonator as strain sensor. *Journal of Computational and Theoretical Nanoscience*, 11(4):1174–1177, 2014-04-01T00:00:00.

[46] P. Stadler, W. Belzig, and G. Rastelli. Ground-state cooling of a carbon nanomechanical resonator by spin-polarized current. *Phys. Rev. Lett.*, 113:047201, Jul 2014.

[47] J. Moser, A. Eichler, J. Güttinger, M. I. Dykman, and A. Bachtold. Nanotube mechanical resonators with quality factors of up to 5 million. *Nature Nanotechnology*, 9:1007–1011, Jul 2014.

[48] Z. Y. Ning, T. W. Shi, M. Q. Fu, Y. Guo, X. L. Wei, S. Gao, and Q. Chen. Transversally and axially tunable carbon nanotube resonators in situ fabricated and studied inside a scanning electron microscope. *Nano Letters*, 14(3):1221–1227, 2014. PMID: 24527775.

[49] Chung Chiang Wu and Zhaohui Zhong. Capacitive spring softening in single-walled carbon nanotube nanoelectromechanical resonators. *Nano Letters*, 11(4):1448–1451, 2011. PMID: 21428322.

[50] Quan Wang and Behrouz Arash. A review on applications of carbon nanotubes and graphenes as nano-resonator sensors. *Computational Materials Science*, 82(0):350 – 360, 2014.

[51] R. Chowdhury, S. Adhikari, and J. Mitchell. Vibrating carbon nanotube based biosensors. *Physica E: Low-dimensional Systems and Nanostructures*, 42(2):104 – 109, 2009.

[52] I.K. Kim and S.I. Lee. Nonlinear resonances of a single-wall carbon nanotube cantilever. *Physica E: Low-dimensional Systems and Nanostructures*, 67(0):159 – 167, 2015.

[53] William G. Conley, Arvind Raman, Charles M. Krousgrill, and Saeed Mohammadi. Nonlinear and nonplanar dynamics of suspended nanotube and nanowire resonators. *Nano Letters*, 8(6):1590–1595, 2008. PMID: 18489167.

[54] Vera Sazonova, Yuval Yaish, Hande Üstünel, David Roundy, Tomás A. Arias, and Paul L. McEuen. A tunable carbon nanotube electromechanical oscillator. *Nature*, 431:284–287, 2004. PMID: 18489167.

[55] Qingfei Chen, Liang Huang, Ying-Cheng Lai, Celso Grebogi, and David Dietz. Extensively chaotic motion in electrostatically driven nanowires and applications. *Nano Letters*, 10(2):406–413, 2010. PMID: 20055431.

[56] Mai Duc Dai, Chang-Wan Kim, and Kilho Eom. Finite size effect on nanomechanical mass detection: the role of surface elasticity. *Nanotechnology*, 22(26), 2011. PMID: 20055431.

[57] Jin He and Carmen M. Lilley. Surface effect on the elastic behavior of static bending nanowires. *Nano Letters*, 8(7):1798–1802, 2008. PMID: 18510370.

[58] Gang-Feng Wang and Xi-Qiao Feng. Surface effects on buckling of nanowires under uniaxial compression. *Applied Physics Letters*, 94(14):–, 2009.

[59] F. Song and G.L. Huang. Modeling of surface stress effects on bending behavior of nanowires: Incremental deformation theory. *Physics Letters A*, 373(43):3969 – 3973, 2009.

[60] B. Bar On, E. Altus, and E.B. Tadmor. Surface effects in non-uniform nanobeams: Continuum vs. atomistic modeling. *International Journal of Solids and Structures*, 47(9):1243 – 1252, 2010.

[61] F. Song, G.L. Huang, H.S. Park, and X.N. Liu. A continuum model for the mechanical behavior of nanowires including surface and surface-induced initial stresses. *International Journal of Solids and Structures*, 48(14–15):2154 – 2163, 2011.

[62] Thomas Rueckes, Kyoungha Kim, Ernesto Joselevich, Greg Y. Tseng, Chin-Li Cheung, and Charles M. Lieber. Carbon nanotube-based nonvolatile random access memory for molecular computing. *Science*, 289(5476):94–97, 2000.

[63] Hua-Jun Chen and Ka-Di Zhu. Ultrasensitive mass sensing with nonlinear optics in a doubly clamped suspended carbon nanotube resonator. *Journal of Applied Physics*, 114(21):–, 2013.

[64] Weixu Zhang, Tiejun Wang, and Xi Chen. Effect of surface stress on the asymmetric yield strength of nanowires. *Journal of Applied Physics*, 103(12):–, 2008.

[65] MAURICE A. BIOT. Mechanics of incremental deformations, chapter 2. *Wiley, New York*, pages 67–82, 1965.

[66] L. Meirovitch. Analytical methods in vibrations. *New York: Macmillan*, 1967.

[67] Jie Mei and Lijie Li. Frequency self-tuning of carbon nanotube resonator with application in mass sensors. *Sensors and Actuators B: Chemical*, 188(0):661 – 668, 2013.

[68] Ye-Wei Zhang, Tian-Zhi Yang, Jian Zang, and Bo Fang. Terahertz wave propagation in a nanotube conveying fluid taking into account surface effect. *Materials*, 6(6):2393, 2013.

[69] Alhussein Albarbar, Samir Mekid, Andrew Starr, and Robert Pietruszkiewicz. Suitability of mems accelerometers for condition monitoring: An experimental study. *Sensors*, 8(2):784, 2008.

[70] Laura Ruzziconi, Abdallah H. Ramini, Mohammad I. Younis, and Stefano Lenci. Theoretical prediction of experimental jump and pull-in dynamics in a mems sensor. *Sensors*, 14(9):17089, 2014.

[71] F.M. Alsaleem, M.I. Younis, and L. Ruzziconi. An experimental and theoretical investigation of dynamic pull-in in mems resonators actuated electrostatically. *Microelectromechanical Systems, Journal of*, 19(4):794–806, Aug 2010.

[72] Barun Pratiher. Stability and bifurcation analysis of an electrostatically controlled highly deformable microcantilever-based resonator. *Nonlinear Dynamics*, 78(3):1781–1800, 2014.

[73] Ehsan Maani Miandoab, Aghil Yousefi-Koma, Hossein Nejat Pishkenari, and Farid Tajaddodianfar. Study of nonlinear dynamics and chaos in mems/nems resonators. *Communications in Nonlinear Science and Numerical Simulation*, 22(1–3):611 – 622, 2015.

[74] Hossein S. Haghighi and Amir H.D. Markazi. Chaos prediction and control in mems resonators. *Communications in Nonlinear Science and Numerical Simulation*, 15(10):3091 – 3099, 2010.

[75] Ehsan Maani Miandoab, Hossein Nejat Pishkenari, Aghil Yousefi-Koma, and Farid Tajaddodianfar. Chaos prediction in mems-nems resonators. *International Journal of Engineering Science*, 82(0):74 – 83, 2014.

[76] Wen-Ming Zhang, Osamu Tabata, Toshiyuki Tsuchiya, and Guang Meng. Noise-induced chaos in the electrostatically actuated mems resonators. *Physics Letters A*, 375(32):2903 – 2910, 2011.

[77] Kwangho Park, Qingfei Chen, and Ying-Cheng Lai. Energy enhancement and chaos control in microelectromechanical systems. *Phys. Rev. E*, 77:026210, Feb 2008.

[78] Abdulrahman Seleim, Shahrzad Towfighian, Emmanuel Delande, Eihab Abdel-Rahman, and Glenn Heppler. Dynamics of a close-loop controlled mems resonator. *Nonlinear Dynamics*, 69(1-2):615–633, 2012.

[79] Haiwu Rong, Xiangdong Wang, Wei Xu, and Tong Fang. Subharmonic response of a single-degree-of-freedom nonlinear vibroimpact system to a randomly disordered periodic excitation. *Journal of Sound and Vibration*, 327(1–2):173 – 182, 2009.

[80] W.Y. Liu, W.Q. Zhu, and Z.L. Huang. Effect of bounded noise on chaotic motion of duffing oscillator under parametric excitation. *Chaos, Solitons and Fractals*, 12(3):527 – 537, 2001.

[81] M. Ali, A. Bohm, and M. Jonsson. Wireless sensor networks for surveillance applications; a comparative survey of mac protocols. In *Wireless and Mobile Communications, 2008. ICWMC '08. The Fourth International Conference on*, pages 399–403, July 2008.

[82] Gang Zhao. Wireless sensor networks for industrial process monitoring and control: A survey. *Network Protocols and Algorithms*, 3(1):46–63, 2001.

[83] Xiaoya Hu, Bingwen Wang, and Han Ji. A wireless sensor network-based structural health monitoring system for highway bridges. *Computer-Aided Civil and Infrastructure Engineering*, 28(3):193–209, 2013.

[84] JeongGil Ko, Chenyang Lu, M.B. Srivastava, J.A. Stankovic, A. Terzis, and M. Welsh. Wireless sensor networks for healthcare. *Proceedings of the IEEE*, 98(11):1947–1960, Nov 2010.

[85] D.R. Frey. Chaotic digital encoding: an approach to secure communication. *Circuits and Systems II: Analog and Digital Signal Processing, IEEE Transactions on*, 40(10):660–666, Oct 1993.

[86] A. Muller and J.M.H. Elmirghani. Chaotic transmission strategies employing artificial neural networks. *Communications Letters, IEEE*, 2(8):241–243, Aug 1998.

[87] M. Eisencraft, R.D. Fanganiello, and L.H.A. Monteiro. Chaotic synchronization in discrete-time systems connected by bandlimited channels. *Communications Letters, IEEE*, 15(6):671–673, June 2011.

[88] Min Long, Yunfei Chen, and Fei Peng. Simple and accurate analysis of ber performance for dcsk chaotic communication. *Communications Letters, IEEE*, 15(11):1175–1177, November 2011.

[89] Lei-Sheng Jin, Lei Ying, Shuang Lu, and Yan Zhang. Coexistence of synchronization and amplitude death in time-delay systems. In *Multimedia and Signal Processing (CMSP), 2011 International Conference on*, volume 2, pages 21–24, May 2011.

[90] Yan Wang, Ying-Cheng Lai, and Zhigang Zheng. Onset of colored-noise-induced synchronization in chaotic systems. *Phys. Rev. E*, 79:056210, May 2009.

[91] A. J. Sievers and S. Takeno. Intrinsic localized modes in anharmonic crystals. *Phys. Rev. Lett.*, 61:970–973, Aug 1988.

[92] P. Binder, D. Abraimov, A. V. Ustinov, S. Flach, and Y. Zolotaryuk. Observation of breathers in josephson ladders. *Phys. Rev. Lett.*, 84:745–748, Jan 2000.

[93] R. Morandotti, U. Peschel, J. S. Aitchison, H. S. Eisenberg, and Y. Silberberg. Dynamics of discrete solitons in optical waveguide arrays. *Phys. Rev. Lett.*, 83:2726–2729, Oct 1999.

[94] Arthur R. McGurn. Intrinsic localized modes in photonic crystal circuits. *Chaos*, 13(2):754–765, 2003.

[95] L. Q. English, F. Palmero, P. Candiani, J. Cuevas, R. Carretero-González, P. G. Kevrekidis, and A. J. Sievers. Generation of localized modes in an electrical lattice using subharmonic driving. *Phys. Rev. Lett.*, 108:084101, Feb 2012.

[96] Daniel Brake, Huiwen Xu, Andrew Hollowell, Ganesh Balakrishnan, Chris Hains, Mario Marconi, and Vakhtang Putkaradze. Intrinsic localized modes in two-dimensional vibrations of crystalline pillars and their application for sensing. *Journal of Applied Physics*, 112(10):–, 2012.

[97] M. E. Manley, A. J. Sievers, J. W. Lynn, S. A. Kiselev, N. I. Agladze, Y. Chen, A. Llobet, and A. Alatas. Intrinsic localized modes observed in the high-temperature vibrational spectrum of nai. *Phys. Rev. B*, 79:134304, Apr 2009.

[98] M. Haas, V. Hizhnyakov, A. Shelkan, M. Klopov, and A. J. Sievers. Prediction of high-frequency intrinsic localized modes in ni and nb. *Phys. Rev. B*, 84:144303, Oct 2011.

[99] M. Lakshmanan, B. Subash, and Avadh Saxena. Intrinsic localized modes of a classical discrete anisotropic heisenberg ferromagnetic spin chain. *Physics Letters A*, 378(16–17):1119 – 1125, 2014.

[100] Ryan Stearrett and L Q English. Experimental generation of intrinsic localized modes in a discrete electrical transmission line. *Journal of Physics D: Applied Physics*, 40(17):5394, 2007.

[101] Yuli Starosvetsky and Alexander F. Vakakis. Traveling waves and localized modes in one-dimensional homogeneous granular chains with no precompression. *Phys. Rev. E*, 82:026603, Aug 2010.

[102] L. Q. English, F. Palmero, A. J. Sievers, P. G. Kevrekidis, and D. H. Barnak. Traveling and stationary intrinsic localized modes and their spatial control in electrical lattices. *Phys. Rev. E*, 81:046605, Apr 2010.

[103] Takahiro Shimada, Daisuke Shirasaki, and Takayuki Kitamura. Stone-wales transformations triggered by intrinsic localized modes in carbon nanotubes. *Phys. Rev. B*, 81:035401, Jan 2010.

[104] V Hizhnyakov, M Haas, A Shelkan, and M Klopov. Theory and molecular dynamics simulations of intrinsic localized modes and defect formation in solids. *Physica Scripta*, 89(4):044003, 2014.

[105] M. Sato, B. E. Hubbard, A. J. Sievers, B. Ilic, D. A. Czaplewski, and H. G. Craighead. Observation of locked intrinsic localized vibrational modes in a micromechanical oscillator array. *Phys. Rev. Lett.*, 90:044102, Jan 2003.

[106] M. Sato, B. E. Hubbard, L. Q. English, A. J. Sievers, B. Ilic, D. A. Czaplewski, and H. G. Craighead. Study of intrinsic localized vibrational modes in micromechanical oscillator arrays. *Chaos*, 13(2):702–715, 2003.

[107] M. Sato, B. E. Hubbard, and A. J. Sievers. *Colloquium* : Nonlinear energy localization and its manipulation in micromechanical oscillator arrays. *Rev. Mod. Phys.*, 78:137–157, Jan 2006.

[108] Masayuki Kimura and Takashi Hikihara. Stability change of intrinsic localized mode in finite nonlinear coupled oscillators. *Physics Letters A*, 372(25):4592 – 4595, 2008.

[109] Eyal Kenig, Boris A. Malomed, M. C. Cross, and Ron Lifshitz. Intrinsic localized modes in parametrically driven arrays of nonlinear resonators. *Phys. Rev. E*, 80:046202, Oct 2009.

[110] Masayuki Kimura and Takashi Hikihara. Coupled cantilever array with tunable on-site nonlinearity and observation of localized oscillations. *Physics Letters A*, 373(14):1257 – 1260, 2009.

[111] A.J. Dick, B. Balachandran, and Jr. Mote, C.D. Intrinsic localized modes in microresonator arrays and their relationship to nonlinear vibration modes. *Nonlinear Dynamics*, 54(1-2):13–29, 2008.

[112] M. Sato, S. Imai, N. Fujita, S. Nishimura, Y. Takao, Y. Sada, B. E. Hubbard, B. Ilic, and A. J. Sievers. Experimental observation of the bifurcation dynamics of an intrinsic localized mode in a driven 1d nonlinear lattice. *Phys. Rev. Lett.*, 107:234101, Nov 2011.

[113] Qingfei Chen, Ying-Cheng Lai, and David Dietz. Controlled generation of intrinsic localized modes in microelectromechanical cantilever arrays. *Chaos*, 20(4):–, 2010.

[114] Jing-Quan Liu, Hua-Bin Fang, Zheng-Yi Xu, Xin-Hui Mao, Xiu-Cheng Shen, Di Chen, Hang Liao, and Bing-Chu Cai. A mems-based piezoelectric power generator array for vibration energy harvesting. *Microelectronics Journal*, 39(5):802 – 806, 2008.

[115] Zhengjun Chew and Lijie Li. Design and characterisation of a piezoelectric scavenging device with multiple resonant frequencies. *Sensors and Actuators A: Physical*, 162(1):82 – 92, 2010.

[116] L. Gammaitoni, I. Neri, and H. Vocca. Nonlinear oscillators for vibration energy harvesting. *Applied Physics Letters*, 94(16):–, 2009.

[117] ZL. Wang. Nanopiezotronics. *Advanced materials*, 19(6):889–892, 2007.

[118] Ruomeng Yu, Caofeng Pan, Jun Chen, Guang Zhu, and Zhong Lin Wang. Enhanced performance of a zno nanowire-based self-powered glucose sensor by piezotronic effect. *Advanced Functional Materials*, 23(47):5868–5874, 2013.

[119] Thierry Dauxois, Michel Peyrard, and C. R. Willis. Discreteness effects on the formation and propagation of breathers in nonlinear klein-gordon equations. *Phys. Rev. E*, 48:4768–4778, Dec 1993.

[120] S.P. Timoshenko J.M. Gere. Mechanics of materials, chapter 5. *PWS Publishing, Boston, USA*, page 303–308, Dec 1997.

[121] J. Guckenheimer and P. Holmes. Nonlinear oscillations, dynamical systems, and bifurcations of vector fields. *Springer, New York*, Dec 1990.

[122] A. Erturk and D.J. Inman. Broadband piezoelectric power generation on high-energy orbits of the bistable duffing oscillator with electromechanical coupling. *Journal of Sound and Vibration*, 330(10):2339 – 2353, 2011. Dynamics of Vibro-Impact Systems.

[123] D. Rugar and P. Grütter. Mechanical parametric amplification and thermomechanical noise squeezing. *Phys. Rev. Lett.*, 67:699–702, Aug 1991.

[124] R. B. Karabalin, X. L. Feng, and M. L. Roukes. Parametric nanomechanical amplification at very high frequency. *Nano Letters*, 9(9):3116–3123, 2009. PMID: 19736969.

[125] R. B. Karabalin, S. C. Masmanidis, and M. L. Roukes. Efficient parametric amplification in high and very high frequency piezoelectric nanoelectromechanical systems. *Applied Physics Letters*, 97(18):–, 2010.

[126] Barry E. DeMartini, Jeffrey F. Rhoads, K.L. Turner, Steven W. Shaw, and J. Moehlis. Linear and nonlinear tuning of parametrically excited mems oscillators. *Microelectromechanical Systems, Journal of*, 16(2):310–318, April 2007.

[127] Barry E. DeMartini, H.E. Butterfield, J. Moehlis, and K.L. Turner. Chaos for a microelectromechanical oscillator governed by the nonlinear mathieu equation. *Microelectromechanical Systems, Journal of*, 16(6):1314–1323, Dec 2007.

[128] Song Zhankui and Kaibiao Sun. Nonlinear and chaos control of a micro-electromechanical system by using second-order fast terminal sliding mode control. *Communications in Nonlinear Science and Numerical Simulation*, 18(9):2540 – 2548, 2013.

[129] Zhilin Qu, Gang Hu, Guojian Yang, and Guangrong Qin. Phase effect in taming nonautonomous chaos by weak harmonic perturbations. *Phys. Rev. Lett.*, 74:1736–1739, Mar 1995.

[130] R. Meucci, W. Gadomski, M. Ciofini, and F. T. Arecchi. Experimental control of chaos by means of weak parametric perturbations. *Phys. Rev. E*, 49:R2528–R2531, Apr 1994.

[131] L. Y. Gorelik, A. Isacsson, M. V. Voinova, B. Kasemo, R. I. Shekhter, and M. Jonson. Shuttle mechanism for charge transfer in coulomb blockade nanostructures. *Phys. Rev. Lett.*, 80:4526–4529, May 1998.

[132] R. P. Andres, T. Bein, M. Dorogi, S. Feng, J. I. Henderson, C. P. Kubiak, W. Mahoney, R. G. Osifchin, and R. Reifenberger. Coulomb staircase at room temperature in a self-assembled molecular nanostructure. *Science*, 31:1323–1325, 1996.

[133] A. Isacsson, L.Y. Gorelik, M.V. Voinova, B. Kasemo, R.I. Shekhter, and M. Jonson. Shuttle instability in self-assembled coulomb blockade nanostructures. *Physica B: Condensed Matter*, 255(1–4):150 – 163, 1998.

[134] L.Y. Gorelik, A. Isacsson, Y.M. Galperin, R.I. Shekhter, and M. Jonson. Nanoelectromechanics and single-charge tunneling. *Current Applied Physics*, 2(1):3 – 10, 2002.

[135] A. Isacsson and T. Nord. Low-frequency current noise of the single-electron shuttle. *EPL (Europhysics Letters)*, 66(5):708, 2004.

[136] F Pistolesi and Rosario Fazio. Dynamics and current fluctuations in an ac-driven charge shuttle. *New Journal of Physics*, 8(7):113, 2006.

[137] Taegeun Song, Mikhail N Kiselev, Konstantin Kikoin, Robert I Shekhter, and Leonid Y Gorelik. Self-sustained oscillations in nanoelectromechanical systems induced by kondo resonance. *New Journal of Physics*, 16(3):033043, 2014.

[138] Michael J Moeckel, Darren R Southworth, Eva M Weig, and Florian Marquardt. Synchronizing a single-electron shuttle to an external drive. *New Journal of Physics*, 16(4):043009, 2014.

[139] M. N. Kiselev. Dynamical symmetries and quantum transport through nanostructures. *physica status solidi (c)*, 4(9):3362–3373, 2007.

[140] T. Nord and A. Isacsson. Impact of van der waals forces on the classical shuttle instability. *Phys. Rev. B*, 69:035309, Jan 2004.

[141] Norihiko Nishiguchi. Shuttle instability induced by an ac gate in a nanoelectromechanical single-electron transistor. *Phys. Rev. B*, 78:085407, Aug 2008.

[142] F. Pistolesi and Rosario Fazio. Charge shuttle as a nanomechanical rectifier. *Phys. Rev. Lett.*, 94:036806, Jan 2005.

[143] Dominik V. Scheible and Robert H. Blick. Silicon nanopillars for mechanical single-electron transport. *Applied Physics Letters*, 84(23):4632–4634, 2004.

[144] D. R. Koenig and E. M. Weig. Voltage-sustained self-oscillation of a nano-mechanical electron shuttle. *Applied Physics Letters*, 101(21):–, 2012.

[145] Chulki Kim, Marta Prada, and Robert H. Blick. Coulomb blockade in a coupled nanomechanical electron shuttle. *ACS Nano*, 6(1):651–655, 2012. PMID: 22201451.

[146] Andriy V. Moskalenko, Sergey N. Gordeev, Olivia F. Koentjoro, Paul R. Raithby, Robert W. French, Frank Marken, and Sergey E. Savel'ev. Nanomechanical electron shuttle consisting of a gold nanoparticle embedded within the gap between two gold electrodes. *Phys. Rev. B*, 79:241403, Jun 2009.

[147] Chulki Kim, Marta Prada, Gloria Platero, and Robert H. Blick. Realizing broadbands of strong nonlinear coupling in nanoelectromechanical electron shuttles. *Phys. Rev. Lett.*, 111:197202, Nov 2013.

[148] R.H. Blick and R.A. Marsland. Nanomechanical computer. *United States Patent 7414437B1*, 2008.

[149] Matthew Spletzer, Arvind Raman, Alexander Q. Wu, Xianfan Xu, and Ron Reifenberger. Ultrasensitive mass sensing using mode localization in coupled microcantilevers. *Applied Physics Letters*, 88(25):–, 2006.

[150] Guanglei Wang, Liang Huang, Ying-Cheng Lai, and Celso Grebogi. Nonlinear dynamics and quantum entanglement in optomechanical systems. *Phys. Rev. Lett.*, 112:110406, Mar 2014.

[151] Florian Marquardt. Quantum mechanics: The gentle cooling touch of light. *Nature*, 478:47–48, 2011.

[152] Markus Aspelmeyer, Tobias J. Kippenberg, and Florian Marquardt. Cavity optomechanics. *Rev. Mod. Phys.*, 86:1391–1452, Dec 2014.

[153] Monika H. Schleier-Smith, Ian D. Leroux, Hao Zhang, Mackenzie A. Van Camp, and Vladan Vuletić. Optomechanical cavity cooling of an atomic ensemble. *Phys. Rev. Lett.*, 107:143005, Sep 2011.

[154] E. Verhagen, S. Deléglise, S. Weis, A. Schliesser, and T. J. Kippenberg. Quantum-coherent coupling of a mechanical oscillator to an optical cavity mode. *Nature*, 482:63–67, 2012.

[155] D. K. Armani, T. J. Kippenberg, S. M. Spillane, and K. J. Vahala. Ultra-high-q toroid microcavity on a chip. *Nature*, 421:925–928, 2003.

[156] Tal Carmon, Hossein Rokhsari, Lan Yang, Tobias J. Kippenberg, and Kerry J. Vahala. Temporal behavior of radiation-pressure-induced vibrations of an optical microcavity phonon mode. *Phys. Rev. Lett.*, 94:223902, Jun 2005.

[157] Tal Carmon, M. C. Cross, and Kerry J. Vahala. Chaotic quivering of micron-scaled on-chip resonators excited by centrifugal optical pressure. *Phys. Rev. Lett.*, 98:167203, Apr 2007.

[158] Tal Carmon and Kerry J. Vahala. Modal spectroscopy of optoexcited vibrations of a micron-scale on-chip resonator at greater than 1 ghz frequency. *Phys. Rev. Lett.*, 98:123901, Mar 2007.

[159] C. K. Law. Interaction between a moving mirror and radiation pressure: A hamiltonian formulation. *Phys. Rev. A*, 51:2537–2541, Mar 1995.

[160] D. Vitali, S. Gigan, A. Ferreira, H. R. Böhm, P. Tombesi, A. Guerreiro, V. Vedral, A. Zeilinger, and M. Aspelmeyer. Optomechanical entanglement between a movable mirror and a cavity field. *Phys. Rev. Lett.*, 98:030405, Jan 2007.

[161] Fenfei Liu and M. Hossein-Zadeh. Mass sensing with optomechanical oscillation. *Sensors Journal, IEEE*, 13(1):146–147, Jan 2013.

[162] Kartik Srinivasan, Houxun Miao, Matthew T. Rakher, Marcelo Davanço, and Vladimir Aksyuk. Optomechanical transduction of an integrated silicon cantilever probe using a microdisk resonator. *Nano Letters*, 11(2):791–797, 2011. PMID: 21250747.

[163] Alexander G. Krause, Martin Winger, Tim D. Blasius, Qiang Lin, and Oskar Painter. A high-resolution microchip optomechanical accelerometer. *Nature Photonics*, 6:768–772, 2012.

[164] E. Gavartin, P. Verlot, and T. J. Kippenberg. A hybrid on-chip optomechanical transducer for ultrasensitive force measurements. *Nature Nanotechnology*, 7:509–514, 2012.

[165] Kyu Hyun Kim, Gaurav Bahl, Wonsuk Lee, Jing Liu, Matthew Tomes, Xudong Fan, and Tal Carmon. Cavity optomechanics on a microfluidic resonator with water and viscous liquids. *Light: Science and Applications*, 2, 2013.

[166] Garrett D. Cole and Markus Aspelmeyer. Cavity optomechanics: Mechanical memory sees the light. *Nature Nanotechnology*, 6:690–691, 2011.

[167] A. Isacsson. Dynamics of a three-terminal mechanically flexible tunneling contact. *Phys. Rev. B*, 64:035326, Jun 2001.

[168] Yuji Ando and Tomohiro Itoh. Calculation of transmission tunneling current across arbitrary potential barriers. *Journal of Applied Physics*, 61(4):1497–1502, 1987.

Appendix A

An Example for Understanding Quantum Tunneling

In chapter 6 and 7, quantum tunneling has been involved, and the content in this appendix is served to understand this quantum phenomenon. Here, a basic two-terminal device that is made of ZnO is considered, as shown in Fig. A.1. The middel part of the device is a very short nanowire (80 nm), in which The electron transport in z-direction can be seen as ballistic, and only a few electron energy states exist in x-y plane. For an electron in quantum wire, its energy is given by:

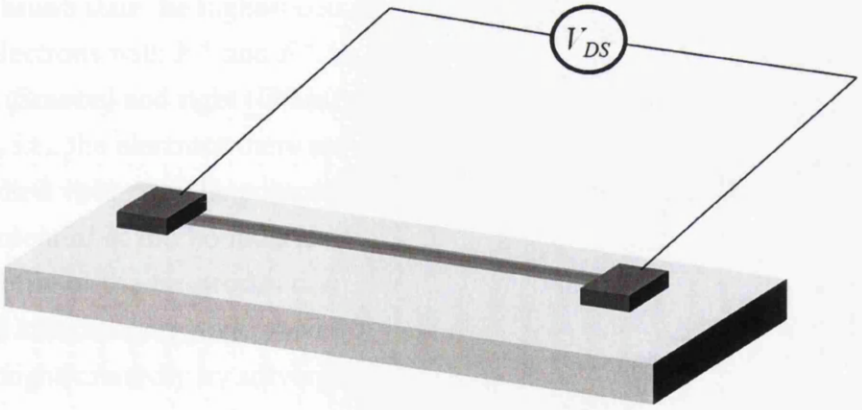

Fig. A.1 Proposed two-terminal device

$$E = \frac{\pi^2\hbar^2}{2m}\left(\frac{n_x^2}{L_x^2} + \frac{n_y^2}{L_y^2}\right) + \frac{\hbar^2 k_z^2}{2m}, \quad n_x, n_y = 1, 2, \ldots \tag{A.1}$$

where the electron in z-direction is modeled by plane waves with wave number k_z. $\hbar$ is the Planck constant divided by 2π. n_x and n_y are energy quantum number in x and y directions,

respectively. m is the effective mass of the electron. L_x and L_y are the length in $x-y$ plane. k_z is the wavenumber in z-direction. Three modes of the energy in quantum wire are plotted in Fig. A.2. The electrons in the nanowire will occupy the energy level from low to high, and

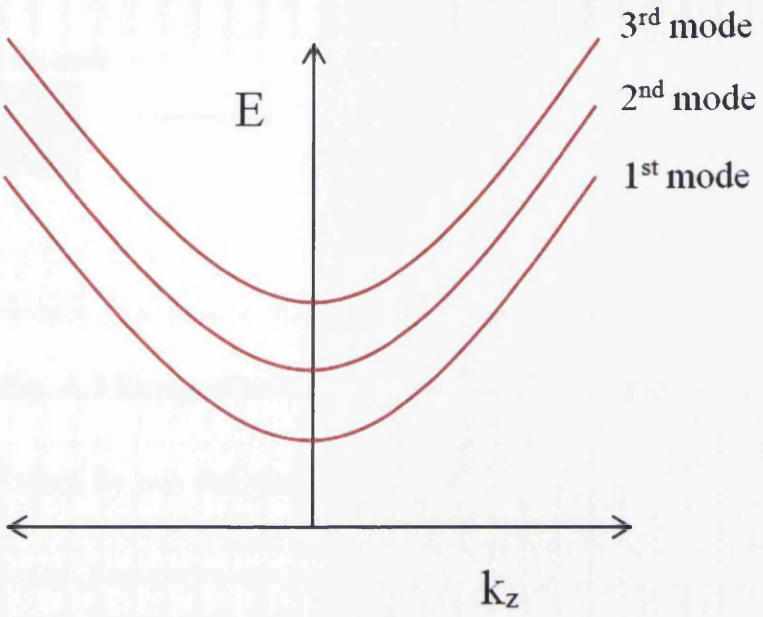

Fig. A.2 Energy modes of electrons in ZnO wire

in the equilibrium state the highest occupied energy is called quasi Fermi levels, represented by F^+ for electrons with F^+ and F^- for the electrons with $-k$.

The left (Source) and right (Drain) electrodes of the device are assumed to be reservoirs of electrons, i.e., the electrons there are keeping presumably in equilibrium state, even under a given applied voltage. The potential inside of the electrodes is approximately constant while the potential at the boundaries has a step which confines the electrons. The whole potential profile of the electrodes can be seen as a finite square well as shown in Fig. A.3. The allowed kinetic energy and wave functions of electrons inside of the electrodes can be obtained straightforwardly by solving the Schrödinger equation, as:

$$\begin{aligned} T_n &= \frac{\hbar^2 k_n^2}{2m} = \frac{n^2\pi^2\hbar^2}{2mL^2} \\ \psi_n(z) &= \sqrt{\frac{2}{L}} sin(k_n z) \end{aligned} \tag{A.2}$$

where L is the length of the electrodes in z-direction and n ($n = 1,2,3\ldots$) is the energy quantum number. k_n is z-direction component of wave vector at energy state n. The electrons occupy the energy state according to the Pauli exclusion principle that demands one energy

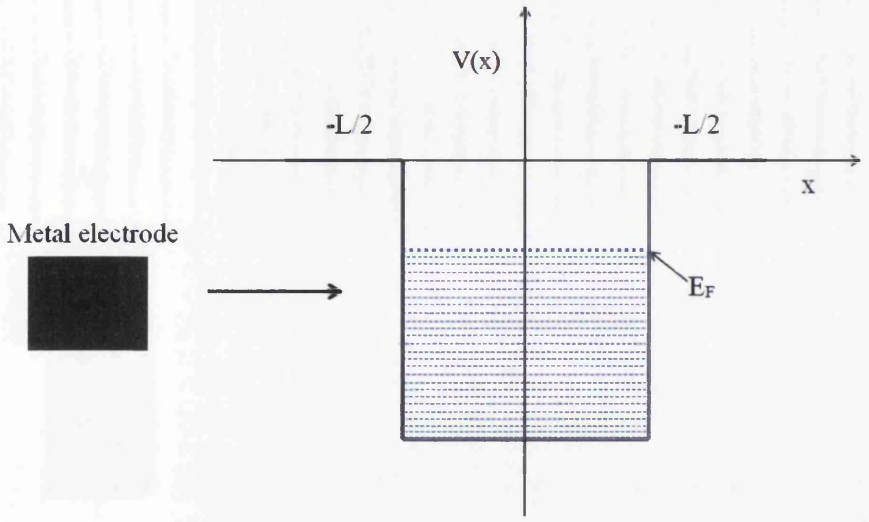

Fig. A.3 Energy distribution of electrons in the electrodes

state can only be taken by two electrons if considering the spin. The highest energy state occupied by electrons is Femi energy E_F or so-called chemical potential μ. When the electrodes and the ZnO nanowire are connected and there is no bias applied to S and D, the Femi energy must be constant through the device. Otherwise, there will be current flowing. This scenario is plotted in Fig. A.4, where the chemical potential μ_S, F^+, F^- and μ_D are being flat. The number of electrons with k^+ wavenumber equals to the number of the electrons with k^- wavenumber so there is not current. If a DC voltage V_e is applied to the source (S) and drain (D), the electron equilibrium state will be broken. As shown in Fig. A.5 the unbalance between the electrons with k^+ and k^- occurs with F^+ is higher than F^-, which leads to some uncompensated electrons that have energy between F^+ and F^- flowing into the drain, i,e,. current arising. The quasi Fermi level now have the following relations with chemical potential, which are: $F^+ = \mu_S$ and $F^- = \mu_D$. Also, the relation of the shift between the potential energies of each electrodes and the applied V_e is given by $\mu_D - \mu_S = -qV_e$, where q is the charge of a single electron. Under a applied voltage V_e, the current in a ballistic quantum wire is given by the famous Landauer formula, which is:

$$I_{in} = -q^2 \frac{V_e}{\pi\hbar} \tag{A.3}$$

I_{in} is the current brought by the uncompensated electrons. However, in this device, the quantum wire is made by ZnO, which is semiconductive material, and the electrodes are made of metals such as Ag. When a two-terminal device is fabricated, the M-S interfaces would be formed into ohmic or schottky diode. Here, a general case, i.e, ohmic at left end and schottky at right is considered. Due to the depletion region formed at the interface, the

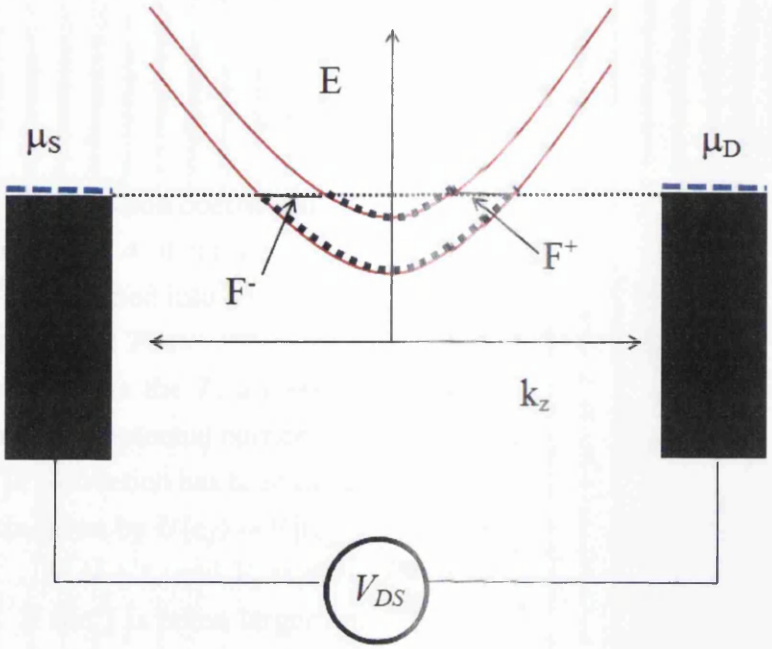

$V_{DS} = 0$

Fig. A.4 Electron states when the device is in equilibrium

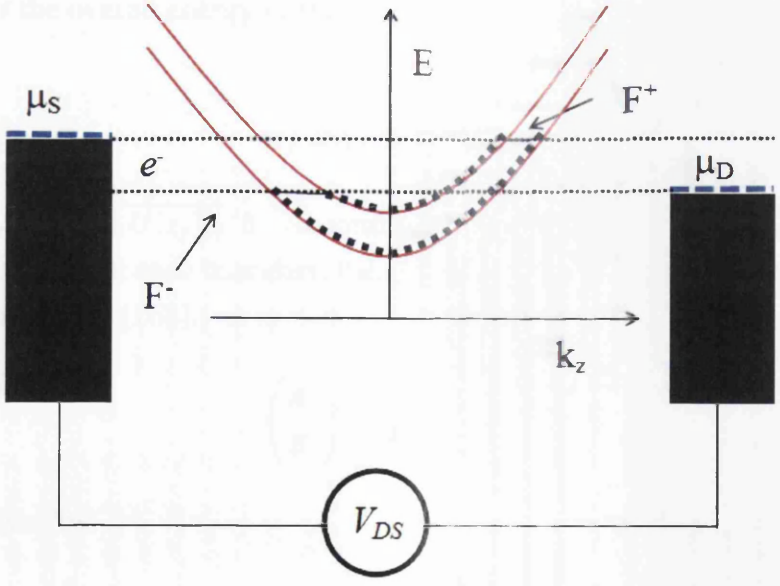

$V_{DS} = V_e$

Fig. A.5 Electron states when the device is applied a voltage

current I_{in}, therefore, can only partially be transmitted, and the transmitted current can be obtained by:

$$I_T = TI_{in} = -q^2 \frac{V_e}{\pi\hbar} T \tag{A.4}$$

where T is the transmission coefficient for an electron that has the Fermi energy in the left electrode. From Eq. A.4, it can be seen that the problem of calculating the current in the short device is transformed into a scatting problem. Thus, the key of which is to analyze the transmission coefficient T.

In order to calculate the T, a method that can be used to calculate the transmission coefficient of arbitrary potential barrier is used [168]. As shown in the Fig. A.6, the potential inside the wire in z-direction has been divided into many small rectangles, the potential $U(z_j)$ of j_{th} segment is given by $U(z_j) = V[(z_{j-1} + z_j)/2]$, where j is the number of the segment ($j = 0,1,2,3,\ldots,N,N+1$, and V_z is the potential energy of the whole device including the electrodes. If the j is taken larger and larger, the continuous potential variation will be recovered gradually. For a single rectangular potential barrier j, the time-independent wavefunction of an electron inside j is described by the Schrödinger equation:

$$E\psi(z_j) + \frac{\hbar^2}{2m}\frac{d^2\psi(z_j)}{dx^2} - U(z_j)\psi(z_j) = 0 \tag{A.5}$$

where the E is the overall energy of the electron. The wave function of ψ_j can be derived easily:

$$\psi_j = A_j e^{ik_j z} + B_j e^{-ik_j z} \tag{A.6}$$

where $k_j = \sqrt{[2m(E - U(z_j))]}/\hbar$. According to the quantum theory, the ψ_j and $d\psi_j/dz$ should be continuous at each boundary, then the amplitude A_j and B_j can be determined by the following equation [168]:

$$\begin{pmatrix} A_j \\ B_j \end{pmatrix} = \prod_{l=0}^{j=1} M_l \begin{pmatrix} A_0 \\ B_0 \end{pmatrix} \tag{A.7}$$

where M_l is given by:

$$M_l = \begin{bmatrix} (1+S_l)exp[-i(k_{l+1}-k_l)z_l] & (1-S_l)exp[-i(k_{l+1}+k_l)z_l] \\ (1-S_l)exp[i(k_{l+1}+k_l)z_l] & (1+S_l)exp[-i(k_{l+1}-k_l)z_l] \end{bmatrix} \tag{A.8}$$

and $S_l = k_l/k_{l+1}$. The scatting matrix M can then be obtained as:

$$M = \begin{bmatrix} M_{11} & M_{12} \\ M_{21} & M_{22} \end{bmatrix} = \prod_{l=0}^{N} M_l \tag{A.9}$$

Finally, the T can be calculated by: $T = k_{N+1}/k_0 |k_0/(k_{N+1}M_{22})|^2$, provided the $A_0 = 1$ and $B_{N+1} = 0$.

The potential energy function $V(z)$ has to be clarified if calculating the T by the above method. First, the potential variation under an applied V_e is assumed to be linear as the quantum wire is not a perfectly metallic wires but a short nanoscale device, and the electrodes have a relatively bigger cross-section area. The source and drain capacitances can then be simply represented by parallel plate capacitors. The potential energy in the wire can be described by:

$$V_w(z) = V_{w0} - qV_e \frac{C_D(z)}{C_{ES}(z)} \tag{A.10}$$

where $C_{ES} = C_D + C_S$ is total electrostatic capacitance at point at z, and C_D and C_S are the capacitance linking the point at z to drain and source, respectively. V_{w0} is the initial potential energy field of the electrons in the quantum wire. The picture of potential V_{w0} has been presented in Fig. A.6, where at the left end and right end the potential variations due to the forming M-S contacts have been considered. The V_{w0} in the M-S contact regions can be calculated by Poisson equation, which are not given in detail here. The material of the two electrodes are chosen asAg. The donor density N_d in the ZnO is taken as 1×10^{16} /cm^3. The built-in potential of the Schottky barrier$\phi_B = 0.3$ eV. An electron that comes from the source with$E = E_F = 5.49$ eV. The potential field in the nanowire is divided into 360 grids (z_1 to z_{361}). Based on the parameters taken above, the potential energy diagram of the device including two electrodes has been plotted in Fig. A.6, where the schottky barrier at the right side is about 0.3 eV, and an electron that have energy E_F from the left electrode with amplitude A_0 and B_0 is shown, represented by the red and blue arrows in the figure. The amplitude of the incoming electron in each segment are presented by A_j and $B_[j]$, and when the electron reach the right electrode, it has only the amplitude A_{N+1} as no electron coming from right electrode assummed.

The transmission coefficient T in the nanowire is firstly calculated in Fig. A.7. In Fig. A.7 (a), the potential energy diagram under the applied voltage V_e is shown. The potential is linearly decreased from the left to right, as the negative voltage is added to the left. In Fig. A.7 (b), it is seen the variation of the T versus applied voltage V_e. The transmission coefficient is performing the nonlinearly while in some range the T is oscillating due to the

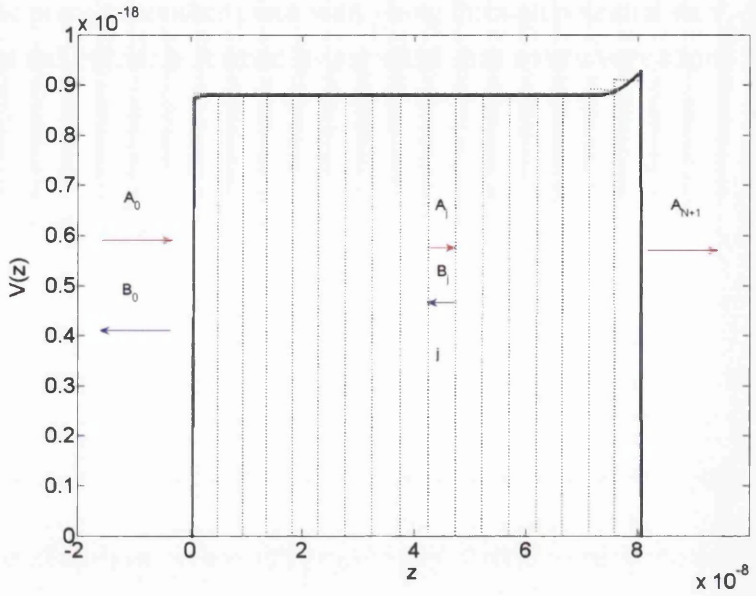

Fig. A.6 Energy diagram of the device when there is no applied voltage and strain

resonance through the virtual states above the barrier. In Fig A.7. (c), the current with the varied applied voltage V_e has been plotted. From this example, it is clearly to see how the

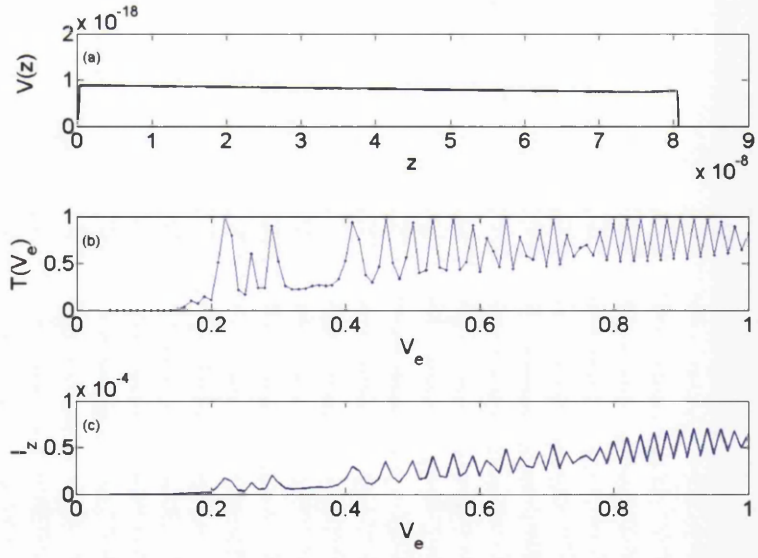

Fig. A.7 Transmission result when the device is applied a voltage V_e (0-1 V) . a) potential energy. b) Transmission vs V_e. c) Transmission current I_z vs V_e]

electron transport from one electrodes to another one. In the quantum tunneling, the electron

tunnel from one place to another place with going through potential barriers. In the chapter 6 and 7, the potential barrier is formed by air which has a very very short distance.

Appendix B

Program Code

B.1 Calculating The Motion of The CNT Nanotube

```
global Omiga0 alpha bta F0 Omiga1

    b=0.066e-9;

    d=0.548e-9;

    L=100e-9;

    p=1350;

    E=5.5e12;

    Im=pi/4*(d/16-(d/2-b));

    Is=pi*(d/8-(d/2-b));

    C=2*pi*d-2*pi*b;

    A=pi*b*(d-b);
sigmat=0;
sigmaxx=sigmat;
tauxx=0;
Es=0;
```

```
vdc=5;

    v0=5;
T=300;
Pr=1*1.01325*10;
h=500e-9;
kB=1.38*10;
ebsr0=8.85*10;
m=5.6*10;
vt=(kB*T/m);

    bta=pi*Pr*d/(4*vt*p*A);
F0=pi*ebsr0*(vdc*v0)/(h*(log(4*h/d)))*(2/3)/(p*A);
EIm=sigmaxx*Im+E*Im+tauxx*Is+Es*Is;
PP=sigmaxx*A+tauxx*C;
Omiga0=((16*pi*EIm+4*pi*PP*L)/(3*p*A*L));
alpha=E/(18*p)*(2*pi/L);

    Omiga1=1*Omiga0;

    [t,q]=ode45('nanotube',[0 1.5*10e-6],[0 0 0.1e-9 0.1]);
```

B.2 Function of Calculating The Lyapunov Exponents

```
function [Texp,Lexp]=lyapunov(n,rhsextfcn,fcnintegrator,tstart,stept,tend,ystart,ioutp);

    n1=n; n2=n1*(n1+1);

    nit = round((tend-tstart)/stept);

    y=zeros(n2,1); cum=zeros(n1,1); y0=y;
gsc=cum; znorm=cum;

    y(1:n)=ystart(:);
```

```
    for i=1:n1 y((n1+1)*i)=1.0; end;

    t=tstart;

    for ITERLYAP=1:nit

    [T,Y] = feval(fcnintegrator,rhsextfcn,[t t+stept],y);

    t=t+stept;
y=Y(size(Y,1),:);

    for i=1:n1
for j=1:n1 y0(n1*i+j)=y(n1*j+i); end;
end;

    znorm(1)=0.0;
for j=1:n1 znorm(1)=znorm(1)+y0(n1*j+1); end;

    znorm(1)=sqrt(znorm(1));

    for j=1:n1 y0(n1*j+1)=y0(n1*j+1)/znorm(1); end;

    for j=2:n1
for k=1:(j-1)
gsc(k)=0.0;
for l=1:n1 gsc(k)=gsc(k)+y0(n1*l+j)*y0(n1*l+k); end;
end;

    for k=1:n1
for l=1:(j-1)
y0(n1*k+j)=y0(n1*k+j)-gsc(l)*y0(n1*k+l);
end;
end;

    znorm(j)=0.0;
for k=1:n1 znorm(j)=znorm(j)+y0(n1*k+j); end;
```

```
znorm(j)=sqrt(znorm(j));

    for k=1:n1 y0(n1*k+j)=y0(n1*k+j)/znorm(j); end;
end;

    for k=1:n1 cum(k)=cum(k)+log(znorm(k)); end;

    for k=1:n1
lp(k)=cum(k)/(t-tstart);
end;

    if ITERLYAP==1
Lexp=lp;
Texp=t;
else
Lexp=[Lexp; lp];
Texp=[Texp; t];
end;

    if (mod(ITERLYAP,ioutp)==0)
fprintf('t=for k=1:n1 fprintf(' fprintf('n');
end;

    for i=1:n1
for j=1:n1
y(n1*j+i)=y0(n1*i+j);
end;
end;

    end;
```

B.3 Calculating The Quantum Tunnelling

```
m0=9.109e-31;
h=6.626e-34/(2*pi);
```

```
q=1.602e-19;
EF=7*1.6e-19;
Lz=80e-9;

    L=0.01;

    n=360;
ol=Lz/n;

    E1=1*EF;

    VV=0.1:0.0001:1.6;
n0=size(VV); n1=n0(2);

    for k=1:n1
Ve=VV(k);
VL=Ve*q;
kL=(2*m0*(E1-VL))(1/2)/h;
AL=1/(1i*(2*L)(1/2));

    VR=0;
kR=(2*m0*(E1-VR))(1/2)/h;

    I=eye(n+3,n+3);
Q=zeros(n+3,1);
Q(1)=h(2)/(2*m0*ol(2))*AL*(exp(1i*kL*ol)-exp(-1i*kL*ol));

    V=zeros(n+3,1);

    Vw0=7.5*q;
V(1)=VL;
V(n+3)=VR;
for i=2:n+2
V(i)=Vw0-q*(Ve/n)*(i-2);
end
```

```
    H=zeros(n+3,n+3);

    WL=-h(2)/(2*m0*ol(2))*exp(1i*kL*ol);
WR=-h(2)/(2*m0*ol(2))*exp(1i*kR*ol);

    H(1,1)= h(2)/(m0*ol(2))+V(1)+WL;
H(n+3,n+3)=h(2)/(m0*o(2))+V(n+3)+WR;
H(1,2)=-h(2)/(2*m0*ol(2));
H(n+3,n+2)=-h(2)/(2*m0*ol(2));

    for j=2:n+2
H(j,j)=h(2)/(m0*ol(2))+V(j);
H(j,j-1)=-h(2)/(2*m0*ol(2));
H(j,j+1)=-h(2)/(2*m0*ol(2));
end
    Tr1=E1*I;
Tr2=Tr1-H;
Wave=Tr2;
Pw=abs(Wave).(2);

    reflec(k)=(abs((Wave(1)-AL)/AL))(2);
end
trans=1-reflec;

    [rows,cols]=find(trans==max(max(trans)));
Vp=VV(cols);

    [num,val]=sort(trans);
for g=k:-1:k-26
g1=k-g+1;
VVp(g1)=VV(val(g));
end

    [num1,val1]=sort(VVp);
```

```
    for o=1:26
VVpo(o)=num1(o+1)-num1(o);
end
```